X-RAY IMAGING AND READOUT OF A TPC WITH THE MEDIPIX CMOS ASIC

PROEFSCHRIFT

ter verkrijging van
de graad van doctor aan de Universiteit Twente,
op gezag van de rector magnificus,
prof. dr. W.H.M. Zijm,
volgens besluit van het College voor Promoties
in het openbaar te verdedigen
op donderdag 2 juni 2005 om 16.45 uur

door

Alessandro Fornaini

geboren op 1 Juni 1975

te Pisa (Italië)

Dit proefschrift is goedgekeurd door:

prof. dr. ing. B. van Eijk (promotor) en
dr. J.L. Visschers (assistent-promotor)

Contents

Introduction **1**

1 Interaction of particles with matter **3**
1.1 Photon interaction processes . . . 3
1.1.1 Photoelectric effect . . . 6
1.1.2 Compton scattering . . . 8
1.1.3 Pair production . . . 10
1.2 Energy loss of charged particles in matter . . . 11
1.2.1 The Bethe-Bloch formula . . . 13
1.2.2 Energy dependence of the energy loss . . . 15
1.2.3 Range . . . 15
1.3 Energy loss of electrons and positrons . . . 17
1.3.1 Energy loss by atomic collisions . . . 17
1.3.2 Energy loss by radiation (bremsstrahlung) . . . 18
1.3.3 Critical energy and radiation length . . . 19
1.4 Conclusions . . . 20

2 Introduction to X-ray imaging **23**
2.1 Image characterization . . . 23
2.1.1 Spatial resolution . . . 23
2.1.2 Signal-to-noise ratio . . . 24
2.1.3 Image contrast . . . 24
2.1.4 Detective quantum efficiency . . . 25
2.1.5 PSF, LSF and ESF . . . 26
2.1.6 Modulation transfer function (MTF) . . . 28
2.1.7 Contrast transfer function . . . 31
2.1.8 Noise power spectrum and noise equivalent quanta . . . 32
2.2 X-ray imaging technologies . . . 32
2.2.1 Analog and digital systems . . . 32
2.2.2 Direct and indirect X-ray detection systems . . . 33
2.2.3 Counting, integrating and energy-weighting systems . . . 33
2.3 Conclusions . . . 34

3 Hybrid pixel detectors and the Medipix1 chip 35
3.1 Hybrid Pixel Detectors . . . 35
3.1.1 Advantages and disadvantages of hybrid pixel detector technology . . . 37
3.2 The Medipix1 X-ray Detector . . . 40
3.2.1 The Medipix1 pixel cell . . . 40
3.3 The Medipix1 readout system . . . 43
3.4 Medipix1 production and quality control . . . 46
3.4.1 Medipix1 wafer testing procedure . . . 47
3.5 Medipix1 Image Gallery . . . 49
3.6 Conclusions . . . 51

4 Medipix1 characterization with a synchrotron X-ray source 53
4.1 ESRF: the European Synchrotron Radiation Facility . . . 54
4.2 The experimental setup . . . 56
4.3 Spatial uniformity . . . 56
4.4 Linearity . . . 57
4.5 Absolute calibration and noise estimate . . . 59
4.6 Point Spread Function . . . 62
4.7 Subpixel sensitivity scanning . . . 63
4.8 Time resolution . . . 64
4.9 Radiation damage . . . 65
4.10 Conclusions . . . 66

5 Medipix2 67
5.1 Description of the Medipix2 chip . . . 68
5.1.1 The Medipix2 pixel cell . . . 71
5.1.1.1 The charge preamplifier . . . 73
5.1.1.2 The threshold discriminators . . . 73
5.1.1.3 Double Logic Discriminator . . . 75
5.1.1.4 Shift Register . . . 75
5.1.1.5 Pixel Configuration Register . . . 76
5.1.2 IO logical description of the Medipix2 chip . . . 77
5.2 Additional features of the Medipix2 chip . . . 79
5.2.1 The Charge Sharing Test (CST) . . . 79
5.2.2 Test pulse . . . 80
5.2.3 Fine threshold tuning . . . 80
5.3 The Medipix2 Serial Readout . . . 81
5.4 Medipix2 production and quality control . . . 83
5.5 Medipix2 wafer testing procedure . . . 84
5.6 Medipix2 image gallery . . . 87
5.7 Conclusions . . . 89

6 A tiled array of Medipix2 chips for X-ray imaging 91
6.1 Size limitations of an hybrid pixel detector . . . 91
6.2 Pixel detector array systems . . . 92
6.3 Medipix2 interconnectivity . . . 93
6.4 The 2×4 Medipix2 chipboard in build-up technology . . . 94
6.4.1 The 2 × 4 chipboard design . . . 95
6.5 Current status . . . 97
6.6 Conclusions . . . 98

7 The readout of a gas detector with the Medipix2 chip 99
7.1 Collider experiments . . . 99
7.2 Gas Filled detectors . . . 100
7.2.1 Multi-wire proportional chambers . . . 100
7.2.2 Drift chambers . . . 102
7.2.3 Time projection chambers . . . 103
7.2.4 Recent improvements: gas-filled chambers without wires . 104
7.3 A semiconductor readout for a gas detector . . . 106
7.3.1 Readout using a CMOS chip . . . 106
7.3.2 Readout implementation with the Medipix2 chip . . . 107
7.4 The GEM/Medipix2 TPC . . . 108
7.4.1 Results . . . 109
7.5 The Micromegas/Medipix2 TPC . . . 112
7.5.1 The post-processed Medipix2 chips . . . 114
7.5.2 Signal development . . . 115
7.5.3 Results . . . 117
7.5.4 Single electron detection efficiency . . . 119
7.5.5 Suppression of δ-rays . . . 121
7.5.6 The Moiré effect . . . 121
7.5.7 Discharges and damage to the Medipix2 chips . . . 124
7.5.8 Metalized and non-metalized Medipix2 chips . . . 125
7.6 Conclusions and future plans . . . 126

A Bump-bonding pixel detectors 129
A.1 The solder bump flip-chip process . . . 129
A.1.1 Under-Bump Metalization . . . 129
A.1.2 Solder Bumping . . . 130
A.1.3 Assembly . . . 130
A.1.4 Underfilling . . . 131
A.1.5 Remarks . . . 131
A.2 The indium bump process . . . 132
A.3 Inspection . . . 134

Summary 141

Samenvatting 143

Introduction

X-rays and gamma-rays were discovered respectively by Wilhelm Conrad Röntgen in 1895 and by Paul Villard in 1900, and their possible application to fields like medicine or physics research was immediately investigated.

Since then, after more than one century of study and development, the instruments employing X or gamma rays are countless. Instrumentation for X-ray detection is now needed in many different sectors, from medicine to industry and from basic to applied science. Given this importance, and despite the already high number of existing technologies, there is still a need for new types of X-ray detectors offering increasingly better performance. One of the most recent innovations in X-ray detection is the *hybrid pixel technology*.

A hybrid pixel detector is composed of two parts: a high resistivity semiconductor layer and a CMOS readout chip. Both structures are segmented into corresponding matrices of diodes and readout cells. Each diode is connected to a readout cell via a small sphere of conducting material. The charge created in a given diode by ionizing radiation that hits the semiconductor sensor, is collected by the corresponding readout cell. A more detailed discussion of pixel devices is presented in Chapter 3.

At first instance, hybrid pixel detectors were not developed for photon imaging, but for use in high energy physics. In a typical particle physics experiment, two beams of particles collide. Some of the colliding particles may interact, and this often results in the creation of other, *secondary*, particles. From the study of these interactions and the behaviour of the secondary particles, it is possible to find confirmation of or flaws in existing theories. Thus, the goal of the experimentalist is to efficiently detect these particles.

A high energy physics experiment consists of a series of sub-systems, each one designed to detect a specific class of particles, or capable of measuring a specific property (energy of the particle, trajectory, etc.). Pixel detectors are employed to determine the exact position of the primary interaction, where a particle decays into other particles (*vertexing*), and to measure the trajectory of charged particles (*tracking*). Given their high spatial resolution and capability to deal with high counting rates, hybrid pixel detectors are nowadays preferred over other technologies.

The Medipix collaboration was created in 1995 to transfer hybrid pixel technology from high energy physics to X-ray imaging. The collaboration developed two CMOS ASICs: the Medipix1 (1996) and the Medipix2 (2002). Several types

of semiconductor X-ray sensors have been studied in combination with the chips. In the course of years, numerous tests have been performed and several applications of the Medipix detectors have been investigated with success, proving that hybrid pixel technology has a high potential also in the field of X-ray imaging.

This thesis summarizes several characterization measurements performed on Medipix1 and Medipix2 detectors. New applications of the Medipix2 chip are presented. In Chapter 1, basic processes of interaction between particles and matter are discussed. The focus is placed on the physics of photons and charged particles traversing a sample of material. In Chapter 2, X-ray imaging systems are presented. The most common parameters for image evaluation are introduced and a simple classification of detectors is made. Chapter 3 introduces hybrid pixel detectors and the Medipix1 chip. A typical Medipix1 setup is described. Chapter 4 presents an extensive characterization of the Medipix1 detector, based on the data acquired at the European Synchrotron Radiation Facility (ESRF).

In Chapter 5, the Medipix2 detector is presented, with information on design, experimental setup and testing. Chapter 6 describes a large-area application of the Medipix2 chip. Several Medipix2 chips have been tiled together into a detector array. Finally, in Chapter 7 a new application of the Medipix2 chip is presented. Instead of being connected to a semiconductor sensor, the chip is coupled to a *Gas Gain Grid* and used as readout system in a prototype gas-ionization tracking detector. This application is aimed at high energy physics experiments: from X-ray imaging, back again to particle physics.

Chapter 1

Interaction of particles with matter

In this chapter an overview of the most important processes of interaction of particles with matter is given.

Several types of ionizing radiation exist:

- Charged particles (relativistic or non-relativistic)
- Photons

The detection of these ionizing particles is of particular interest for many purposes:

- Fundamental science (high energy physics, astronomy, etc.)
- Applied science (X-ray crystallography, determination of the 3-dimensional structure of macro-molecules, etc.)
- Medical applications (transmission radiography, biomedical and biological structural analysis, emission radiography)
- Industrial applications (sample analysis through X-ray fluorescence or diffraction, transmission imaging)

Section 1.1 gives an introduction to the most important interaction processes of photons in matter, while section 1.2 provides an overview of the interaction of charged particles with matter.

1.1 Photon interaction processes

In this section the interaction of X-ray photons with matter will be studied. The dominant processes are the following:

- Photoelectric effect: the photon is absorbed by an atomic electron, which is then ejected from the atom
- Compton scattering (including Thomson and Rayleigh scattering): predominantly scattering of photons on free electrons
- Pair production: the photon converts into an electron-positron pair

These processes will be discussed in more detail in the following sections. Fig. 1.1 shows the contributions of these processes to the total photon interaction cross section in the case of carbon and lead. For photon energies below 500 keV the interactions are primarily due to the photoelectric effect, while for photon energies above 50 MeV the dominant effect is pair production in the electromagnetic field of the atomic nucleus. Compton scattering plays an important role in the intermediate energy range.

If we consider the basic properties of these three process, we can immediately explain the two principal qualitative features of the interaction of photons with matter:

- X-ray and γ-ray photons are much more penetrating in matter than charged particles. This is due to the much smaller cross section of the three processes mentioned above with respect to the Coulomb interaction between the charged particles.
- A beam of photons passing through matter is attenuated in intensity, but is not significantly degraded in energy. This is due to the fact that two of the three above processes (photoelectric effect and pair production) entirely remove the photon from the beam, either by absorption or scattering. The photons that pass straight through, therefore, are those that have not suffered any interactions at all, and so they retain their original energy. However, the total number of photons (hence the beam intensity) is reduced by the number of photons which have interacted. Only photons that have interacted through a Compton scattering process have sustained an energy loss (see section 1.1.2).

It is interesting to calculate the intensity attenuation suffered by a photon beam passing through matter. Consider a collimated, mono-energetic beam of N photons. The number of x- or γ-rays removed from the beam while crossing a sample of thickness dx of a certain material is:

$$dN = -\mu N dx \tag{1.1}$$

The constant of proportionality μ is known as the *total attenuation coefficient*, and it is the probability per unit length that a photon will be scattered by or absorbed in the material. This means that this coefficient is related to the cross sections of the processes mentioned above.

The total cross section per atom is the following:

$$\sigma_{tot} = \sigma_{p.e.} + Z\sigma_C + \sigma_{pair} \tag{1.2}$$

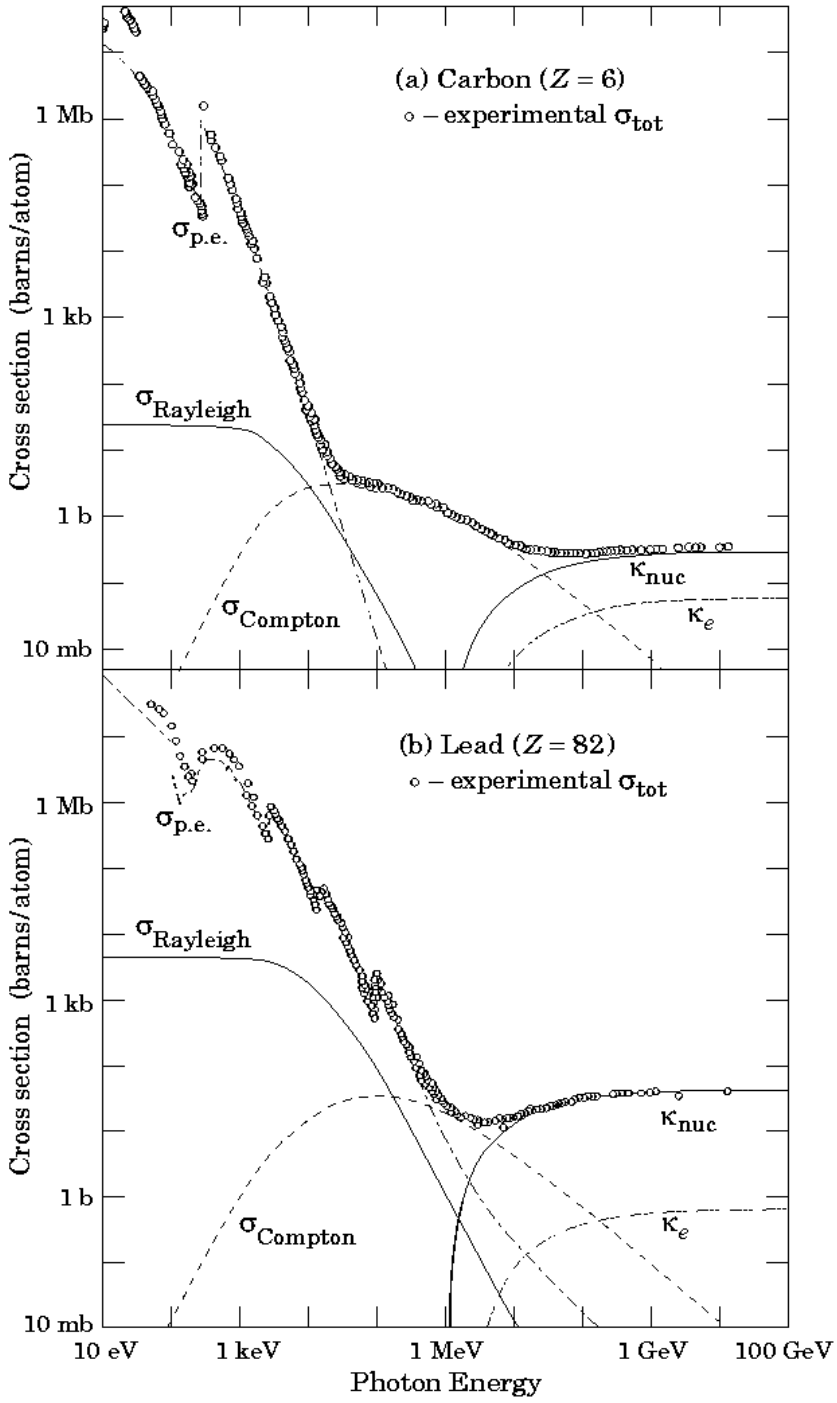

Figure 1.1: Contributions to the photon interaction cross section in carbon (a) and lead (b). Here $\sigma_{p.e.}$ is the atomic photoelectric effect cross section; σ_R, the Rayleigh scattering; σ_C, Compton scattering; σ_{nuc}, pair production off the nucleus field; σ_e pair production from the field of atomic electrons [1].

($\sigma_{p.e.}$ = photoelectric cross section, σ_C = Compton cross section and σ_{pair} = pair production cross section). Here we have multiplied the Compton cross section by Z to take into account the Z electrons present in the atom. If we now multiply σ_{tot} by the density of atoms n, we obtain the probability per unit length for an interaction:

$$\mu = \sigma_{tot} n = \sigma_{tot}(N_a \rho / A) \tag{1.3}$$

where N_a is Avogadro's number, ρ is the density of the material and A is the atomic weight.

Integrating eqn.1.1 we obtain that the fraction of photons still present in the beam at a distance x inside the material is:

$$N(x) = N_0 e^{-\mu x} \tag{1.4}$$

where N_0 is the initial number of photons present in the beam. We can also write this equation in terms of the beam intensity:

$$I(x) = I_0 e^{-\mu x} \tag{1.5}$$

$I(x)$ is the beam intensity after passing through a distance x in the material, and I_0 is the initial intensity of the beam.

The following sections contain a more detailed description of the main interaction processes of photons in matter mentioned above.

1.1.1 Photoelectric effect

For photon energies below 500 keV the most important process of interaction with matter is the photoelectric effect. This mechanism involves the absorption of a photon by an atomic electron with the subsequent ejection of the electron from the atom. The energy of the outgoing electron is:

$$E = h\nu - E_B \tag{1.6}$$

where E_B is the binding energy of the electron.

Fig. 1.2 shows a typical photoelectric cross section, as a function of the energy of the incident photon. As can be seen, at energies above the highest electron binding energy of the atom (the K shell), the cross section is relatively small but it increases rapidly as the K-shell energy is approached. Just after this point, the cross section drops drastically since the K-electrons are no longer available for the photoelectric effect. This drop is known as the K absorption edge. Below this energy, the cross section rises once again and the edge behavior is repeated at lower energies when the L, M etc. levels are passed. These are known respectively as the L-absorption edges (due to sub-shells, the L edge actually consists of several edges), M-absorption edge and so on.

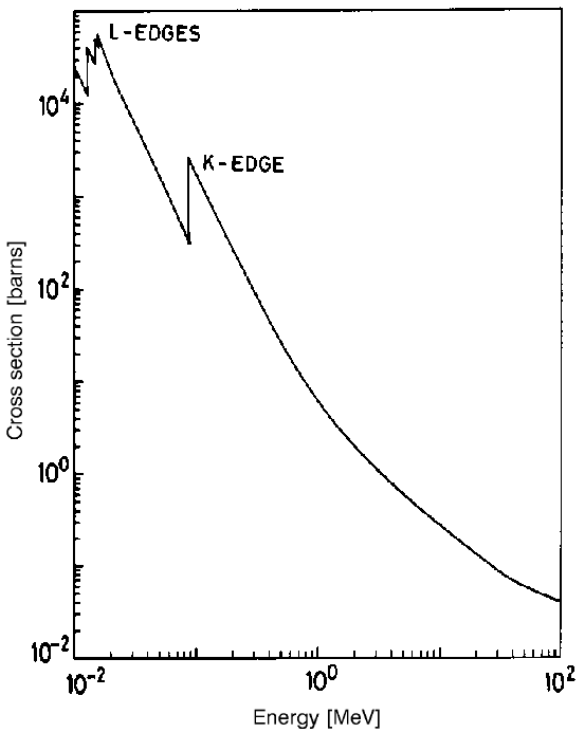

Figure 1.2: Typical photoelectric cross section as a function of the incident photon energy. These values have been calculated for lead [2].

From a theoretical point of view, it is difficult to rigorously calculate the photoelectric cross section because of the complexity of the Dirac wave-functions for the atomic electrons. However, for photon energies above the K-edge it is almost always the electrons on the K shell that are involved. If this is assumed and the energy is non-relativistic (i.e. $h\nu << m_e c^2$), the cross section can be calculated using a Born approximation. For an atom:

$$\sigma_{p.e.} = 4\alpha^4 \sqrt{2} Z^5 \Phi_0 \left(\frac{m_e c^2}{h\nu} \right)^{7/2} \tag{1.7}$$

where $\Phi_0 = 8\pi r_e^2/3 = 6.651 \times 10^{-25}\text{cm}^2$, r_e is the classical range of the electron and $\alpha = 1/137$ is the fine structure constant. For energies closer to the K-edge more complicated correction factors have to be included in the above expression for $\sigma_{p.e.}$. Formulas for the L- and M-edges have also been calculated, but they are more complicated [3].

It is interesting to study the dependence of the cross section on the atomic

number Z. In our first approximation it goes as Z^5, if higher order corrections are introduced the dependence is not so simple anymore and it behaves approximately as Z^4. Then it is clear that high Z materials are the most favored for photoelectric absorption, and the choice of the material is of critical importance when building a photon detector that exploits the photoelectric effect to convert photons into electrons.

1.1.2 Compton scattering

Compton scattering is important for photon energies between 500 keV and 50 MeV. The denomination *Compton scattering* indicates the incoherent scattering of photons on a free electron gas. In matter, electrons are normally bound in the atoms. However, if the photon energy is high with respect to the binding energy, then the electron can be considered approximately free.

A Compton process is illustrated in fig. 1.3. By simply applying conservation of momentum and energy, the energy of the scattered photon can be easily calculated:

$$k' = \frac{k}{1 + \frac{k}{m_e c^2}(1 - cos\theta)} \tag{1.8}$$

where $k = h\nu$ is the energy of the incident photon, and $k' = h\nu'$ is the energy of the scattered photon. The scattered photon transfers a fraction of its energy to the recoiling electron:

$$T = k - k' \tag{1.9}$$

The maximum electron recoil energy allowed by kinematics is given by:

$$T_{max} = k\left(\frac{2\gamma}{1 + 2\gamma}\right) \tag{1.10}$$

where $\gamma = k/m_e c^2$. T_{max} it is called *Compton edge* (see fig. 1.4).

The cross section for Compton scattering was one of the first to be calculated using quantum electrodynamics (QED) and it is known as the *Klein-Nishina formula*:

$$\frac{d\sigma_C}{d\Omega} = \frac{r_e^2}{2}\frac{1}{[1 + \gamma(1 - cos\theta)]^2}\left(1 + cos^2\theta + \frac{\gamma^2(1 - cos\theta)^2}{1 + \gamma(1 - cos\theta)}\right) \tag{1.11}$$

where Ω is the solid angle, r_e is the classical electron radius and the angle θ is indicated in fig. 1.3. Integrating over $d\Omega$ we obtain the total Compton scattering cross section:

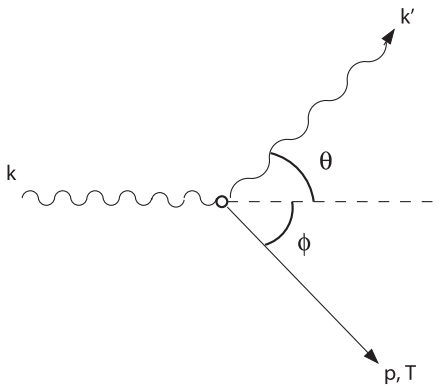

Figure 1.3: The Compton scattering process: a photon with initial momentum equal to k_0 is scattered off an electron. The scattered photon has a momentum $k' < k$. θ is the scattering angle.

$$\sigma_C = 2\pi r_e^2 \left(\frac{1+\gamma}{\gamma^2} \left(\frac{2(1+\gamma)}{1+2\gamma} - \frac{1}{\gamma} ln(1+2\gamma) \right) + \frac{1}{2\gamma} ln(1+2\gamma) - \frac{1+3\gamma}{(1+2\gamma)^2} \right) \tag{1.12}$$

Since there are Z electrons per atom, it follows that the Compton cross section is proportional to Z.

Related to the Compton scattering are the two classical processes of *Thomson* and *Rayleigh* scattering. Thomson scattering is the scattering of photons off free electrons in the classical limit. In fact, at low energies with respect to the electron mass the Klein-Nishina formula for Compton scattering reduces to the classical Thomson cross section:

$$\sigma_T = \frac{8\pi}{3} r_e^2 \tag{1.13}$$

Rayleigh scattering is instead the scattering of photons off atoms as a whole. In this process all the electrons of the atom participate, and for this reason it is also called *coherent* scattering.

Both processes are characterized by the fact that no energy is transferred to the medium. The atoms are neither ionized nor excited, and only the direction of the photon is changed. At the relatively high energies of X-rays and γ-rays, however, Thomson and Rayleigh scattering are small, and for most purposes can be safely neglected.

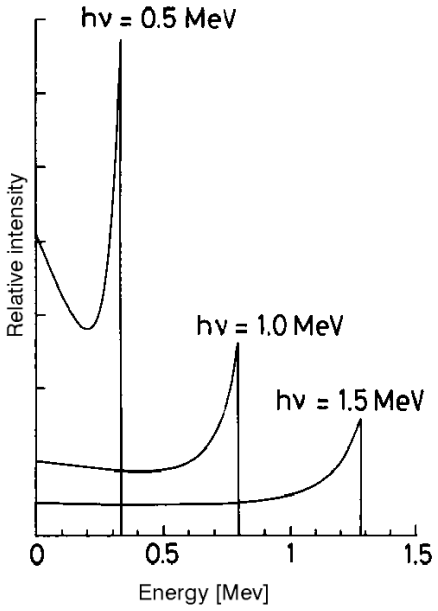

Figure 1.4: Energy distribution of Compton recoil electrons, for different energies of the incident photon hν. The sharp drop at the maximum recoil energy is known as Compton edge *[2].*

1.1.3 Pair production

The third process of interaction of photons with matter is pair production, which involves the transformation of a photon into an electron-positron pair. Two conditions must be satisfied for this process to be possible:

- To conserve momentum, pair production can only occur in the presence of a third body, usually a nucleus, or even an atomic electron
- To produce an electron-positron pair, the photon energy needs to be higher than a certain threshold. This threshold is equal to the electron mass plus the positron mass in the case of production in the nucleus field, or to twice this amount for production in an atomic electron field (due to the recoil of the atomic electrons):

$$E_{Th,Nuc} = 2m_e c^2 = 1.022 MeV \tag{1.14}$$

$$E_{Th,el.} = 4m_e c^2 = 2.044 MeV \tag{1.15}$$

Pair production becomes the predominant process of interaction for photon energies above 50 MeV.

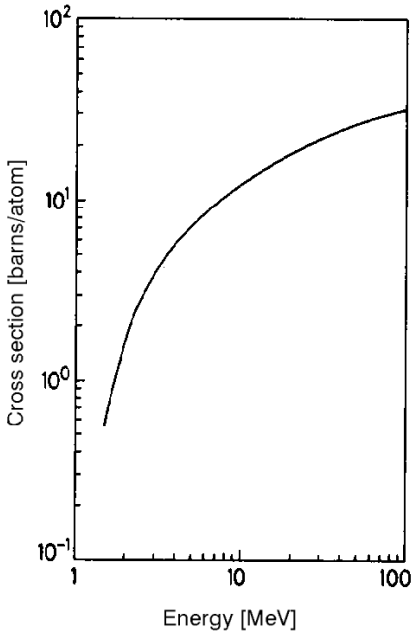

Figure 1.5: Calculated pair production cross section for lead (according to eqn. 1.16) [2].

The cross section for pair production can be computed numerically. However, by using a few assumptions we can obtain an analytical expression. If we take into account only relativistic energies, and if we neglect any screening effect of the atomic electrons surrounding the nucleus, we obtain:

$$\sigma_{nuc} = 4Z^2\alpha r_e^2 \left(\frac{7}{9}\left(ln\frac{2h\nu}{m_e c^2} - f(Z)\right) - \frac{109}{54}\right) \tag{1.16}$$

where $h\nu$ is the photon energy, $\alpha = 1/137$ is the fine structure constant, and f(Z) is a Coulomb correction. We note that for high energies the pair production cross section goes as Z^2. An example of pair production cross section is shown in fig. 1.5 in the case of lead.

1.2 Energy loss of charged particles in matter

Before entering the details of energy loss of charged particles in matter, we note that it is convenient to group charged particles into three different classes depending on their mass:

- Electrons and positrons

- Charged particles (muons, pions, protons, α particles and light nuclei up to ^{4}He)

- Heavy ions (medium sized and heavy nuclei)

For each class, different effects and approximations have to be taken into account. This section will discuss the details of the energy loss of charged heavy particles, while the energy loss of electrons and positrons will be treated in the next section. Heavy ions will not be discussed in this chapter because of complicated additional effects that arise, and because the other two cases are of more interest for the subject of this thesis.

In general, two principal features characterize the passage of charged particles through matter: a loss of energy by the particle and a deflection of the particle from its incident direction. These effect are primarily the result of two electromagnetic processes of atomic collision:

- Collisions with the atomic electrons of the material

- Elastic scattering from nuclei

These reactions occur many times per unit path length in matter and it is their cumulative result that accounts for the two principal effects observed. However, these are not the only possible processes that can occur to a charged particle traversing some amount of material. Other important processes include:

- Emission of Cerenkov radiation

- Nuclear reactions

- Bremsstrahlung

However, these reactions are relatively rare compared to the atomic processes, and will not be discussed in this chapter.

Of the two electromagnetic processes, the inelastic collisions with the atomic electrons are almost exclusively responsible for the energy loss of heavy charged particles in matter. In these collisions, the incident particle interacts with the atomic electrons from the material, and energy is transferred from the particle to the atom causing an excitation or an ionization. The amount transferred in each collision is usually a small fraction of the total energy of the particle. However, the number of collisions per unit length is so large that a cumulative energy loss is observed even in relatively thin layers of material. Atomic collisions are usually divided into two different groups:

- *Soft collisions* in which only an atomic excitation results

- *Hard collisions* in which the atom in ionized

In some of the *hard* processes enough energy is transferred such that the ionization electron is in turn capable of ionizing other atoms, causing often substantial secondary ionization. These high-energy recoil electrons are known as *δ-rays* or *knock-on electrons*.

Elastic scattering from nuclei also occurs frequently, although not as often as electron collisions. In general, only a small amount of energy is transferred in these processes, because the masses of the nuclei in most materials are usually very large compared to the incident particle. The largest part of the energy loss is due to atomic electron collisions.

1.2.1 The Bethe-Bloch formula

Collisions are of course statistical in nature, occurring with a certain quantum mechanical probability. However, since their number per macroscopic path length is extremely large, the fluctuations in the energy loss are small, so that the average energy loss per unit length is a useful quantity to be taken into account. The correct quantum-mechanical calculation was first performed by Bethe, Bloch and other authors. In this calculation the energy transfer is parametrized in terms of momentum transfer. The formula obtained is:

$$\frac{-dE}{dx} = 2\pi N_a r_e^2 m_e c^2 \rho \frac{Z}{A}\frac{z^2}{\beta^2}(ln\frac{2m_e\gamma^2 v^2 W_{max}}{I^2} - 2\beta^2 - \delta - 2\frac{C}{Z}) \qquad (1.17)$$

where:

r_e = classical electron radius = 2.817×10^{-13} cm
m_e = electron mass
N_a = Avogadro's number = $6.022 \times 10^{23} mol^{-1}$
I = mean excitation potential
Z = atomic number of the material
A = atomic weight of the material
ρ = density of the material
z = charge of the incident particle in units of e
$\beta = v/c$ of the incident particle
$\gamma = 1/\sqrt{1-\beta^2}$
δ = density correction
C = shell correction
W_{max} = maximum energy transfer in a single collision

The maximum energy transfer is the energy transfer produced by a head-on collision, and for an incident particle of mass M, kinematics calculations give:

$$W_{max} = \frac{2m_e c^2 \eta^2}{1 + 2s\sqrt{1+\eta^2+s^2}} \qquad (1.18)$$

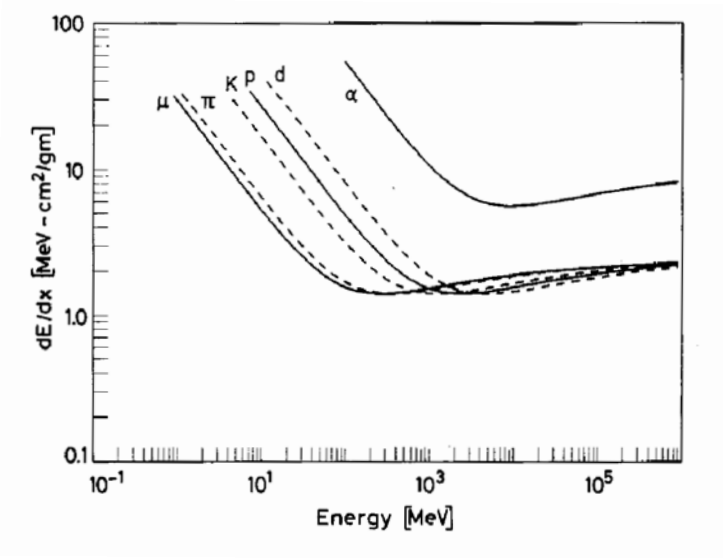

Figure 1.6: The energy loss dE/dx as function of energy for several different particles [2].

where s $= m_e/M$ and $\eta = \beta\gamma$. If $M >> m_e$ we can approximate to:

$$W_{max} = 2m_e c^2 \eta^2 \tag{1.19}$$

We also note that $2\pi N_a r_e^2 m_e c^2 = 0.1535 MeV cm^2/g$ so that the Bethe-Bloch formula can be rewritten in a more practical form:

$$\frac{-dE}{dx} = 0.1535 MeV cm^2/g \; \rho \frac{Z}{A} \frac{z^2}{\beta^2} (ln \frac{2m_e \gamma^2 v^2 W_{max}}{I^2} - 2\beta^2 - \delta - 2\frac{C}{Z}) \tag{1.20}$$

The mean excitation potential I is a difficult quantity to calculate. Values of I for several materials have been deduced from actual measurements of dE/dx and semi-empirical formulas for I as a function of Z have been fitted to the points. More information can be found in [4, 5]. In fig. 1.6 the Bethe-Bloch formula eqn. 1.17 is plotted as a function of kinetic energy for several different particles.

The density correction δ is important at high energies. It arises from the fact that the electric field of the particle tends to polarize the atoms along its path. Because of this polarization, electrons far from the path of the particle will be shielded from the full electric field intensity. Interactions with these outer-lying electrons will contribute less to the total energy loss than predicted by the

Bethe-Bloch formula. It is clear that this effect depends on the density of the material, since the induced polarization will be greater in condensed materials than in lighter substances such as gases.

The shell correction C accounts for effects that arise when the velocity of the incident particle is comparable or smaller than the orbital velocity of the bound atomic electrons (thus, this correction is important for low energies).

1.2.2 Energy dependence of the energy loss

At non-relativistic energies, dE/dx is dominated by the overall $1/\beta^2$ factor and decreases with increasing velocity until about v=0.96c, where a minimum is reached. Particles at this point are known as *minimum ionizing particles* or simply *MIP*. Note that the minimum value of dE/dx is almost the same for all the particles of the same charge.

As the energy increases beyond the minimum ionizing point, the term $1/\beta^2$ becomes almost constant and dE/dx rises again due to the logarithmic dependence of the Bethe-Bloch formula. This *relativistic rise* is, however, opposed by the density correction. In this rise zone, different particles show more or less the same value for the energy loss.

For energies below the minimum ionizing point, each particle exhibits a dE/dx that is usually distinct from the other particle types, being dependent on its squared charge/velocity ratio $(Z/\beta)^2$ accordingly to the Bethe-Bloch formula eqn. 1.17. This behaviour is often exploited in particle physics experiments to identify different types of particles.

From fig. 1.7 we see that as a heavy particle slows down while traversing a material, its rate of energy loss will change. In particular it will start to lose more energy per unit length when it reaches the zone below the minimum ionizing value. Fig. 1.7 shows the amount of ionization created by a heavy particle as a function of the length of the path traversed inside the material. This is known as the Bragg curve, and, as can be seen, most of the energy is deposited near the end of the trajectory. At the end of the trajectory, however, the β of the particle becomes small and the dE/dx also drops quickly.

1.2.3 Range

Consider now a beam of monoenergetic particles, crossing a certain homogeneous material. We would expect that all the particles will lose all their energy after having penetrated the same thickness of matter, but this is not in fact true. The penetration range can be measured by sending a monoenergetic beam through samples of the material, each one with a different thickness, and measuring the ratio of transmitted to incident particles. This ratio is plotted versus the absorber thickness. The resulting curve (see fig. 1.8) does not show a sharp drop to background level, but a slope over a certain range of thickness.

This result is due to the fact that the process of energy loss is not continuous but statistical in nature. Two identical particles from the same monoenergetic beam will in general suffer a different number of collisions (and thus a different

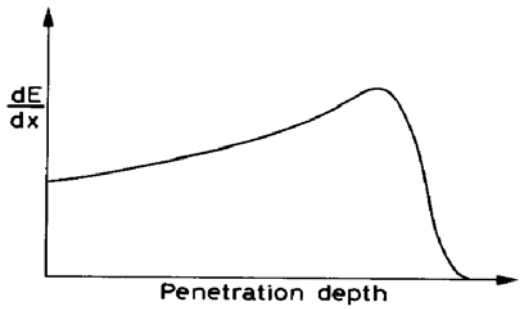

Figure 1.7: A typical Bragg curve showing the variation of dE/dx as a function of the penetration depth of the particle in matter. The particle is more ionizing toward the end of its path [2].

energy loss) while crossing the same thickness of matter. This phenomenon is known as *range straggling*, and the spread has a gaussian shape. The mean value of this distribution is known as *mean range*, and it indicates the thickness at which about half of the particles are absorbed (see fig. 1.8).

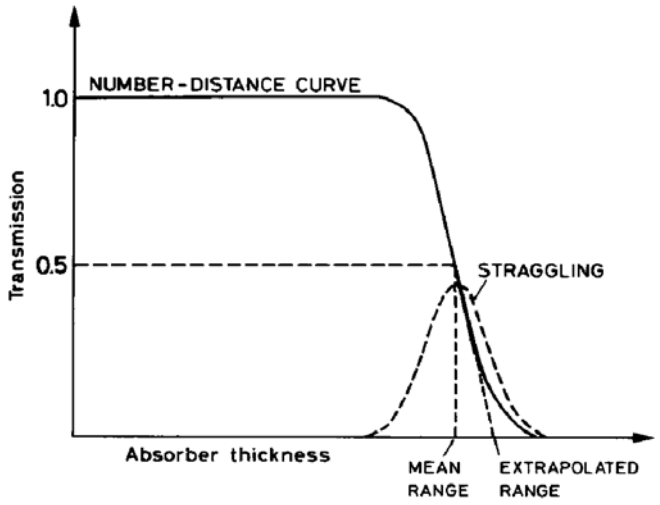

Figure 1.8: Transmission probability distribution as function of material thickness. The straggling function can be approximated by a Gaussian [2].

1.3 Energy loss of electrons and positrons

Like heavy charged particles, electrons and positrons also lose energy by collisions with atomic electrons when passing through matter. However, another mechanism of energy loss is also present. Because of their small mass, the emission of electromagnetic radiation arising from scattering in the electric field of a nucleus (*bremsstrahlung*) has to be taken into account. At incident energies of a few MeV, this effect still plays a small role. However, as the energy increases, bremsstrahlung radiation becomes the dominant process (see fig. 1.9).

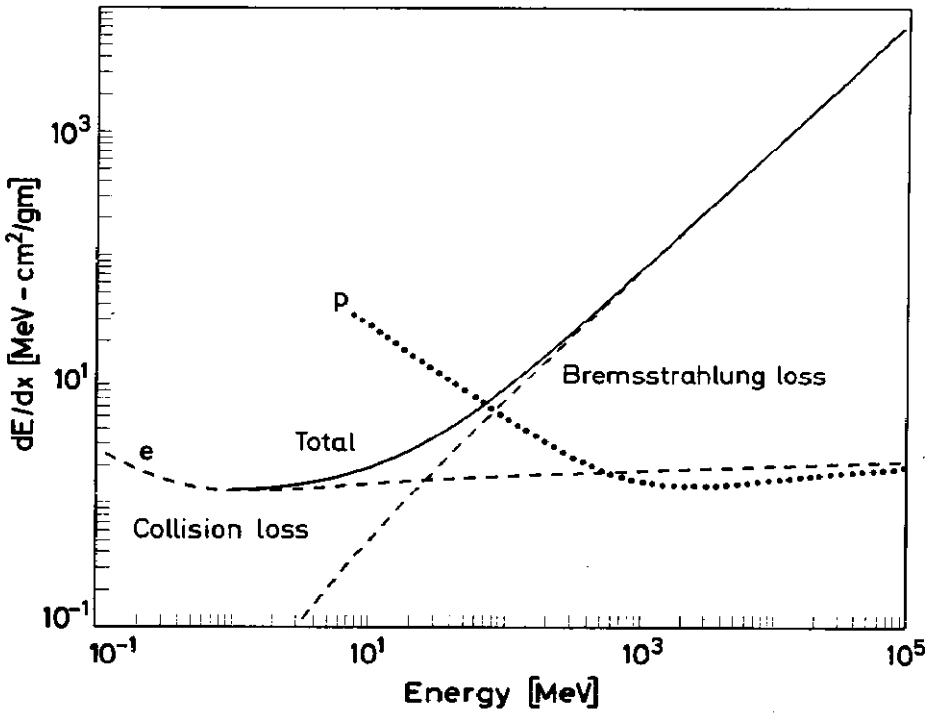

Figure 1.9: Energy loss from collision and from bremsstrahlung for electrons in copper. For comparison, the dE/dx for protons is also shown [2].

1.3.1 Energy loss by atomic collisions

In the case of electrons and positrons, the Bethe-Bloch formula has to be modified to take into account two effects:

- Eqn. 1.17 is derived under the assumption that the incident particle remains undeflected during the collision, but this is not valid anymore because of the small value of the electron mass
- In the case of an incident electron, the collision with the atomic electron is between two identical particles, which gives rise to quantum mechanical exchange effects

The correct calculation gives:

$$\frac{-dE}{dx} = 2\pi N_a r_e^2 m_e c^2 \rho \frac{Z}{A}\frac{1}{\beta^2}\left(ln\frac{\tau^2(\tau+2)}{2(I/m_e c^2)^2} + F(\tau) - \delta - 2\frac{C}{Z}\right) \tag{1.21}$$

where τ is the kinetic energy of the particle in units of $m_e c^2$. The function $F(\tau)$ describes the different behaviour of electrons and positrons:

$$F(\tau) = 1 - \beta^2 + \frac{\frac{\tau^2}{8} - (2r+1)ln2}{(\tau+1)^2} \quad for \;\; e^- \tag{1.22}$$

$$F(\tau) = 2ln2 - \frac{\beta^2}{12}(23 + \frac{14}{\tau+2} + \frac{10}{(\tau+2)^2} + \frac{4}{(\tau+2)^3}) \quad for \;\; e^+ \tag{1.23}$$

The other quantities are as described in eqn. 1.17.

1.3.2 Energy loss by radiation (bremsstrahlung)

The dominant mechanism of energy loss for high energy electrons is the production of electromagnetic radiation. This is known as bremsstrahlung in the case of passage through matter, synchrotron radiation in the case of circular acceleration and cyclotron radiation if the electrons are non-relativistic.

A semiclassical calculation of the bremsstrahlung process for a relativistic particle of charge e interacting with the Coulomb field generated by a nucleus of atomic number Z gives the following result:

$$\frac{d\sigma}{dk} = 5Z^2 {r_e}^2 \alpha \left(\frac{m_e c}{Mv}\right)^2 \frac{{r_e}^2}{k} ln\frac{Mv^2\gamma^2}{k} \tag{1.24}$$

where k is the energy of the produced photon, and M and v respectively are the mass and speed of the incident particle. The mass of the incident particle appears in this equation with an inverse square dependence. This means that the bremsstrahlung radiation loss for a muon ($M = 106$ MeV), the lightest particle after the electron, is about 40000 times smaller than that of electrons and positrons. Because of this, bremsstrahlung effects are usually not taken into account for heavy charged particles. We also note that this cross section depends on the material through the factor Z^2, which means that heavy elements are

Material	Critical Energy (MeV)
Pb	9.51
Al	51.0
Fe	27.4
Cu	24.8
Water	92
Air (STP)	102
NaI	17.4
Polystyrene	109

Table 1.1: Critical energies for some materials.

more efficient at causing energy loss by radiation (while ionization energy loss is proportional to Z, see also eqn. 1.17).

However, corrections must be made to eqn. 1.24 to take into account other effects due to the presence of atomic electrons. The electric field generated by these electrons also causes the incident particle to emit radiation, but since this effect is proportional to Z and not to Z^2 it can in general be neglected for all but the lightest elements. A more important contribution of the atomic electrons is their screening of the nuclear charge, for which corrections are calculated numerically.

1.3.3 Critical energy and radiation length

As we have seen the energy loss by radiation depends strongly on the nuclear charge Z of the absorbing material. For each material, we can define a critical energy E_c at which the radiation loss equals the collision loss:

$$\frac{dE}{dx}_{rad} = \frac{dE}{dx}_{coll} \quad for \quad E = E_c \tag{1.25}$$

Above this energy, radiation loss will dominate over collision-ionization losses, and vice-versa below E_c (see also fig. 1.9). An approximate formula for the critical energy is the following:

$$E_c = \frac{800\ MeV}{Z + 1.2} \tag{1.26}$$

The values of the critical energy for a few materials are given in table 1.1.

Another useful parameter is the quantity known as *radiation length* L_{rad}, defined as the distance over which the electron energy is reduced by a factor $1/e$ due to radiation loss only. In the high energy limit, the loss due to collisions

Material	L_{rad}(gr/cm^2)	L_{rad}(cm)
Air (STP)	36.20	30050
Water	36.08	36.1
NaI	9.49	2.59
Pb	6.37	0.56
Cu	12.86	1.43
Al	24.01	8.9
Fe	13.84	1.76
BGO	7.98	1.12
Polystirene	43.80	42.9
Si	21.62	9.4
GaAs	12.19	2.3
CdTe	8.85	1.5

Table 1.2: Radiation lengths for some materials.

can be neglected with respect to the radiation loss. The energy of an electron that traversed a material of thickness x is given by:

$$E = E_0 \, e^{-x/L_{rad}} \tag{1.27}$$

An approximate formula for the radiation length is the following:

$$\frac{1}{L_{rad}} = 4Z(Z+1)\frac{\rho N_a}{A} r_e^2 \alpha (ln(183Z^{-1/3}) \tag{1.28}$$

For quick calculations, the following can be useful [6]:

$$L_{rad} = \frac{716.4 g/cm^2 \, A}{Z(Z+1)ln(287/\sqrt{Z})} \tag{1.29}$$

The values obtainable in this way are accurate to within 2.5% except for helium where the result is about 5% too low. The values of the radiation lengths for a few materials are listed in table 1.2.

1.4 Conclusions

In this chapter, an overview of the main processes of interaction between particles and matter is given. For our field of research, two categories of radiation are of particular interest:

- Photons, in the energy range 4 - 100 keV (soft and hard X-rays)

- Charged particles, with an energy up to several TeV

Photons are of primary interest in X-ray imaging. An introduction to imaging is given in next chapter, and a new technique for X-ray detection (the Medipix hybrid pixel detectors) will be described in chapters 3, 4, 5 and 6. In chapter 7, a new system for detection of charged particles in high energy physics experiments is presented.

An exhaustive compendium of all the phenomena introduced in this chapter can be found in [2].

Chapter 2

Introduction to X-ray imaging

This chapter deals with general characteristics of X-ray imaging and ways of evaluating detector performance. A complete overview of existing imaging systems is outside the scope of this thesis. Thus, only an introduction to the parameters most commonly used for image quality evaluation will be given, together with a basic classification of the existing technologies employed in X-ray detection. Advantages and disadvantages of the different categories of detectors will be described, in order to clarify the choices made that led to the development of Medipix hybrid pixel detectors.

2.1 Image characterization

The quality of an image can be evaluated in terms of a number of parameters, the most important of which will be described in the following sections. The image quality, and, ultimately, the fact that a feature has been successfully detected or not, does not depends uniquely on the process of image formation and on the characteristics of the imaging detector. Other important factors are, for instance, image processing, optimum image display and the skill and experience of the human observer. This section will give only a first introduction to the physical image evaluation parameters.

2.1.1 Spatial resolution

The spatial resolution of an imaging system is the ability of the system to register separate images of two closely situated objects (see fig. 2.1).

The resolution of the system is usually measured using a test object with alternating transparent and absorbing lines. The resolution power is then given in line pairs per millimeter (lp/mm), i.e, it gives the number of "tops" and "valleys" that can be detected per millimeter. For instance, if the system is

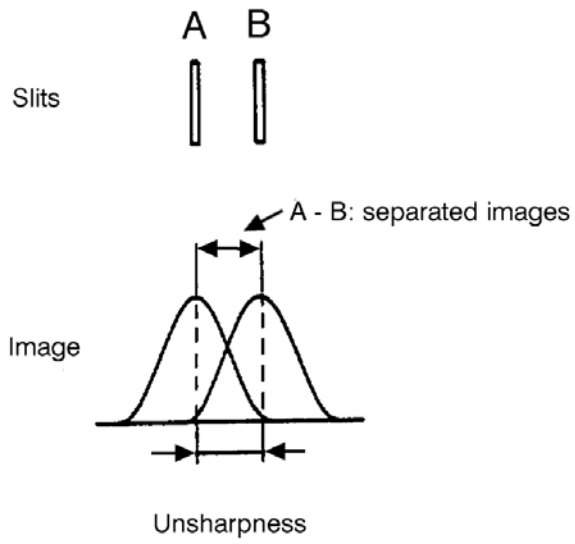

Figure 2.1: The resolution of an imaging detector is the ability to register separate images of two closely situated objects.

capable of visualizing a pattern with 100 μm wide bars alternated to 100 μm wide spacings, its spatial resolution is 1/(0.1+0.1)=5 lp/mm.

2.1.2 Signal-to-noise ratio

The *signal-to-noise ratio* (SNR) is defined as the ratio between the fraction of the output signal (voltage or current or charge) that is directly related to the information of interest (signal) and the fraction of output that does not contain information (noise).

The SNR is a good indicator for image quality. In an imaging system the quality of a image is determined not only by the quality of the recorded signal, but also by the noise level. Noise fluctuations can mask real fluctuations, so care should be taken of reducing noise as much as possible.

2.1.3 Image contrast

In a X-ray image, the various intensities transmitted by the specimen are rendered as different densities in the image. The density differences from one area to another constitute radiographic contrast. Any shadow or detail within the image is visible thanks to the contrast between it and its background of surrounding structures. Within appropriate limits, with greater contrast or density

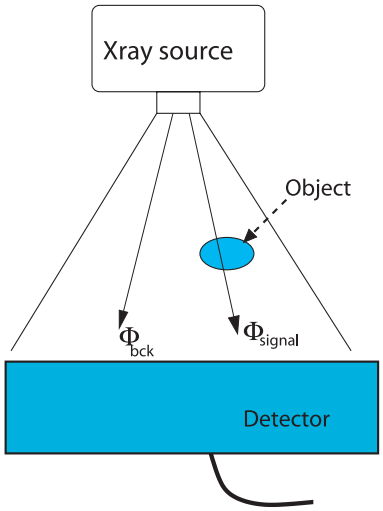

Figure 2.2: The difference between the measured photon fluencies Φ_{bkg} and Φ_{signal} determines the image contrast.

differences in the radiograph, the details will stand out in a more pronounced way.

A common definition of the *image contrast* of a signal is the following:

$$C = \frac{|\Phi_{signal} - \Phi_{bkg}|}{\Phi_{bkg}} \tag{2.1}$$

where Φ_{signal} is the flux of photons detected in an area of the image covered by the object to be imaged, and Φ_{bkg} is the flux of photons detected in an area of the image where the object is not present. For a completely opaque object, Φ_{signal} is equal to 0 and so the contrast is equal to 1. If no object is present Φ_{signal}=Φ_{bkg} and the contrast is equal to 0.

2.1.4 Detective quantum efficiency

In general, for a given imaging system, the signal-to-noise ratio of the output SNR_{out} is lower than the SNR at its input (SNR_{in}). The squared ratio of these two quantities is called *detective quantum efficiency* (DQE) and describes how the input SNR_{in} is transferred to the output:

$$DQE = \frac{SNR_{out}^2}{SNR_{in}^2} \tag{2.2}$$

The DQE assumes values between 0 and 1. An ideal detector would extract all the information from the incident beam, so SNR_{out}^{ideal}=SNR_{in}^{ideal} and thus DQE=1.

If the imaging system is composed by several different subsystems, the total DQE is the product of the individual DQEs of all the subdetectors. Thus, the DQE of a complete system is never better than the DQE of its weakest component.

In a direct detection system (see section 2.2.2) the DQE is essentially determined by the absorption efficiency of the sensor only.

2.1.5 PSF, LSF and ESF

The quality of the image depends fundamentally on the ability of the imaging system to reproduce each single point in the object.

The *point spread function* (PSF) [7] is defined as the distribution in absorbed energy (per unit area) in the image plane when the imaging system is irradiated through a vanishingly small aperture (see fig. 2.3).

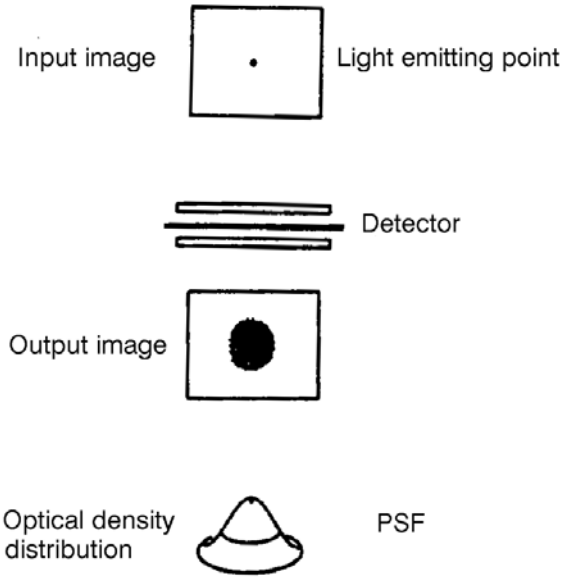

Figure 2.3: The point spread function, PSF.

The object can be considered as composed of an infinite number of points. The imaging system reproduces the points in the object with unsharp points in the image, as shown in fig. 2.4. This is why the point spread function is of such fundamental importance in describing the properties of an imaging detector.

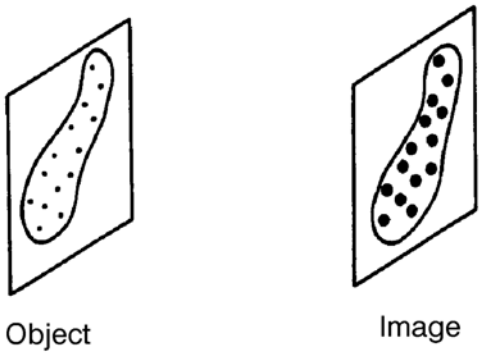

Figure 2.4: The image of an object is composed of unsharp images of the object points.

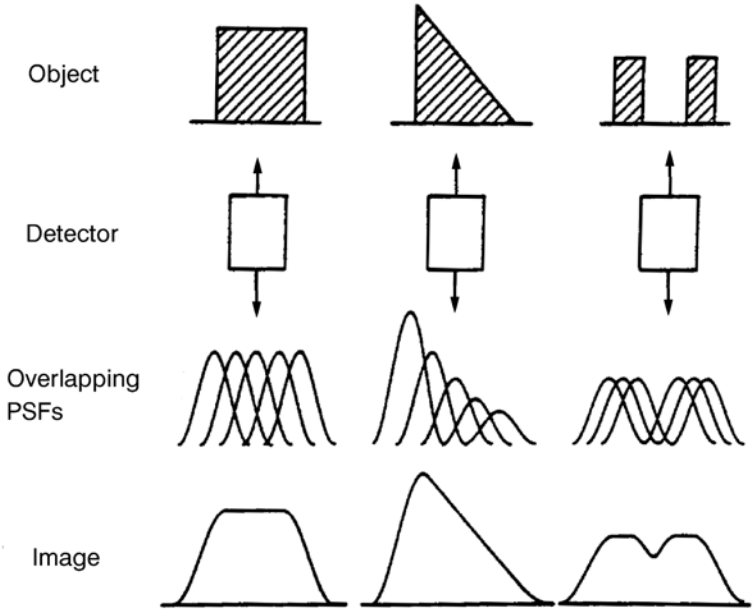

Figure 2.5: Knowledge of the PSF of the imaging system allows to calculate the image from the object or, inversely, of the object from the image.

However, the point spread function is a two-dimensional function that is, in general, difficult to measure. In some cases, the so-called *line spread function*

(LSF) [8] can more easily be measured, and the PSF is mathematically derived from it. The LSF is defined as the distribution of absorbed energy per unit area in the image plane when the imaging system is irradiated by an infinitely long, vanishingly narrow slit . The LSF is composed of overlapping point spread functions.

For a system where the PSF is rotationally symmetric, the LSF is independent of the direction. For such detectors, the line spread function gives a complete description of the system. If the imaging system is not rotationally symmetric the LSF must be measured in all directions to allow derivation of the PSF.

The usefulness of the concepts of PSF and LSF is that the analysis of how complicated structures are imaged can be reduced to investigating the reproduction of simple objects such as point and lines.

Another concept that can be useful to characterize the imaging system is the *edge spread function* (ESF), which is defined as the distribution in absorbed energy per unit area when a long, sharp edge of a totally absorbing material is imaged.The edge spread function is also composed of point spread functions.

Once the PSF has been determined, either directly or through the LSF or ESF, it is in principle possible to calculate the image of a known object independently of its complexity. The inverse operation (reconstructing the object from knowledge of its image) is normally more interesting and can be accomplished in a similar way (see fig. 2.5).

2.1.6 Modulation transfer function (MTF)

An alternative approach to investigate the performance of an imaging system is to describe the image using elementary sine waves. A sine wave is characterized by its amplitude, frequency and phase. Every continuous function can be described as a sum of overlapping sine waves with a suitable choice of amplitudes and frequencies (Fourier analysis). In order to study the ability of an imaging system to reproduce complex objects, the response of the system to simple spatial sine waves is investigated.

If the imaging system is linear and spatially invariant, the image of a sine wave remains a sine wave with the same frequency as the input wave. If the imaging system is not ideal, the amplitude of the input signal will be different. Decreasing amplitudes indicate that the information content of the image has been reduced (see fig. 2.6). Normally, high frequencies are more distorted than lower frequencies. If the imaging system is linear but not spatially invariant (for instance, due to the X-ray focus) a change in phase of the sine waves will also occur.

For each spatial frequency f (expressed in terms of lp/mm) the modulation of the signal is calculated. The modulation M for a sine wave is:

$$M = \frac{E_{max} - E_{min}}{E_{max} + E_{min}} \tag{2.3}$$

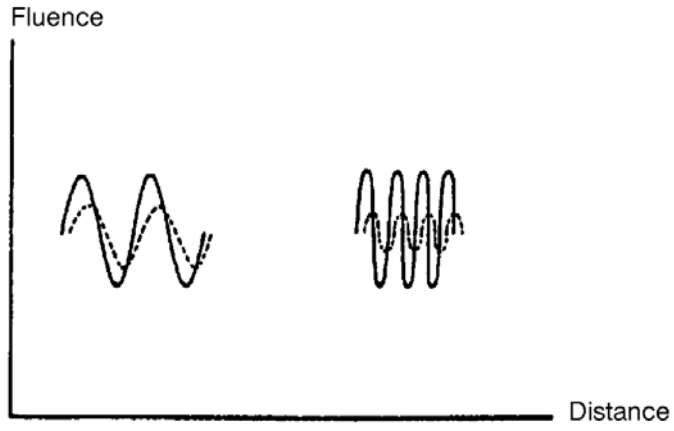

Figure 2.6: Distortion of the amplitude and phase shift of sine waves which pass through a linear, spatially variant system. Solid curve: input wave. Dashed curve: output wave.

where E_{max}, E_{min} are respectively the maximum and minimum amplitudes of the sine wave (see fig. 2.7).

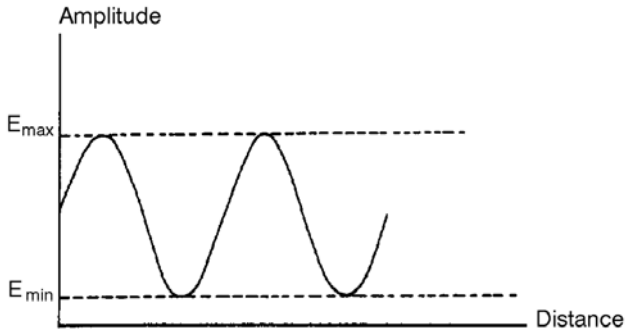

Figure 2.7: The modulation M can be calculated from E_{max} and E_{min}.

The ratio of the modulation of the output wave and the modulation of the input wave at a given spatial frequency f gives the *modulation transfer function* MTF [9] of the imaging system:

$$MTF(f) = \frac{\left(\frac{E_{max}-E_{min}}{E_{max}+E_{min}}\right)_{out}}{\left(\frac{E_{max}-E_{min}}{E_{max}+E_{min}}\right)_{in}} \tag{2.4}$$

If this formula is used to calculate MTFs at different spatial frequencies, an MTF-curve is obtained (fig. 2.8). The MTF-curve describes how the imaging system reproduces the contrast of the object at different spatial frequencies. An imaging system that does not distort the object gives an MTF-curve that is equal to 1 at all spatial frequencies. However, such an ideal imaging device does not exist.

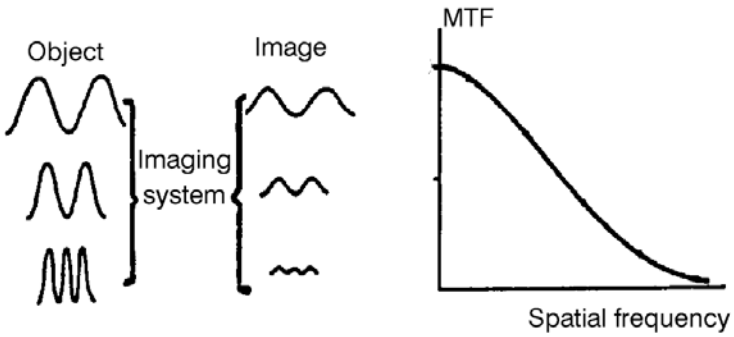

Figure 2.8: The MTF-curve describes how the imaging system reproduces the contrast of the object at different spatial frequencies.

An advantage of the concept of MTF compared to that of PSF is the following. If a system consists of different components, each with is own modulation transfer function MTF_1, MTF_2, ... , MTF_N then the total modulation transfer function of the system is obtained as the product of the individual MTFs:

$$MTF_{total} = MTF_1 \times MTF_2 \times ... \times MTF_N \tag{2.5}$$

A typical example is given in fig. 2.9.

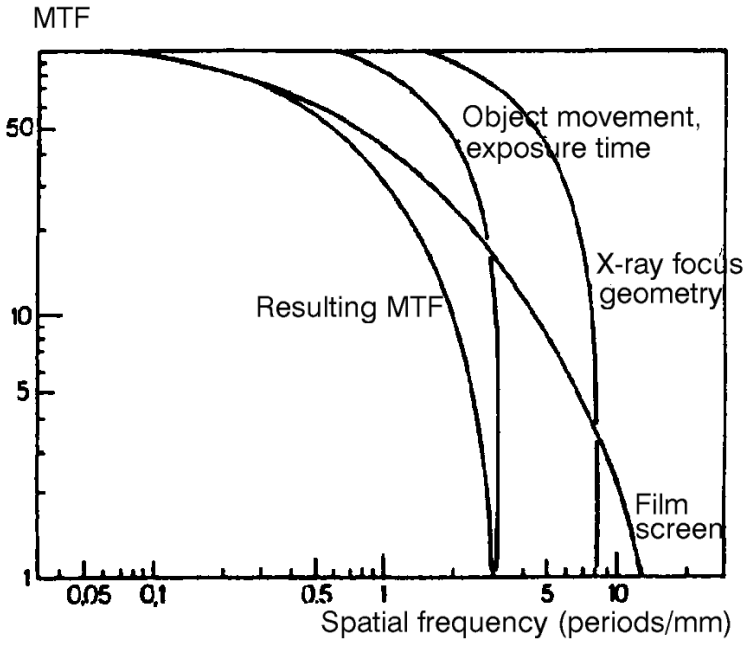

Figure 2.9: Total MTF-curve for an X-ray imaging system and MTF-curves of its components.

2.1.7 Contrast transfer function

The *contrast transfer function* (CTF) is very similar to the MTF. It concerns the modulation of a signal passing through a bar pattern (this structure is usually employed to determine the spatial resolution of imaging systems, see section 2.1.1).

The CTF is measured by exposing a number of bar patterns with known spatial frequencies ν_i, and then calculating the modulation of the resulting signal:

$$CTF(\nu) = \frac{I_{max}(\nu) - I_{min}(\nu)}{I_{max}(\nu) + I_{min}(\nu)} \tag{2.6}$$

The same method is often used to measure the MTF. This is not strictly correct as a series of line pairs corresponds to a square wave pattern and not to a sine wave pattern, but the resulting difference is often small [10].

2.1.8 Noise power spectrum and noise equivalent quanta

The *noise power spectrum* (NPS, also known as *Wiener spectrum* [11] is the squared modulus of the Fourier transformation of the fluctuations about the mean of a flat field image.

The noise found in conventional X-ray imagers is described by a noise power spectrum that is roughly constant over a wide range of spatial frequencies. Such a NPS is called *white* in analogy to white light, which contains a mixture of light of all frequencies within the visible spectrum. A white noise power spectrum indicates that the random fluctuations at one point in the image are uncorrelated with or independent from fluctuations at another point.

The *noise equivalent quanta* (NEQ) [12] is also an important parameter. It is defined in the following way:

$$NEQ(\nu) = \frac{MTF^2(\nu)}{NPS(\nu)} \tag{2.7}$$

2.2 X-ray imaging technologies

A large number of X-ray imaging detectors has been built, for use in many different fields, ranging from medical applications to material analysis to protein crystallography, and many more. A complete and detailed study of the existing X-ray detectors is thus out of the scope of this thesis. However, an overview of the general characteristics of imaging systems is provided in the following sections.

2.2.1 Analog and digital systems

Systems producing images in analog format and systems producing digital images are both used for X-ray imaging. Examples of analog systems are film based detectors, which are still the most widely used systems for medical radiology. Recently designed systems are often digital (CCDs, hybrid pixel detectors, amorphous-Si flat-panel systems, and many others).

A digital system offers many advantages with respect to an analog one:

- Digitized images are produced instantaneously (since they need no development) and easily transferred, so that they can quickly be evaluated by specialists at different locations. Films have slow chemical development procedures and cannot be easily transferred to another location or copied. Data storage and retrieval is also facilitated by the use of a digital approach.

- A digital system allows to perform image processing. The use of specific mathematical algorithms and software filters can enhance barely visible structures. In general the digitized image can be processed so that the user can obtain from it as much information as possible. Image processing is a powerful tool: offline image treatment and specially 3-dimensional image

reconstruction has become one of the most important fields in medical imaging (in *Computed Tomography*, for instance).

- Dose reduction is certainly one of the strongest arguments for digital systems. Films have a limited linear dynamic range: overexposure or underexposure will result in a serious loss of contrast. With digital systems the dose can be optimized to the required signal-to-noise ratio for a specific setup or task. This is specially important for medical applications, because it can lead to a considerable reduction of the radiation dose that a patient is receiving. In the case of the Medipix1 chip, it has been estimated that an image with a contrast comparable to traditional analog technologies can be obtained with a radiation dose several times (5-30 times) lower.

Film-based systems, however, offer excellent spacial resolution, typically of the order of 1 μm.

2.2.2 Direct and indirect X-ray detection systems

Another very important distinction between imaging systems can be made at the photon detection level. A system can be classified either as a *direct* X-ray detector or as an *indirect* detector. In a direct detection system the X-rays convert in the detector itself. An indirect system uses an intermediate layer to convert the X-rays into visible light. For this reason, in the case of an indirect conversion system the spatial resolution is deteriorated because of the lateral spread of the visible photons, which is a function of the distance between the light emission point and the sensor. Also some visible photons will be lost, thus reducing the quantum efficiency of the device. Direct photon detection is thus preferable for its performance regarding spatial resolution, contrast and DQE.

Examples of indirect detection systems are screen-films, amorphous-Si flat panel detectors and CCDs, while hybrid pixels and selenium panels are direct detectors.

2.2.3 Counting, integrating and energy-weighting systems

There are three different approaches for recording signals coming from detected photons: the counting method, the integrating method and the energy-weighting method.

In a typical counting device, the pulse height of a photon signal is compared to a threshold set in a comparator. If the signal is above this threshold, the value of a counter is incremented. Every photon with an energy above the threshold is counted. Thus, all the counted photons have the same weight. The possibility of setting a threshold leads to noise reduction, which increases the signal-to-noise ratio and the dynamic range. Current hybrid pixel detectors, like Medipix, are an example of counting devices.

An integrating detector is based upon a different principle: all incoming signals are added up, including noise. This reduces signal-to-noise ratio and dynamic range. Each detected photon contributes to the signal with a weight

factor proportional to its energy. Higher energy photons deposit more charge in the detector, which results in a an higher contribution to signal. In many cases this is a disadvantage, since high energy photons contribute less to the image contrast than low energy photons. In mammography, for instance, the higher part of the energy spectrum, after having passed through the patient, carries much less useful information than the lower energy part. Examples of integrating systems are all types of film-based systems, amorphous semiconductors arrays and CCDs.

The third option is an energy-weighting system, where the weight given to each detected photon is calculated with a certain function $w(E)$. The best weighting factor is approximately $w_{best}(E)=E^{-3}$, where E is the energy of the incident photon [13]. This reflects the attenuation properties of the objects to be imaged. The application of such a weighting function can lead to an increase of the signal-to-noise ratio of up to 2 with respect to the function $w_{int}(E)=E$ (typical of integrating systems) and of up to 1.5 with respect to $w_{count}(E)=1$ (found in counting systems).

An energy-weighting system can be obtained as an improvement of a counting device with above-threshold signal processing. For example, the signal height (which is proportional to the deposited energy) could be determined and stored in a corresponding ADC channel. In this way it could be possible to associate a weighting factor to the content of each ADC channel [17].

2.3 Conclusions

A number of different categories of X-ray detectors exist, each with specific advantages and disadvantages. In the following chapters the application of hybrid pixel technology for X-ray imaging with the Medipix1 and Medipix2 detectors will be described.

Chapter 3

Hybrid pixel detectors and the Medipix1 chip

The Medipix1 chip (also known as PCC, Photon Counting Chip) is the first photon counting chip designed by the Medipix collaboration. After an overview of hybrid pixel detectors and their most important properties, this chapter will focus on the description of the chip and on a typical experimental setup.

An excellent overview and outlook of semiconductor detectors in future high energy physics experiments is given in [18]. The following sections are concentrating instead on applications of pixel semiconductors in X-ray imaging.

3.1 Hybrid Pixel Detectors

A hybrid pixel detector generally consists of two parts: a high resistivity semiconductor sensor, segmented into a matrix of diodes, and a readout electronics chip divided into a corresponding matrix of readout cells. These two parts are connected together, both mechanically and electrically, through small spheres (about 20 μm diameter) of conducting material, usually Pb/Sn solder material or indium. This procedure is called *flip chip bonding* or *bump bonding* process (see fig. 3.1 and appendix A).

A reverse bias voltage is applied to the semiconductor sensor so that it is operated under full depletion: the diode is depleted of free charge carriers. An incoming X-ray hitting the sensor knocks out a valence electron from a silicon atom via the photoelectric effect. This photo-electron has a large kinetic energy, equal to the photon energy minus the atomic binding energy. Secondary electron-hole pairs are created by the photoelectron. The electric field due to the presence of the bias voltage drifts the electron cloud toward the anode contact and the hole cloud toward the cathode contact. Depending on the material properties of the sensor (such as carrier mobilities and collection efficiencies), either holes or electrons are collected on the readout electronics input. Holes are detected as positive going pulses on individual cathode contacts (in this case

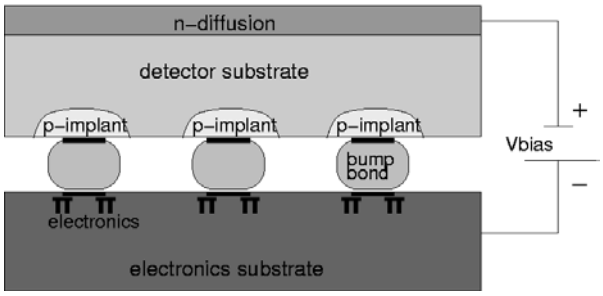

Figure 3.1: Cross section of an hybrid pixel detector, showing the sensor (top) connected to the electronics (bottom) through bump bonds. The configuration shown here is used for hole collection.

the sensor is called positive polarity sensor), while electrons are detected as negative going pulses on individual anode contacts (negative polarity sensor). Silicon sensors are usually employed as positive polarity sensors because the electron pulse is rather short, while for instance for GaAs the negative polarity sensor configuration is preferred since the charge collection efficiency of holes in GaAs is quite bad.

The semiconductor sensor must be capable of stopping the incoming radiation. Silicon sensors of 300 μm thickness [1] show excellent performance for incoming X-ray energies between 5 and 10 keV, thus for both Medipix1 and Medipix2 detectors 300 μm thick silicon sensors have been chosen. However, when using higher energy X-rays, higher-Z materials like GaAs or Cd(Zn)Te are needed because of their much higher stopping power. This is because, as shown in section 1.1.1, the photoelectric cross section goes as Z^5 (300 μm thick silicon sensors will stop only 25% of incoming 20 keV X-rays). These higher energies are needed especially for biomedical imaging, while diffraction and crystallography usually need the lower X-ray energies. For this reason, 200 μm thick GaAs sensors have been employed in Medipix1 detectors, while for Medipix2 sensors both GaAs and CdTe are used. Details of a silicon sensor are shown in fig.3.3.

As an alternative, silicon can be employed for higher energy X-ray detection, if sensor thickness is sufficient to provide adequate stopping power. Silicon sensors of 525 and 700 μm thickness are used for the Medipix2 detectors, while such solution was not implemented in the case of Medipix1 assemblies. However, this approach is not as efficient as the use of high-Z materials. Table 3.1 lists

[1] The value of 300 μm for the thickness of a silicon sensor originates from the requirements of a tracking detector for high energy physics. In that environment, the semiconductor sensor must be thick enough so that each charged particle can deposit a sufficient amount of charge in order to be detected with good S/N ratio. At the same time, the sensor must be not too thick, because large amounts of material decrease track resolution due to multiple scattering. In the case of silicon, the value of 300 μm is a good compromise. For design and production reasons, it has been kept also in the case of Medipix detectors. While other semiconductor sensors (different thickness and/or material) are also employed, 300 μm silicon is still the most common type of sensor connected to Medipix chips.

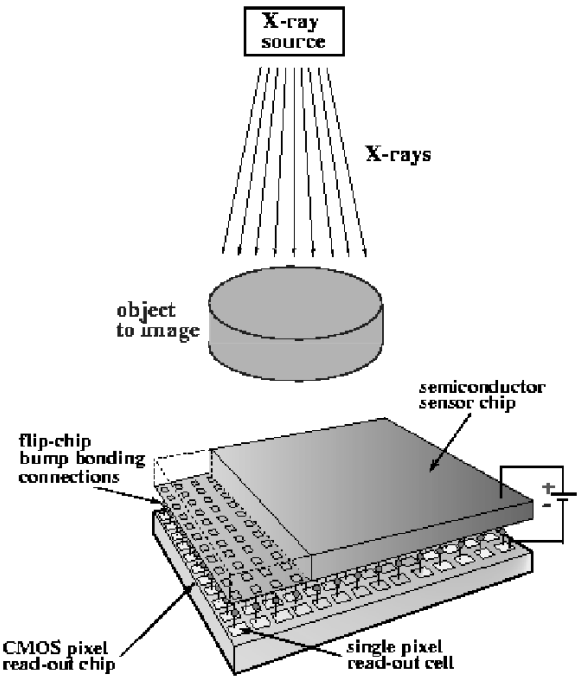

Figure 3.2: A hybrid pixel detector is made up of two matching parts: a matrix of readout electronics cells bump-bonded to a matrix of sensor diodes. X-rays coming from an X-ray source are partially absorbed or scattered by the object, converted by the semiconductor sensor and counted by the readout electronics.

the stopping power of different materials for X-rays of different energies.

3.1.1 Advantages and disadvantages of hybrid pixel detector technology

The use of hybrid pixel detectors for X-ray imaging offers many advantages over other systems (see Chapter 2 for general remarks on imaging systems):

- One of the advantages is that a hybrid pixel detector is a digital system. Because of that it has many interesting properties that are not found in older, analog imaging systems:
  - Digitized images are produced instantaneously and easily transferred. Films have instead slow development procedures and cannot be so easily transferred. Data storage and retrieval is also much facilitated by the use of the digital approach.

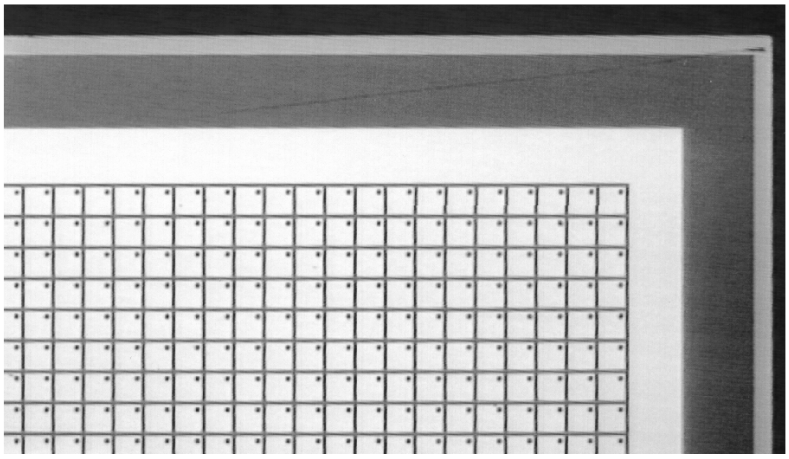

Figure 3.3: Part of a Medipix1 silicon sensor consisting of a matrix of 64×64 diodes of size 170 μm × 170 μm, matching exactly the matrix of readout cells. The thickness of this detector is 300 μm. On every pixel, the metalized bump pad is visible as a black dot of 25 μm diameter.

  - A digital system allows to perform image processing. The use of specific mathematical algorithms and software filters can enhance barely visible structures, and in general the digitized image can be treated so that the user can obtain from it as much information as possible.
  - Films have a very limited linear dynamic range. With digital systems the radiation dose can be optimized to the required signal-to-noise ratio for a specific setup or task. This allows in general a dose reduction.

- Another advantage of an hybrid pixel detector is that it is a *direct* X-ray detection system, while most of the traditional imaging systems (specially the ones used for medical applications) use *indirect* detection. Direct photon detection offers better performances for spatial resolution and contrast.

- A hybrid pixel detector can be a counting device. Many widely used systems follow instead the integrating approach (films, for instance, or CCDs). A counting detector offers many advantages:

  - Noise suppression due to the already mentioned threshold mechanism. This allows to achieve an higher SNR, thus an improved image quality. Furthermore, long data acquisition periods for *low dose rate imaging* become possible, which is relevant for many applications (for instance, autoradiography).

	Si	Si (600 μm)	GaAs	CdTe
5 keV	100%	100%	100%	100%
10 keV	90.64%	99.12%	99.89%	100%
20 keV	26.8%	46.42%	99.88%	98.15%
30 keV	9.55%	18.19%	64.72%	98.27%
40 keV	4.78%	9.33%	63.11%	97.24%
60 keV	2.09%	4.14%	27.77%	70.37%
80 keV	1.58%	3.14%	14.67%	42.97%

Table 3.1: Calculated fractions of X-rays from monochromatic beams of different energies that are converted to photoelectrons by a 300 μm thick layer of different semiconductor materials (Si, CdTe, GaAs). In the case of silicon, the stopping power of a 600 μm thick layer is also shown.

  - Linear and theoretically unlimited dynamic range. Film systems suffer from a restricted linear range. CCDs have a much extended linearity (but they present the drawback, as already mentioned, that high energy photons are weighted more than low energy ones). The dynamic range for counting systems is theoretically unlimited, the actual limitation being only of a practical nature (limitations in the space needed to implement the transistors for the counters in a certain area of the pixel cell).
  - A very precise threshold setting allows to cut off Compton scattered events [14]. This is important for monoenergetic X-ray sources. Scattering in the imaged object can a serious problem for many applications, and it leads to image blurring. As an example, in mammographic applications ratios of scattered to primary radiation can attain 80% after passage through 6 cm of breast tissue [15]. Scattered radiation is one of the reasons why small details and low contrast objects are often undetectable. Usually this problem is addressed with anti-scatter grids, airgaps or scanning slits, but that results in a dose increase (for mammographic applications, the increase can be as much as a factor of 2 [16]).

- Another useful property of hybrid pixel devices is that for a given design of the readout chip, several different semiconductor sensors can be employed, depending on the particular application. Gas gain grid have also been used instead of the sensor, with success (see Chapter 7. This greatly enhances the flexibility of the detector.

- Fully 100% filling factor of semiconductor sensor, which is not always the case for CCDs or active pixel sensors.

- Hybrid pixel detectors use mainstream CMOS IC technology, so they benefit from its advantages: reliable yield, quick turn-around, low power con-

sumption, good price/performance ratio and steadily improving technology

However, hybrid pixel technology also has some drawbacks. The main disadvantage associated with this type of detectors is that the maximum sensitive area is usually quite small, typically of the size of 1-2 cm^2, due to fabrication processes of CMOS chips. This problem is further investigated in chapter 6, where a possible solution (the tiling of several chip into an array of hybrid pixel detectors) is also described.

3.2 The Medipix1 X-ray Detector

The Medipix1 ASIC (Application Specific Integrated Circuit) has been designed by the CERN MIC group and realized in 1 μm SACMOS (Self-Aligned Contact CMOS) design technology. The component density is comparable to a 0.6 μm standard CMOS process. This was the highest density available at the time of the design (1997). The chip is organized as a matrix of 64 $\times$ 64 cells, its total area is 1.7 cm^2 with a sensitive area of 1.18 cm^2. The dimensions of the pixel cell are 170 μm $\times$ 170 μm (see fig.3.4) [19].

The 64 columns of the chip are connected in groups of four and multiplexed onto the 16-bit input/output bus, and this same bus is also used to load the 5 $\times$ 64 $\times$ 64-bit configuration register. Both loading and data readout can be performed at a frequency of 10 MHz and one complete frame is readout in 384 μs. Pixels cells in an added 65^{th} row at the bottom of the matrix sense the detector leakage current. The sensed current is then reproduced with opposite sign in each of the 64 pixels of the corresponding column to compensate for the detector dark current. This leakage current compensation has a practical range of 0 to 10 nA per pixel.

The Medipix1 X-ray detector is made of a Medipix1 chip bump-bonded to a semiconductor sensor. This structure (chip bonded to sensor) is usually referenced as *detector assembly* or simply *assembly*. Two different types of sensors are used: 300 μm thick silicon sensors and 200 μm thick GaAs. In both cases the sensor segmentation into diodes has to match the chip segmentation, so these sensors are segmented into 64 $\times$ 64 pixels of 170 μm $\times$ 170 μm. The NIKHEF Medipix group has been involved mainly in studying low-energy applications of the Medipix1 detector. As a consequence of this, silicon assemblies were preferably used.

A summary of the characteristics of the Medipix1 detector (as measured on a Medipix1/300μm thick Si sensor assembly) is given in table 3.2.

3.2.1 The Medipix1 pixel cell

Each cell comprises an input bonding pad which is connected to a sensor diode via bump bonding, a preamplifier, a latched comparator with a variable threshold, a short delay line which feeds back to the comparator to produce a pulse

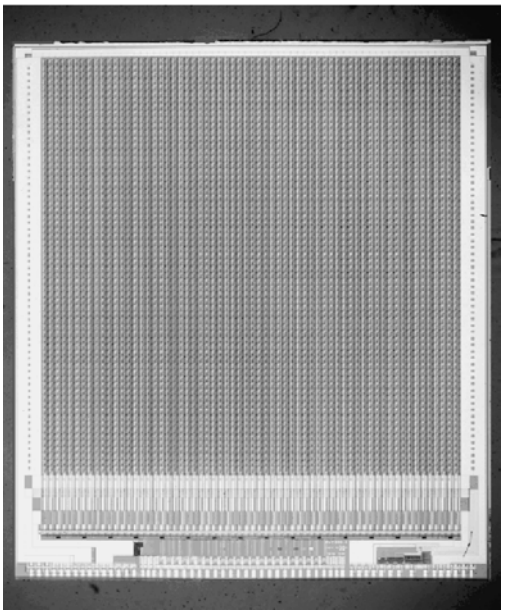

Figure 3.4: The Medipix1 Photon Counting Chip is organized as an array of 64 × 64 identical pixel cells.

Pixel size	170 μm × 170 μm
Number of pixels	64 × 64
Sensitive area	10.88 mm × 10.88 mm
Max. counting rate (pixel)	2 MHz/pixel
Max. counting rate (area)	70 MHz/mm^2
Min. threshold	1400 electrons
Threshold spread (not adjusted)	350 electrons
Threshold spread (adjusted)	80 electrons
Maximum input signal	80000 electrons
Mean total noise level (without sensor)	130 electrons
Mean total noise level (with sensor)	140 electrons

Table 3.2: Summary of the characteristics of the Medipix1 detector, as measured on a Medipix1/300μm Si sensor assembly.

and a 15-bit pseudo random counter. Individual cell configuration is performed with a register of 5 bits per cell: 3 bits for fine threshold adjustment, 1 bit to mask/unmask the cell and 1 bit to enable/disable a test input. The threshold adjustment circuitry is needed in order to compensate for non-uniformities among pixels. The non-uniformity is due to mismatching between the properties of the transistors in the pixels. A good uniformity can be achieved by designing large transistors, but this implies a rise in the power consumption as well as pixel area. A better approach is to design smaller transistors. The resulting differences in the matching of their properties can be adjusted with a fine-tuning circuitry in each pixel. This latter approach is much more optimal in terms of power consumption and area occupied, and it has been chosen in the case of the Medipix1 and Medipix2 chips.

A signal called *shutter* allows for switching between the counting and the readout modes. A block diagram of a pixel cell is represented in fig.3.5; the main components of the cell are described below:

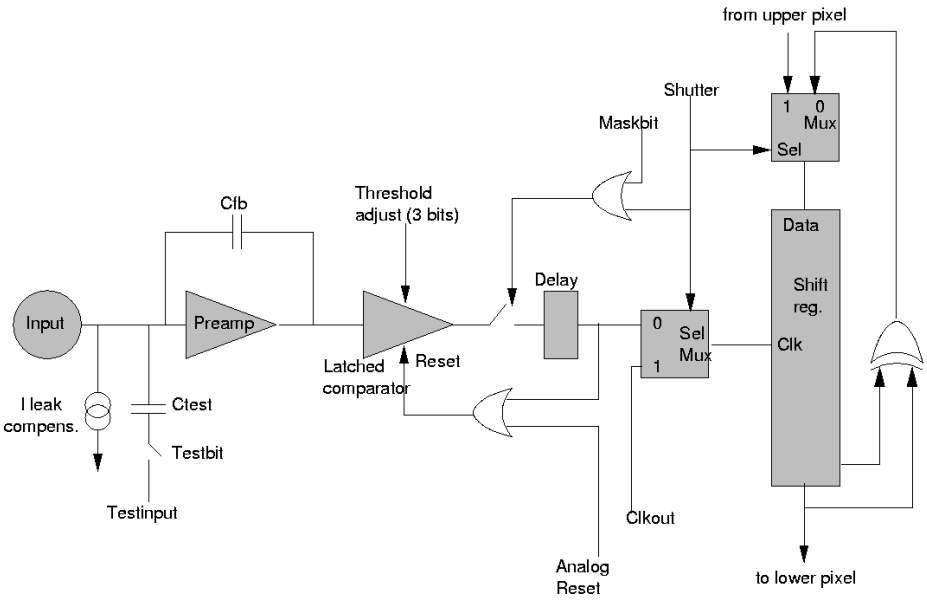

Figure 3.5: Block diagram of a Medipix1 pixel cell. The main steps are: input - charge sensitive preamplifier - common and individual adjustable comparator - delay - 15 bit pseudo-random counter when shutter active, acting also as a shift register during readout.

- The charge released by an X-Ray detected in a pixel of the semiconductor sensor drifts in the applied electric field. The signal is transferred through the solder bumps to the input amplifier in the corresponding pixel cell. In

the Medipix1 chip, only positive signals are accepted, meaning that the sensor should collect holes. The preamplifier is charge integrating and it has a gain of 125 mV/fC. Its input can either be a signal coming from the sensor diode or a test input provided externally.

- The comparator is asynchronous and has an externally set threshold. In addition to a threshold common to all the 4096 pixels, each individual threshold can be separately fine tuned with the 3-bit resolution mentioned above. Only if the pulse height exceeds the threshold level the signal will be further processed. The width of the digital pulse going out from the comparator is defined through an externally adjustable delay and the comparator is reset.

- A shift register is used to count the detected photons. The acquisition time is set by an external shutter signal. When the shutter is active the 15 bit pseudo-random counter will count each signal that has exceeded the comparator threshold. The pseudo-random counter is a finite state machine with $2^{15} - 1$ distinctive states. Each clock pulse causes a change of state. The number of counts in each cell is derived by comparing the pseudo-random number with the contents of a look-up table. The counter is static and is connected during the readout phase as a shift register to the upper and lower neighbouring pixels of the same column enabling a serial readout of the column. This concept makes the information storage part of the readout which saves valuable space (since a pseudo-random counter is smaller in area than a binary counter), and also can be easily read out in serial mode, without extra circuitry.

3.3 The Medipix1 readout system

In a typical Medipix1 setup, the assembly is mounted on a standard printed circuit board (see fig. 3.6). Wirebonds are used to connect the CMOS chip to gold-plated pads on the chipboard. The circuit board is provided with a Lemo connector for semiconductor sensor bias supply (provided externally) and a connector to the Muros1 interface [20].

Muros1 (Medipix1 re-Usable Read-Out System) is a board, developed in the NIKHEF-Medipix group, interfacing the Medipix1 chip to a PC fitted with two commercial National Instruments cards (to which Muros1 is directly connected). Its main function is to translate the TTL levels of the two NI cards to the CMOS levels required by the Medipix1 chip, but it also includes a test-pulse generating circuit and provides the analog bias values and threshold settings.

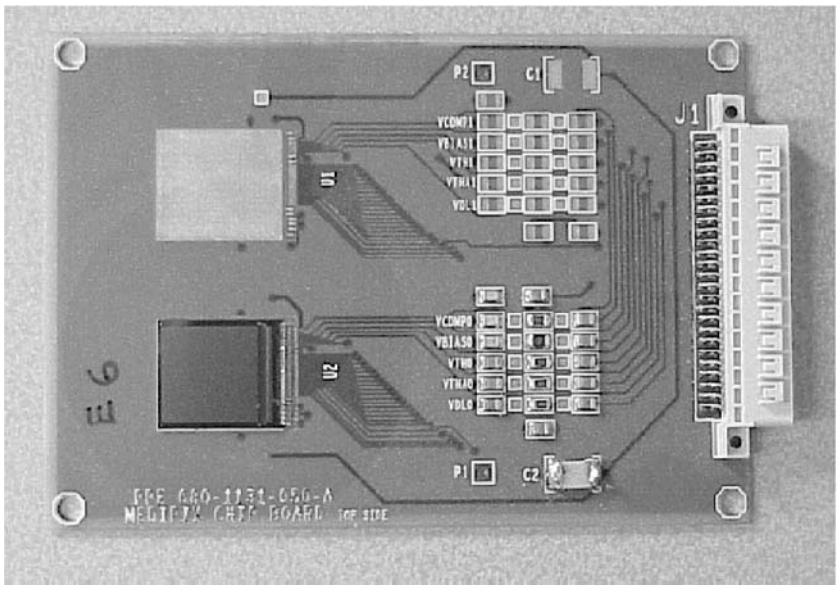

Figure 3.6: Medipix1 chips and assemblies are mounted on a standard printed circuit board (PCB).

Figure 3.7: The Muros1 board interfaces a Medipix1 chip to a PC.

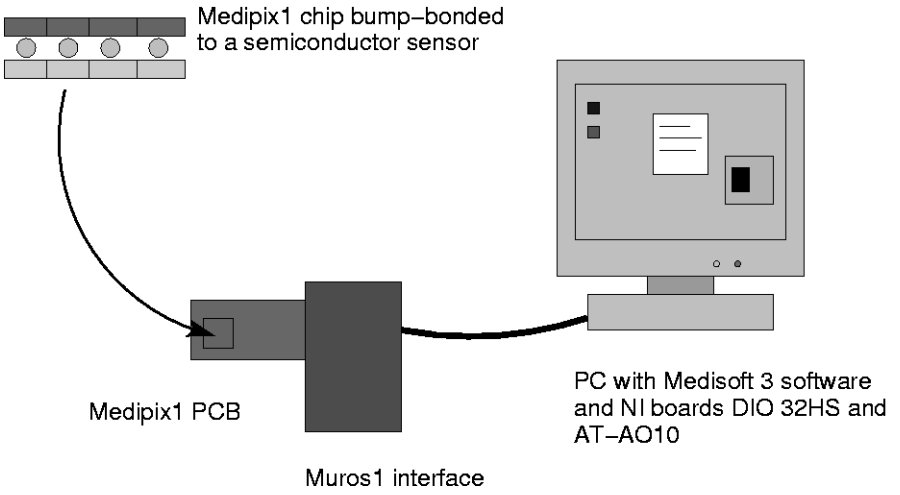

Figure 3.8: Common Medipix1 setup. The Medipix1 chip is bump-bonded to a semiconductor sensor and mounted on a Medipix1 chipboard. The chipboard is connected to a standard Windows PC via a Muros1 interface. The PC is equipped with Medisoft3 software and two commercial National Instruments cards.

The NI commercial cards employed in this readout system are the AT-AO 10 model for the analog voltage supplies and the PCI-DIO 32HS model (or equivalent) for the bi-directional digital data bus and the clock. The AT-AO 10 card has ten analog output lines but only seven are used: two for generating the test pulse and five for the analog voltages (bias, common threshold, individual threshold, etc.). It also provides 8 digital I/O lines of which five are used for control purposes (shutter, read/write, reset, data/control, chip select). This card also provides power supply to Medipix1 chip and Muros1. The PCI-DIO 32HS card has 32 digital I/O lines among which 16 are used for data communication. The card communicates with the Medipix1 chip at a maximum speed of 40 Mbytes/s.

The user controls the system through a standard PC. A software package (*Medisoft3*), developed by the University of Napoli in the LabWindows CVI environment, is required. This software is a package written in ANSI C under LabWindows/CVI development environment and provides the user with a suitable interface for data acquisition operations. Several other routines are included in this package: routines for image manipulation and display, threshold equalization (to improve detector uniformity) and threshold scans. A representation of a common Medipix1 setup is given in fig. 3.8.

There are also other ways to control and read out a Medipix1 chip, and other setups (different from the one described above) have been studied. For instance, before Muros1 was realized, the readout system most commonly employed was

the *MRS* (Medipix Readout System), based on the VME system and designed by the Laben company (Italy). All in all, four such systems were built, before they were replaced by the much cheaper Muros1 solution. More recently, the Napoli group realized the *portable Muros1* board or *pMuros1* [21], based on the Muros1 design, and aimed at autoradiography applications.

3.4 Medipix1 production and quality control

Once the chip design phase is finished, the layout files of the Medipix1 chip are sent to a manufacturing company. The processing steps are performed on 150 mm diameter silicon wafers (see fig. 3.9) in a SACMOS process with 1 μm feature size. A total of 64 chips is realized on each wafer, but only a certain fraction of these will work correctly. This is due mainly to production defect and impurities present in the silicon, which limit the yield of working chips. In order not to waste money and sensors in bump-bonding non-working chips, all the working ones have to be selected before sending the wafer to the dicing and bonding site. Only *known good die* (KGD) are bumped onto sensor chips.

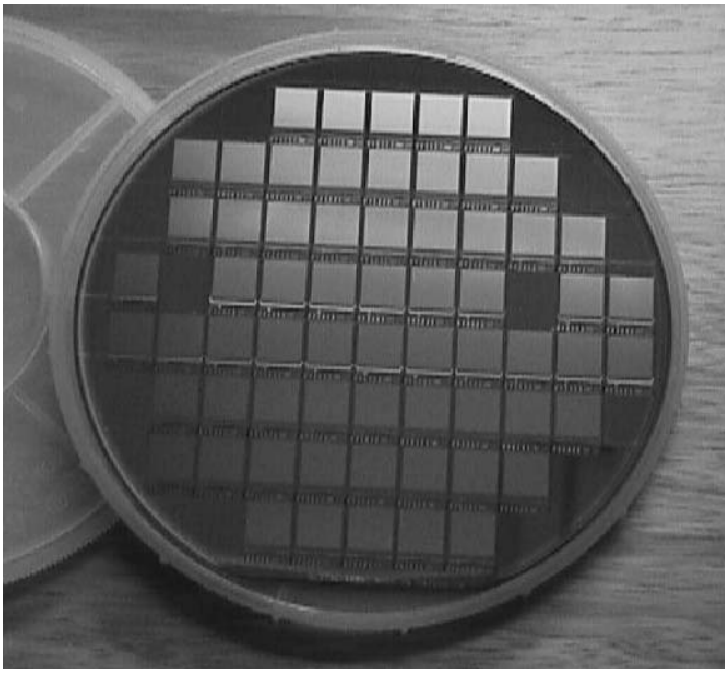

Figure 3.9: A Medipix1 wafer (150 mm diameter) contains 64 chips. The two empty places are used by the manufacturer to put test structures to monitor the production process parameters.

A specially designed probe card was employed during Medipix1 wafer probing. Connected to the Muros1 board and provided with 58 tiny needles, it allows to contact the test pads on the chip under investigation, thus making possible the readout of the Medipix1 chips while still on the wafer.

The probe card is mounted in a wafer probing machine while the Medipix1 wafer under test is fixed (through vacuum suction) on a moving chuck situated below the card position. Contact is made between the probing needles and the testing pads on the chip. In this way the chip can be tested via a standard PC connected to the probe card through a Muros1 interface. When all the necessary tests have been performed, the probe station can automatically step to the next chip.

At the end of a wafer probing test, a *wafer map* summarizing the most important information obtained about the chips is realized. This map will be used during the next operations that will be made on the wafer (chip selection, bump-bonding, chip usage). An example of a Medipix1 wafer map is given in fig. 3.10.

3.4.1 Medipix1 wafer testing procedure

The testing procedure of a Medipix1 chip can be divided in two parts.

The first part consists of evaluating the digital behaviour of the chip. An image pattern is written to the pixel matrix, and it is then read back, and the two patterns are then compared. Another test to be performed is to check the correct behaviour of the threshold adjustment bits and of the counters. Since during readout the counter acts as a shift register for the corresponding column, any error anywhere in the counters results mostly in the loss of the entire column. The presence of these so called *dead columns* is one of the most common flaws found in Medipix1 chips.

The second part concerns the analog characterization of the chip. Two test are of particular interest: the *threshold map* determination and the *ANIN test*. A test-input capacitor can be connected to the analog input line through a flip-flop controlled switch, and in this way we can produce an analog input signal using an external pulse generator which gives a train of pulses of fixed amplitude (this pulser is mounted on the Muros1 interface).

The *threshold map* determination is a study of the distribution of the pixel threshold levels in the entire pixel matrix. Several trains of pulses of different height are sent to the chip. For each pixel, its threshold is defined as the pulse height where the pixel counts 50% of the incoming pulses.

During the ANIN test, once a proper threshold has been chosen for all the pixels, a fixed number of pulses (usually 1000) is sent to the entire pixel matrix. Uniformity in response is then studied (a perfectly working chip would count exactly 1000 in every pixel cell).

Depending on the outcome of these tests, the chips were classified as not working, bad (*class C*), good (*class B*) or very good (*class A*). Classification was

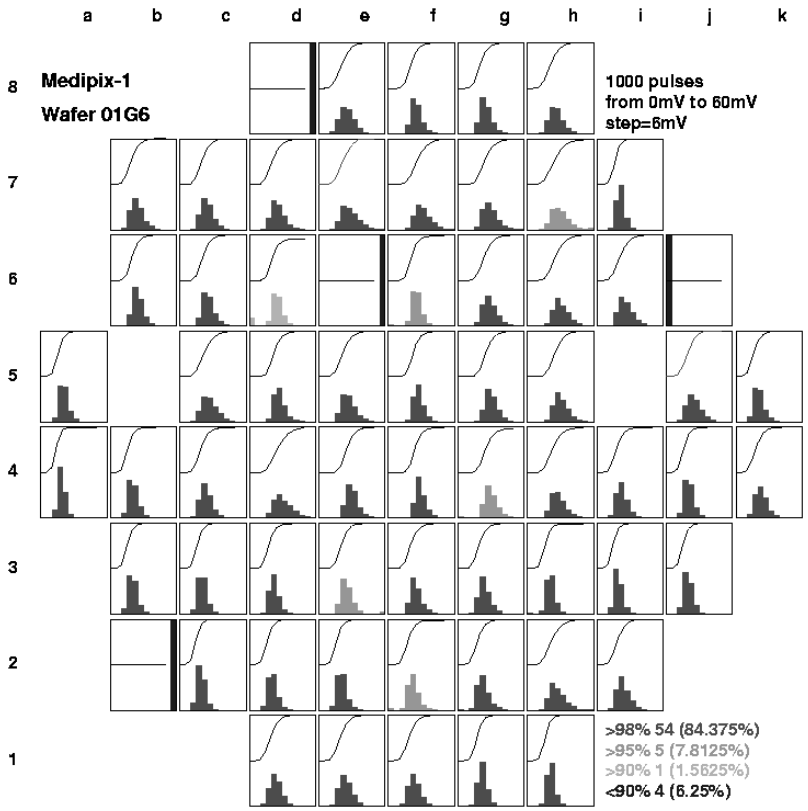

Figure 3.10: A Medipix1 wafermap. On this particular wafer named 01G6, the probing tests found 54 class A chips, 5 class B chips, 1 class C chip and 4 non working chips, for an overall yield of about 94%. This is a very good wafer. The average yield fluctuates from batch to batch but it is usually higher than 60%. Threshold distributions are also shown on the wafermap.

based upon threshold distribution (the lower the pixel thresholds, the better) and number of working pixels per chip (see fig. 3.10 and table 3.3).

Number of working pixels	Chip classification
$> 98\%$	Class A
$> 95\%$	Class B
$> 90\%$	Class C
$< 90\%$	Not usable

Table 3.3: Medipix1 classification system, based on the number of working pixels.

3.5 Medipix1 Image Gallery

The Medipix1 system has been tested and evaluated under many different conditions, and it has been proved to be a successful single photon counting detector. In particular silicon assemblies are capable to work at room temperature even for X-ray energies as low as 5.5 keV [22].

Figures 3.11-3.14 are a few examples of images taken with the Medipix1 chip, using different types of semiconductor sensors (Si or GaAs) and X-ray sources.

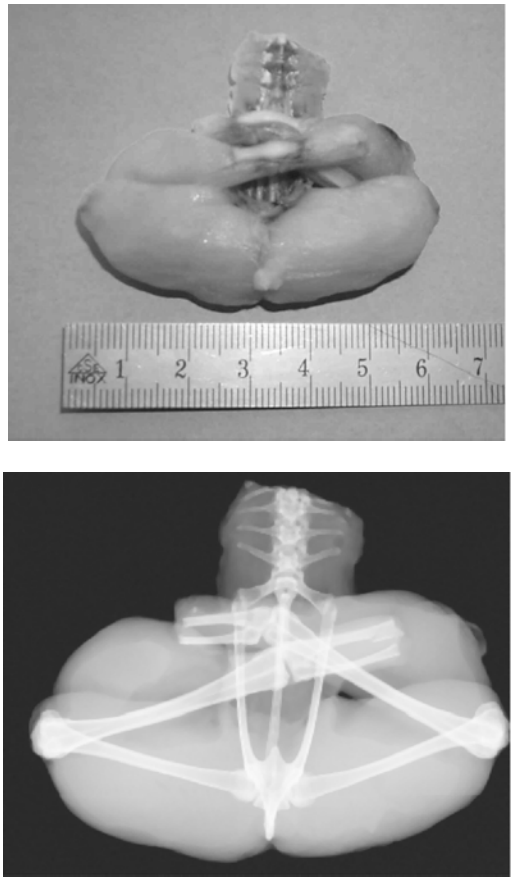

Figure 3.11: X-ray image of frog legs. This image was taken using a Mo X-ray tube. The Medipix1 detector (300 μm thick silicon sensor) was stepped for one detector width in x and half a detector width in y. Acquisition time per step was 500 ms [23].

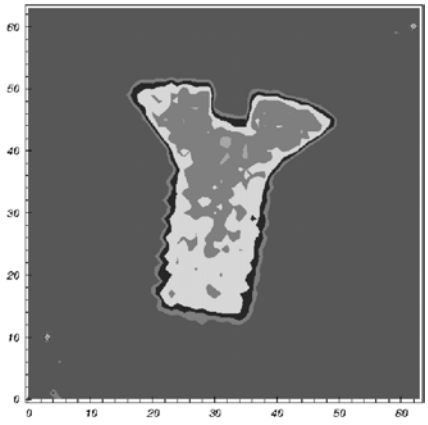

Figure 3.13: M2-screw (6 mm long) imaged with a ^{241}Am radioactive source (60 keV X-rays) using a 200 μm thick GaAs sensor (background subtracted) [24].

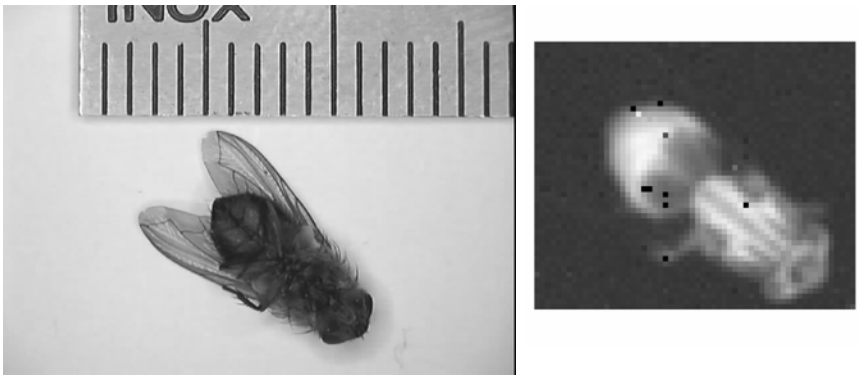

Figure 3.12: X-ray image of a fly. This image was taken using a ^{55}Fe radioactive source (5.9 keV X-rays) and a Medipix1 chip bump bonded to a 300 μm silicon detector. To reach such low energies the threshold adjustment facility of Medipix1 was used. The acquisition time chosen for this image was 5 hours (source of 4.6 MBq placed away from the fly for uniform illumination), which demonstrates the stability of the system [25].

Figure 3.14: One of the first Medipix1 raw images using a ^{90}Sr source (electrons). The different colours represent different numbers of counts per pixel. The image is formed by a 500 μm thick tungsten wire bent to an m *character. A chip bonded to a 200 μm thick GaAs sensor was used. This image has subsequently been adopted as official logo by the Medipix collaboration [24].*

3.6 Conclusions

Hybrid pixel detectors for X-ray imaging have been introduced. The focus is on the Medipix1 chip: its design characteristics are presented together with a description of the readout system and a typical experimental setup. Chip testing at wafer level, carried out at NIKHEF, is also described.

The advantages of hybrid pixel detectors over other imaging systems are outlined: excellent dynamic range and signal-to-noise ratio, good detection efficiency, flexibility (as the semiconductor sensor can be appropriately chosen).

However, this technology presents also some drawbacks, the most serious of which is a small sensitive area, limited to a few cm^2.

A detailed characterization of the Medipix1 detector, carried out at the European Synchrotron Radiation Facility in Grenoble (France), is the subject of next chapter.

Chapter 4

Medipix1 characterization with a synchrotron X-ray source

The Medipix1 system has undergone several evaluations demonstrating its imaging capabilities using conventional X-ray and radioactive sources [26, 27, 28]. In order to extend the circuit evaluation toward the high-flux regime and thus to demonstrate its potential for a wider range of applications, a characterization using an intense synchrotron X-ray source was carried out [29] at the European Synchrotron Radiation Facility in Grenoble, France (ESRF).

At the ESRF facility (fig. 4.1) it is possible to reach count rates of more than 1 MHz/pixel corresponding to flux rates of more than 3.4×10^7 monochromatic photons/mm^2/s, which cannot be obtained with any conventional X-Ray source. In the following paragraphs, results of this characterization will be reported. In particular energy response, linearity, charge sharing effects, noise properties and time resolution capabilities will be discussed.

Unless specified otherwise, a 13 keV beam has been used and individual threshold adjustment has been applied to each pixel.

This beam energy has been chosen because it is close to energies commonly used at ESRF for soft matter analysis by X-ray diffraction or X-ray scattering. In addition to that, this energy lies within the range where 300 μm thick silicon sensors are sufficiently absorbing (60% absorption efficiency). Hence, 40% of the photons pass undetected and may be absorbed by the readout electronics circuit.

Figure 4.1: A view of the European Synchrotron Radiation Facility in Grenoble.

4.1 ESRF: the European Synchrotron Radiation Facility

The ESRF is a joint facility supported and shared by 17 European nations. The ESRF project started in 1988, but only in 1994 the synchrotron was completed and open to users with 15 operational beamlines, which were subsequently increased to 40 in 1998.

The synchrotron light is produced in the following way. Electrons emitted by an electron gun are first accelerated in a linear accelerator (linac) and then transmitted to a circular accelerator (booster synchrotron), where they reach an energy of 6 GeV. These high-energy electrons are then injected into a large storage ring (844 m in circumference) where they circulate in a vacuum environment, at a constant energy, for several hours.

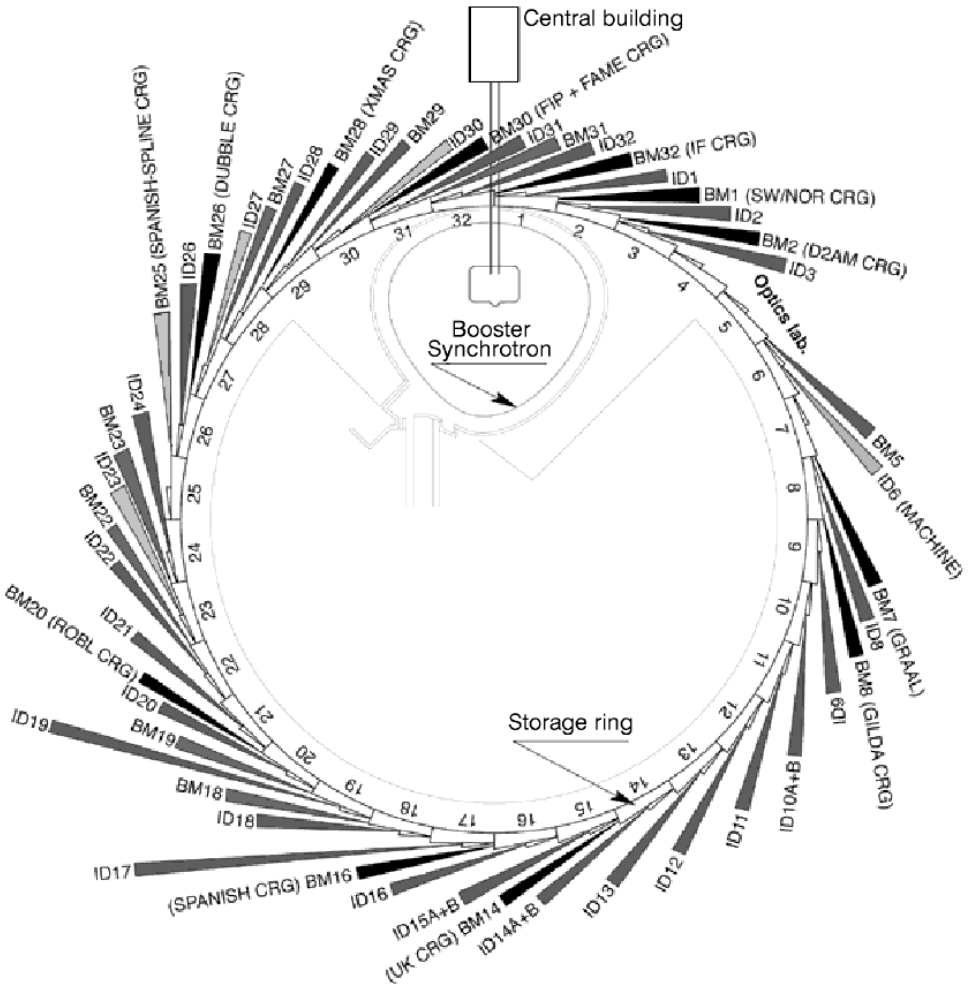

Figure 4.2: A schematic view of the ESRF structure, showing the electron gun, the booster synchrotron, the storage ring and the 40 operational beamlines.

The storage ring includes both straight and curved sections. As the beam travels through the ring, the electrons pass through different types of magnets:

- *Bending magnets*, which deflect the electrons from their straight path by several degrees, causing wide-spectrum synchrotron radiation emission
- *Wigglers* and *undulators*, that force the electrons to follow an undulating trajectory, resulting in a much more intense beam of synchroton light being emitted
- *Focusing magnets*, placed in the straight sections of the storage ring, that

Energy (GeV)	6.03
Maximum current (mA)	200
Horizontal emittance (nm)	4
Vertical emittance (nm)	0.025
Revolution frequency (kHz)	355
Number of bunches	1 to 992
Time between bunches (ns)	2816 to 2.82

Table 4.1: Properties of the ESRF electron beam.

keep the electron beam small and well defined.

The photon beams emitted by the electrons are directed toward the *beamlines* which surround the storage rings in the experimental hall (see fig. 4.2). Each beamline is designed for use with a specific technique or for a specific type of research, and is 24 hours per day operational. Each beamline includes:

- An optical cabin, housing the optical systems, used to tune the X-ray beam to have the desired experimental characteristics.
- An experimental cabin which contains the support mechanism and sample environment for the sample to be studied. One or more detectors record the information produced as a result of the interaction between the photon beam and the sample.
- A control cabin which allows the researchers to control their experiments and to collect the data.

Table 1.1 summarizes the properties of the ESRF electron beam.

4.2 The experimental setup

For this characterization at ESRF an assembly with a silicon sensor has been used. The detector was installed in the multipurpose station of the BM5 ESRF beam line, which can deliver a monochromatic beam in the 4-30 keV range with an intensity of 10^9 X-ray photons/s. The beam cross-section is controlled by two sets of double collimators, and can be made as small as 10 μm $\times$ 10 μm, while beam intensity is monitored with a large-area silicon photodiode of 300 μm thickness. The detector mounting stage allows submicron positioning in both horizontal and vertical directions as well as axial rotations with respect to the beam. A schematic representation of the test setup is given in fig. 4.3.

4.3 Spatial uniformity

To perform a spatial uniformity test a large beam spot size is needed, and the largest beam size obtainable was $6 \times 3\ mm^2$ (the detector sensitive area is about

$11 \times 11\ mm^2$). The intensity of this wide beam was not precisely uniform, but increasing from top to bottom.

The detector uniformity, with and without individual pixel threshold equalization, has been studied. In both cases, exposure time has been 10 s (with 13 keV). The result shown in fig 4.4a was obtained without any individual pixel threshold adjustment, with only the threshold voltage common to all pixels. The rectangular collimator is clearly visible but the uniformity is poor, with a lot of counting pixels outside the exposed area. These pixel-by-pixel in-homogeneities are caused by differences in the transistor characteristics for different pixels. Matching between transistors is never perfect and results in amplifier gain variations between different pixels.

To compensate for this effect every pixel includes a 3-bits DAC (Digital to Analog Converter) to tune individual thresholds. Threshold equalization routines are included in the chip control software allowing the user to calculate the optimal threshold mask and apply it to the pixel matrix. The image acquisition has been repeated after threshold adjustment and the result obtained is shown in fig.4.4c .

4.4 Linearity

Pixel response has been studied as a function of the input rate. In particular, a linear dependence is expected. Different beam intensities have been created with aluminum attenuator foils and measured with the silicon photodiode. The exposure time has been set to 30 ms, corresponding to a full counting range (15 bit) at 1 MHz average count rate. The Medipix1 detector has been operated with individual threshold adjustment.

Linearity response of a few pixels is shown in fig 4.5a (rescaled in equivalent counts per second). All the pixels have a reduced slope above 400 kHz count rate. This deviation from a linear behavior can be explained by taking into account the time structure of the beam, as well as the pile-up of detected events, and

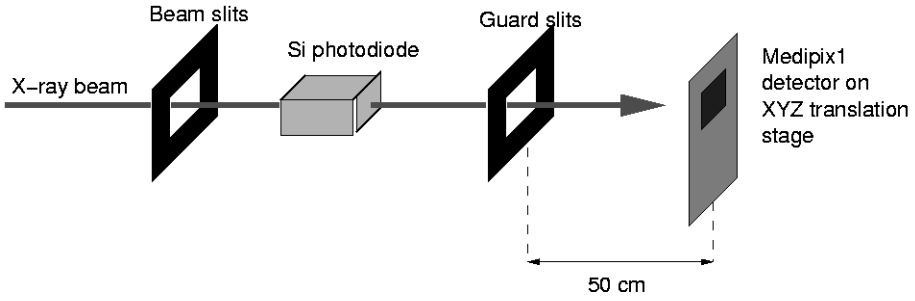

Figure 4.3: Experimental setup of the Medipix1 beam test at ESRF

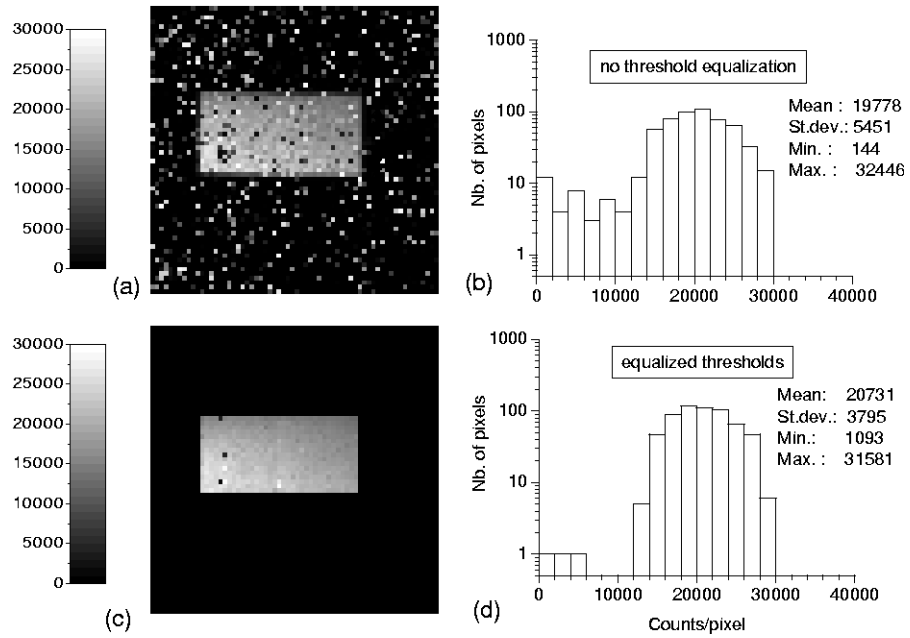

Figure 4.4: Image of a large rectangular X-ray beam and histogram of the pixel counts in the exposed region of 35 × 17 = 595 pixels. Image a) has been taken without any individual pixel threshold equalization, while for image c) such an equalization procedure has been used. Note that very few pixels fail. Non-working pixels are either non-counting (black) or noisy (white). Images b) and d) give the count distribution before and after equalization (note the logarithmic scale).

can be reproduced by a proper model.

During the Medipix1 tests the ESRF beam was operated in the $2 \times \frac{1}{3}$ filling mode. This consists of an active period of duration $T_{act} = 0.93$ μs, evenly filled with about 330 electron packets of typically 40-100 ps duration, and followed by an empty interval of 0.47 μs. This sequence is repeated twice during the ring period $T_{ring} = 2.8$ μs. In our model we assume that the detector cannot discriminate separate events within an active period, so any number of detected events is seen as one single event. It is also assumed that the effective detector recovery time in the absence of incoming hits is shorter than the inactive ring period of 0.47 μs. Finally, it is assumed that X-ray emission during each active period follows Poisson statistics. With all these hypotheses, it is possible to use the models described in [30, 31].

The Monte Carlo model prediction is in good agreement with the experimental data as shown in fig. 4.5b. This agreement confirms our hypotheses, in particular that in practice the detector cannot discriminate more than one event per 0.93 μs bunch, and that the detector recovery time in the absence of

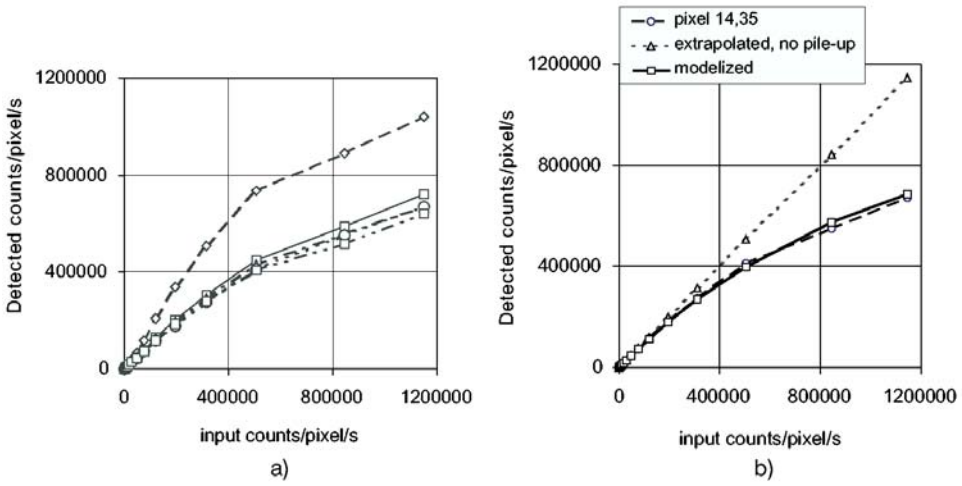

Figure 4.5: a) *Response of four individual pixels as a function of input rate. The input photon rate is calculated from the beam intensity and from the absorption characteristics of the silicon sensor.* b) *Simulation of the pixel response.*

secondary hits is shorter than 0.47 μs. These results are compatible with previous measurements performed on the Medipix1 system using regular pulsing and a theoretical 150 ns peaking time of the pixel preamplifier [19].

The non-linearity is reproducible and can be corrected for by using an appropriate calibration procedure. However, since the detector behavior depends on the time structure of the beam, a different calibration is needed for each operational mode of the machine.

4.5 Absolute calibration and noise estimate

To obtain the energy calibration of the detector, different X-ray energies are needed. Beam energies of 6, 8, 13, 15, 18 and 21 keV have been used. The accuracy on these values is 1%, although the energy spread is much smaller (less than 1 eV).

For this study, a beam illuminating a surface of 10 $\times$ 10 pixels has been used. Some bad pixels have been excluded from the analysis, leaving us with a total of 88 good pixels.

Several threshold scans have been performed over this selected area, one for each different beam energy. The chip threshold voltage setting in mV is scanned from 800 mV to 1400 mV in steps of 10 mV. For each value an image has been acquired, and the count rate has been obtained as a function of threshold voltage (S-curve).

The number of counted photons is about 10^4 per pixel at low thresholds,

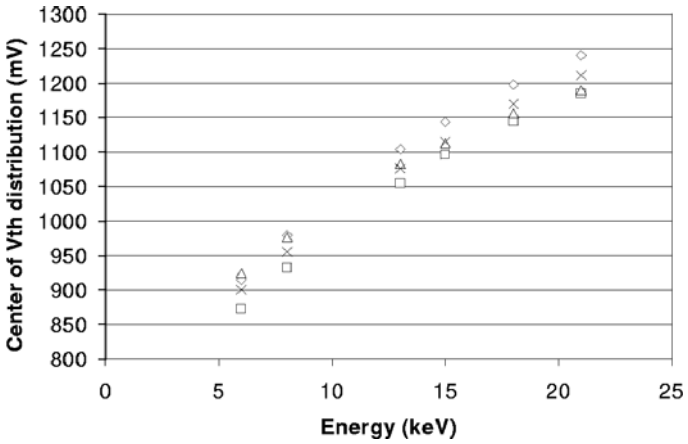

Figure 4.6: Absolute energy calibration curve for 4 arbitrary pixels.

decreasing to almost 0 around the upper limit of the scan. At higher energies the count rate is further reduced because a 300 μm-thick silicon sensor does not fully absorb the X-rays: for instance, at a beam energy of 21 keV, only 22% of the photons are stopped.

For every pixel, 6 S-curves are obtained, corresponding to the 6 different energies employed. The S-curves are then differentiated. The resulting peaked distributions have been fitted with Gaussian functions, giving two useful quantities for our analysis: the center of the differentiated distribution μ_{mV} and the Gaussian spread σ_{mV}, both in mV. So, for every analyzed pixel, 6 values of μ_{mV} and 6 values of σ_{mV} have been calculated up to this point.

For each pixel, the 6 μ_{mV} contain information about the energy calibration, while the voltage thresholds μ_{mV} are plotted as a function of the beam energy (in keV). A quadratic fit then provides the calibration function. In this way 88 calibration functions are obtained, one for each pixel. The calibration functions corresponding to four arbitrary pixels are shown in fig. 4.6.

The 6 σ_{mV} contain information on the Equivalent Noise Charge (ENC) of each pixel, measured as equivalent electron charges on the amplifier input. Using the calibration functions, the σ_{mV} are translated from a voltage value into an energy value expressed in keV, and then from energy to equivalent electrons just by multiplying by 1000 and dividing by k, where:

$$k = 3.62eV/e^{-} \tag{4.1}$$

is the energy needed to create an electron/hole pair in silicon. This calculation is summarized in eq.4.2 and 4.3.

$$\sigma_{keV}^{(j,i)} = f_i(\sigma_{mV}^{(j,i)}) \tag{4.2}$$

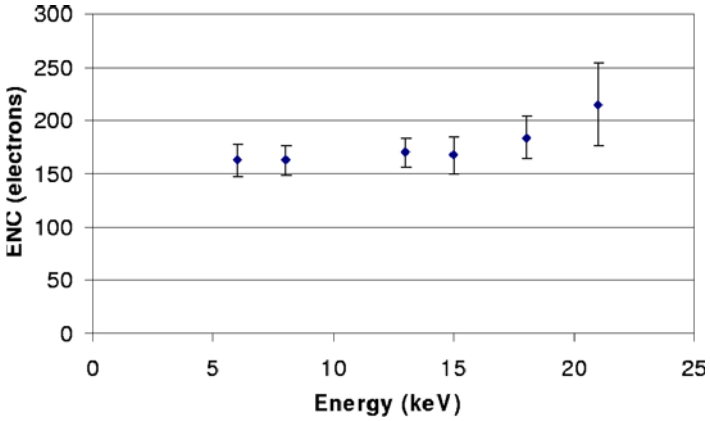

Figure 4.7: Noise (ENC) as a function of X-ray energy, averaged over 88 pixels.

$$\sigma_{ENC}^{(j,i)} = \sigma_{keV}^{(j,i)} \times 1000 \frac{eV}{keV} \times \frac{1}{k} \tag{4.3}$$

with i = pixel index = 1,..,88 and j = energy index = 6 keV, 8 keV, 13 keV, 15 keV, 18 keV and 21 keV. The f_i are the pixel calibration functions.

For each of the 6 different energies we now have 88 ENC values σ_{ENC}, one for each pixel. For each energy, the distribution of the so obtained ENC value over the 88 pixels is studied. These distributions are fitted with a Gaussian function. In fig. 4.7 the mean of this distribution is shown as function of beam energy, while its standard deviation is taken as error bar.

The resulting equivalent noise charge (ENC) of 163 electrons at an X-ray energy of 8 keV is to be compared with our previously reported result of 142 electrons [22], obtained with a different Medipix1 silicon assembly and using only two X-ray energies with linear fits for the energy calibration functions. The average noise over the investigated energy range is estimated to be 170 electrons.

The difference between the firstly reported result of 142 e^- and the present result of 163 e^- can be ascribed to the following causes:

- In our previous publication [22] only two energies (5.5 keV and 8 keV) had been used, while during the characterization at ESRF six energies were used, leading to a more accurate energy calibration
- The two calibrations have been obtained with two different detector assemblies. In general, different detectors may have different noise characteristics, depending on several factors (chip production run, bump-bonding process employed, different semiconductor sensor leakage current which may vary from sensor to sensor).

4.6 Point Spread Function

A pencil beam of 10 μm $\times$ 10 μm has been used to illuminate the center of a pixel. By looking at the counts in this pixel and its neighbors, it is possible to measure directly the Point Spread Function (PSF) of the detector. This is one of the most interesting advantages of using a synchrotron beam for detector characterization.

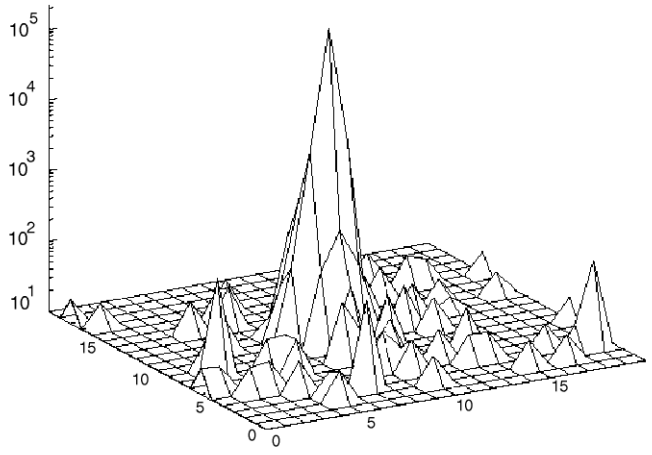

Figure 4.8: The Point Spread Function of the detector is determined by summing 20 acquisitions of 5 s each. Low angle scattering from the collimator or from air contributes to the non-symmetric side peaks in the plot. The vertical axis displays the counts of the pixels (note the logarithmic scale). Both horizontal axis show steps of 10 μm each.

To obtain a high dynamic range, 20 exposures of 5s each have been accumulated. Noisy pixels (a total of 13) have been masked. The resulting PSF is shown in fig 4.8. The central pixel collected 2.5 $\times$ 10^5 counts and its neighbours 5 $\times$ 10^3 (2% of the central counting). The non-symmetric wings are probably caused by scattering from the collimators or from air. At large distances from the illuminated pixel we can see a random background of about 10 counts. This is due to a known design flaw of the Medipix1 detector: the opening and closing of the shutter may increment the counter value by one. Some pixels do not suffer from this effect while others show it continuously.

This effect at present limits the dynamic range. For the Medipix2 chip this design flaw has been completely cured.

4.7 Subpixel sensitivity scanning

A detector area of 510 μm × 160 μm has been probed in 10 μm steps, in both vertical and horizontal directions, using a collimated beam of 10 μm × 10 μm, with one image being acquired at each step. Individual threshold tuning had been applied. In this way it is possible to investigate local inhomogeneities in detection efficiency. These inhomogeneities can be caused by charge sharing between neighboring pixels in the sensor, or by other effects like bump-bonding defects or inhomogeneities in the semiconductor sensor.

Fig. 4.9*a* and *b* show the sensitivity map of a single pixel, reconstructed with a 10 μm beam. In fig. 4.10 the contributions of the different pixels in the scanned area have been summed up to obtain the total map.

The sensitivity map of the entire explored area is particularly flat with neither loss nor doubling of counts between pixels, and only a shallow drop of about 15% at the crossing point between 4 pixels. The responses of adjacent pixels cross at 50% of the counts at pixel centers.

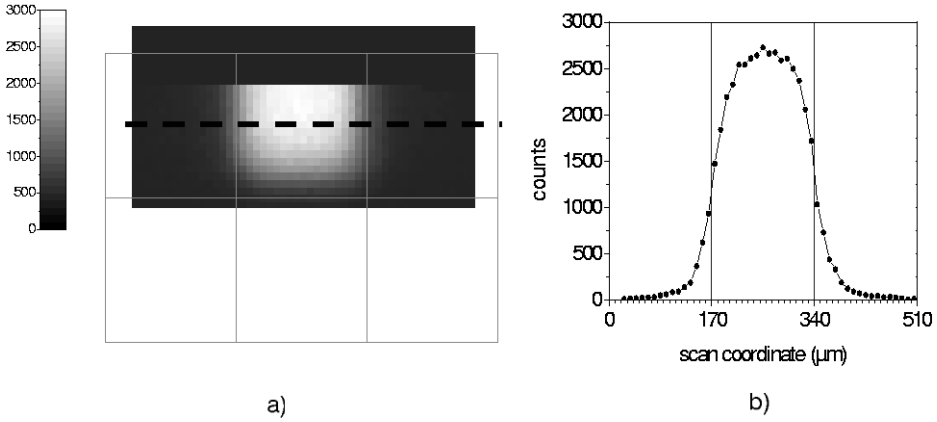

Figure 4.9: Subpixel sensitivity scanning made with a 10 µm square beam. The 3 × 2 grid shows the actual size and position of the detector pixels. a) is a linear greyscale representation of the central pixel response, where the counting areas are represented in white and the non-counting areas in black. b) shows the counts profile along the dotted line in a).

This result demonstrates that individual pixel adjustment allows to properly balance the errors arising from charge sharing between two neighbouring pixels. This confirms also other results previously obtained with a GaAs Medipix1 assembly and 60 keV collimated irradiation, where no intensity loss due to charge sharing between adjacent pixels was found (more information in [32]). Similar results were obtained with other hybrid pixel detector systems [33], thus we can conclude that, at least for monochromatic beams, charge sharing might

no longer be regarded as a major matter of concern for imaging with hybrid pixel detectors.

However, the sensitivity maps obtained also involve some unavoidable contribution from Compton-scattered X-rays at low angle from the beam direction. This can be inferred from the presence of counts at more than 1 pixel distance from the beam center.

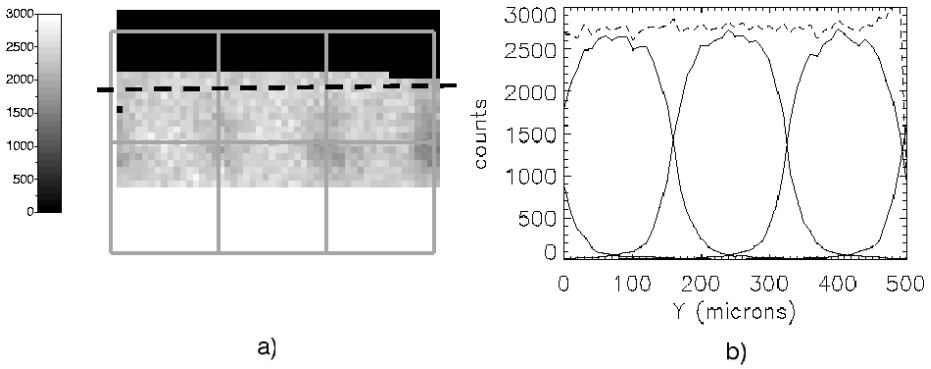

Figure 4.10: Fig. 4.10a shows the sensitivity map of the entire area probed with the pencil beam, obtained by adding up the contributions of all the involved pixels. The superimposed frame indicates position and size of these pixels. Note that the less counting areas (darker) are located near the crossing of 4 adjacent pixels. Fig.4.10b instead shows the counts of every pixel. The dotted line is the total sum, which is approximately constant. These values are taken along the dotted line in a).

4.8 Time resolution

A chopper with tungsten blades rotating with a 10 Hz frequency has been used to modulate beam intensity, with an external signal triggering the acquisition cycle every 10 ms. Each cycle consists of 3 ms count integration, 1 ms detector readout (8 Mbytes/s chip readout rate) and data transfer to the computer, thereby achieving 100 Hz frame rate acquisition with 30% live time.

A sequence of 500 frames has been acquired, a subset of which covering 0.1 second acquisition time (10 frames), is shown in Fig. 4.11. Each illuminated pixel collects about 300 counts, giving sufficient statistics to clearly visualize the beam occultation by the chopper blade. The corresponding absorbed flux rate is 10^5 counts/pixel/s. Showing a major advantage of photon counting detection, the pixel signal is absolutely free from any time lag or blooming (afterglow as shown by many CCDs).

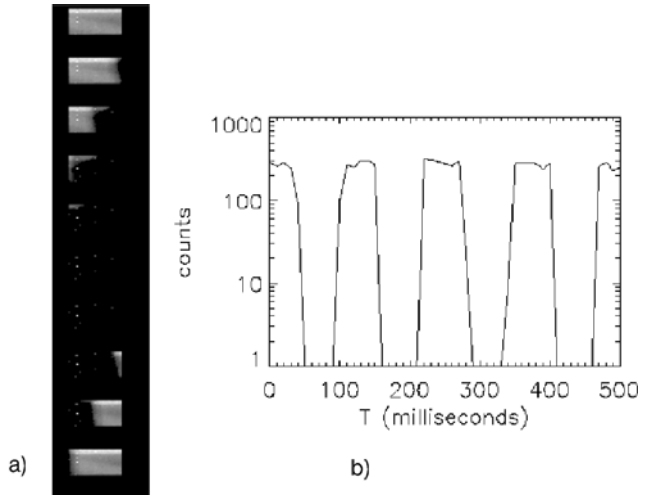

Figure 4.11: Dynamic acquisition at 100 Hz frame rate of a beam modulated with a chopper rotating at 10 Hz. a) A sequence of 10 images covering a time interval of 0.1s. b) Response of one pixel. Note again the logarithmic vertical scale.

4.9 Radiation damage

Submitting the detector to a strong input flux resulted in a permanent noise increase in the irradiated area, which has been interpreted as damage induced on the readout chip by X-rays transmitted through the silicon sensor. The damage is considered permanent since no (partial) recovery has been observed after a few hours.

We estimated the total dose absorbed by the readout chip to be 4 krad (equivalent to 40 Gy or 1.3×10^{10} 13 keV photons/mm^2), while 10 krad have been stopped by the silicon sensor. All these numbers must be regarded only as orders of magnitude estimates.

Since there is an effort to use hybrid pixel detectors also for synchrotron facility applications, radiation tolerance is an important property. Typical operation modes feature intensities of 10^6 photons/mm^2. With an X-ray energy of 13 keV, this might damage the detector in an estimated time of about 8 hours of cumulated exposition. Alternatively, accidental exposure to the direct beam (up to 10^{13} photons/mm^2) as can occur during beamspot alignment may locally damage the detector in less than a second.

The Medipix1 detector has not been designed for radiation-hard purposes. A big improvement is reached with the Medipix2 chip, which is intrinsically radiation hard due to the use of deep sub-micron production technology. This technology is intrinsically radiation hard due to thinner gate oxides, and shallow

trench isolation in the manufacturing process.

Thicker semiconductor sensors (or high-Z materials) with their enhanced stopping power may help improving radiation hardness properties of the detector because they reduce the number of photons reaching the chip. Another improvement can be made by using special radiation hard layout techniques (e.g. transistors with enclosed gates).

4.10 Conclusions

We studied the performance of a Medipix1 silicon assembly during the beam test period at ESRF. This complements the series of measurements that have already been carried out on this detector, mainly with X-ray tubes and radioactive sources.

The analysis of the experimental data leads to several important conclusions. The detector:

- Has a response to X-ray energies as low as 6 keV after individual threshold tuning (which confirms the results previously shown in [22]). Therefore, the detector is suitable for low-energy applications (X-ray Reflectometry, X-ray Diffraction [34] etc.).
- Can handle a readout speed up to 100 Hz frame rate
- Has a pixel-limited point spread function
- Has no signal loss at pixel edges, which demonstrates that charge sharing between neighboring pixels can be compensated by a proper pixel-by-pixel threshold equalization
- Has an average equivalent noise charge (ENC) over the investigated energy range of about 170 e^- (approximately 0.03 fC)

This evaluation confirms the excellent performance of the Medipix1 detector. In addition, we also conclude that counting pixel technology can be successfully applied for X-ray imaging at synchrotron sources.

However, there remain two main drawbacks for high flux applications. The first is insufficient radiation hardness, which is inherent to the electronics chip design technology. This is significantly improved in the Medipix2 chip design. The second is non-linearity in response to high event rates. This can be solved by a proper pixel calibration, which takes into account the time structure of the beam.

Chapter 5

Medipix2

The single photon counting performance of the Medipix1 detector has been further enhanced due to the steady improvements in semiconductor technologies (the Medipix1 chip was designed in 1997). One of the main limitations was in fact the pixel size, 170 μm $\times$ 170 μm, which is determined by the component density allowed by the 1 μm SACMOS process used.

The successor of the Medipix1 readout chip, Medipix2, has been designed in 2001 in 0.25 μm deep submicron CMOS technology by the CERN group of the Medipix collaboration.

In fig. 5.1, the size of the Medipix2 pixel cell is compared to the cell size of its predecessor. The reduction in pixel size is due to the reduced dimensions of the individual transistors as well as the increased number of metal interconnect layers, allowing closer packing of the circuits.

As a result, spatial resolution is enhanced. The input noise to the chip readout electronics is reduced because the capacitance of the sensor diode bump-bonded to the cell depends on the junction area [1]. Due to these improvements, a Medipix2/silicon sensor assembly is capable of detecting X-rays energies as low as 4 keV (compared to the measured 5.5 keV minimum energy for the Medipix1 detector).

Thus, spatial resolution is now becoming comparable to that offered by the less complex integrating systems, without losing any of the many advantages offered by a hybrid pixel detector, like, for instance, excellent signal-to-noise ratio and dynamic range. Furthermore, the new chip has several additional features:

- Polarity is selectable between both positive and negative charge carriers (while Medipix1 could only detect positive charge)
- Single or double threshold operation modes (energy-windowing)
- Leakage current compensation on a pixel by pixel basis (not per column as in Medipix1 - as the leakage current of the sensor may change due to

[1] For small pixels, the input capacitance is dominated by interpixel capacitance

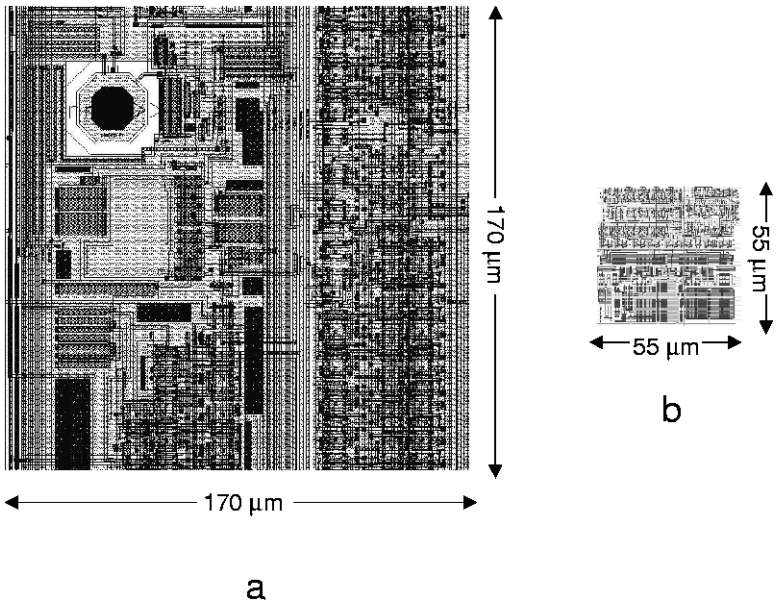

Figure 5.1: Size comparison between a Medipix1 pixel (a) and a Medipix2 pixel (b). This reduction in area of approximately a factor of 9 is allowed by the deep submicron 0.25 CMOS technology used for the design of the Medipix2 chip, in contrast with the 1 µm CMOS technology employed for the Medipix1. The bump-bonding pad is clearly visible in the case of Medipix1, where it is separated from the electronics circuitry. In Medipix2, more metal layers are available and the bumping pad is on top of the electronics circuitry and is not shown here. It covers about 20% of the pixel area.

radiation damage, which in general will not be uniformly distributed over the column)

Special multi-chip tiled array applications of the chip are also a goal of the Medipix2 project (see chapter 6). For this reason, the design was optimized to minimize the dead area between adjacent chips in large-area detectors, as explained in next section.

5.1 Description of the Medipix2 chip

Like Medipix1, the Medipix2 readout chip is also made up of a *periphery* (which includes structures common to all the pixels, and the bonding pads) and a *sensitive area* (the one segmented into readout cells). See fig 5.2 for a picture of the chip.

While this was not an issue in the case of the Medipix1 detector, now the chip area had to be organized in the most efficient way to minimize the dead

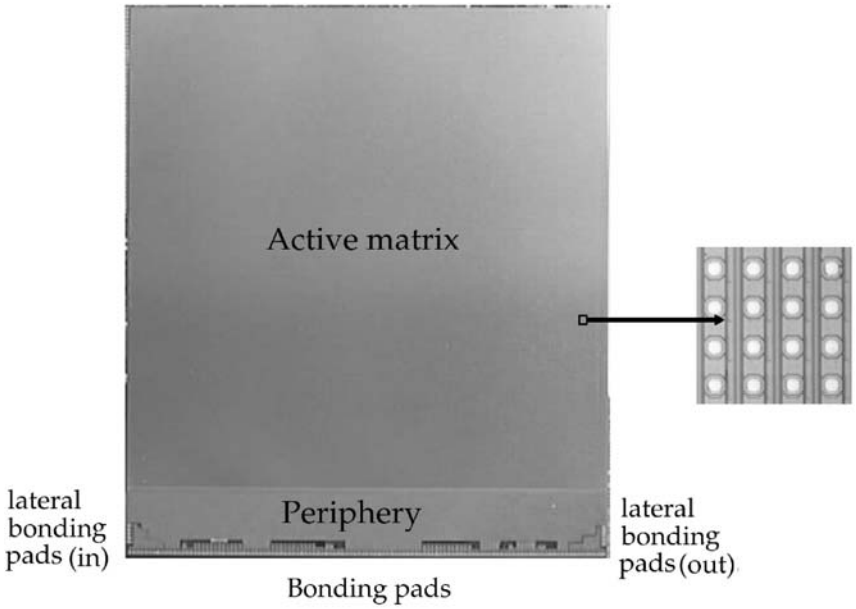

Figure 5.2: A picture of the Medipix2 chip, showing the pixel matrix (top) and the chip periphery (bottom). Chip dimensions are 14.111 × 16.120 mm.

area between neighboring chips. This in view of large area tiling applications, where several Medipix2 chips are connected to the same large semiconductor sensor and read out either as a serial daisy chain or in parallel. Such operation mode was not yet a goal for the Medipix1 chip.

In order to meet this requirement, all the periphery is placed at the bottom of the chip, while the other 3 sides have been designed so that the non-sensitive area at the edge is less than 50 μm wide. With this disposition, one side of the chip is used to connect through aluminum bond wires to the readout system and power lines. The three other sides can be adjacent to other Medipix2 chips. The Medipix2 readout chip is thus said to be *3-side buttable*.

The sensitive area is organized as an array of 256 × 256 identical cells of size 55 μm × 55 μm, resulting in a detection area of 1.98 cm^2 (87% of the total chip surface). The periphery contains:

- 13 8-bits DACs for setting and tuning the working point of the chip
- A 256-bit FSR (Fast Shift Register, 1 bit per column) used to read from and write to the matrix
- LVDS (*Low Voltage Differential Signaling*) drivers and receivers for fast

serial daisy chaining

- The Input/Output logic that controls the chip operation
- The 127 I/O wire-bonding pads for connection with the readout system.

A serial daisy chain between chips can be realized thanks to 5 lateral IO bonding pads that allow a direct connection with the neighbouring chips (see fig 5.2).

In a similar way to the Medipix1 chip, the Medipix2 chip has two working modes depending on the CMOS input *Shutter* state. When the Shutter signal is low, the pixel is in acquisition mode and the detected photons are counted. When Shutter is high, an external clock is used to shift the data from pixel to pixel.

When the matrix is accessed to perform any I/O operation the data is organized in 256 columns of 256 $\times$ 14 bits. Therefore each chip has 917504 bits (almost 1 Megabit) to be read or written for any pixel-array operation. The Medipix2 chip uses a serial high-speed LVDS (Low Voltage Differential Signaling) input for setting the configuration bits of the entire pixel matrix and for setting the 13 DACs (which in turn set the different bias voltages on the chip). Readout can be either performed serially through the LVDS output or in parallel by using a parallel 32-bit single-ended CMOS output bus. However, the loading and reading of the 13 8-bit DACs and of the configuration register in the entire matrix is always done serially through the LVDS transceivers.

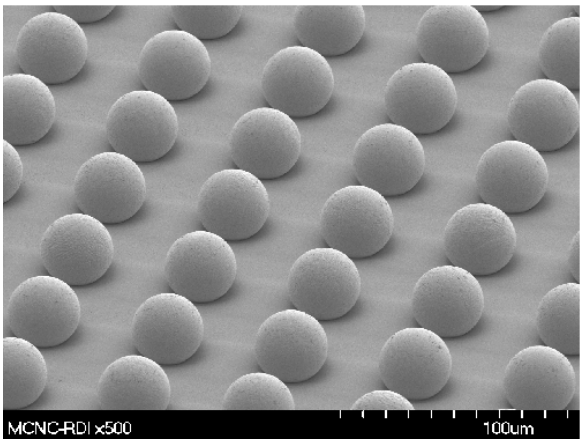

Figure 5.3: Medipix2 uses eutectic Pb/Sn solder bumps of 25 μm diameter and 55 μm pitch, for a resulting density of about 40000 connections per square centimeter. A yield close to 100% is now routinely obtained, with only a few tens of non-connected pixels per chip (picture: courtesy MCNC [35]).

The Medipix2 chip is bump-bonded to a semiconductor sensor (see fig.5.3

Pixel size	55 μm × 55 μm
Number of pixels	256 × 256
Sensitive area	14.11 mm × 14.11 mm
Max. counting rate (pixel)	1 MHz/pixel
Max. counting rate (pixel)	330 MHz/mm^2
Min. threshold	1100 electrons
Threshold spread (not adjusted)	450/250 e-/h+
Threshold spread (adjusted)	120 electrons
Maximum input signal	80000 electrons
Mean total noise (without sensor)	100 electrons
Mean total noise (with sensor)	140 electrons

Table 5.1: Characteristics of the Medipix2 detector (values measured on a Medipix2/300 μm Si sensor assembly).

for a view of the bumps). Different types of semiconductor materials are employed depending on the specific application of each individual assembly. For low-energy X-ray detection, silicon sensors are used, while for higher energies Cd(Zn)Te is employed. High stopping power is achieved also by having thicker sensors. Detectors of 700 μm thickness have been produced in addition to the standard 300 μm thick type.

A summary of the (measured) characteristics of the Medipix2 detector is shown in table 5.1 [36].

5.1.1 The Medipix2 pixel cell

The layout and the schematics of the Medipix2 pixel cell are shown in fig. 5.4 and fig. 5.5 respectively.

The analog part of the pixel contains a charge preamplifier with leakage current compensation, a test capacitance and two identical discriminators. The digital side contains the Double Discriminator Logic (DDL) and a 14-bit shift register.

Each pixel has 8 independent configuration bits. Six are used for individual threshold adjustment (three bits for the lower threshold and three for the high threshold), one for masking noisy pixels and one to enable the input charge test through the 8 fF on-pixel capacitance.

An input bump-bonding pad is also present on the top metal layer.

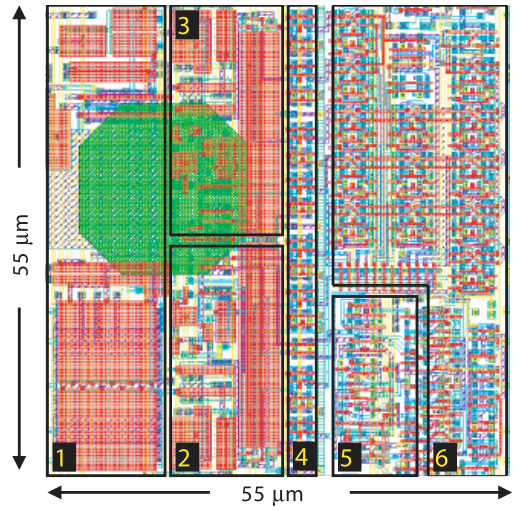

Figure 5.4: Layout of a Medipix2 pixel cell. 1) Preamplifier, 2) High Threshold comparator, 3) Low Threshold comparator, 4) 8-bit configuration register, 5) Double Discriminator Logic, 6) Shift Register and control logic.

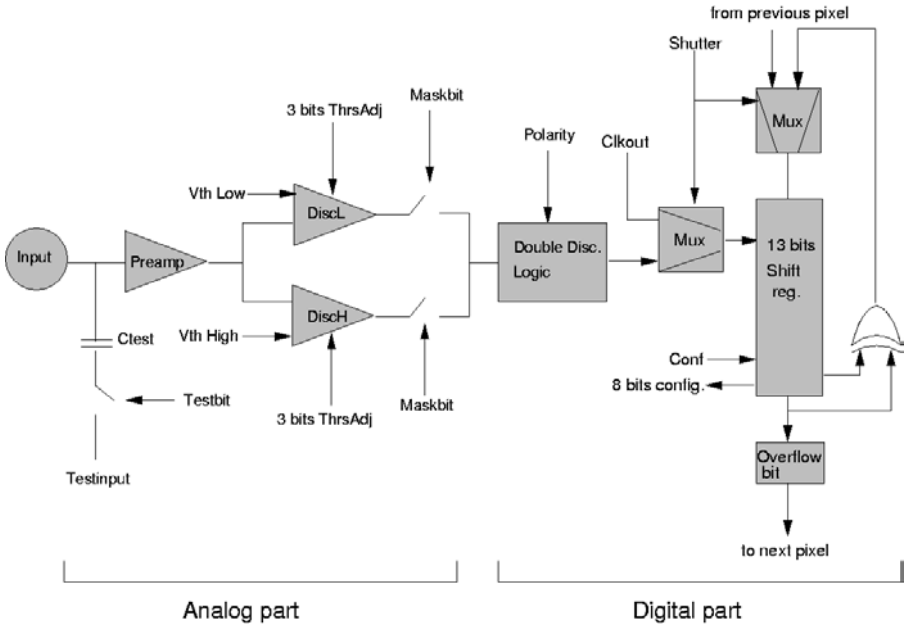

Figure 5.5: Block diagram of a Medipix2 pixel cell.

5.1.1.1 The charge preamplifier

The Medipix2 preamplifier follows the Krummenacher scheme [37], which is based on a differential CMOS input amplifier (see fig. 5.6). This design provides a better rejection of substrate and power supply noise (common mode rejection).

DC leakage current compensation has been implemented in each pixel. This compensation is operated by the M2 transistor. Positive DC leakage currents (hole collection) smaller than the *Ikrum* current DAC and negative leakage currents (electron collection) smaller than *Ikrum*/2 can be compensated in each pixel. The design values have been well overestimated to fit the design specifications (see table 5.2).

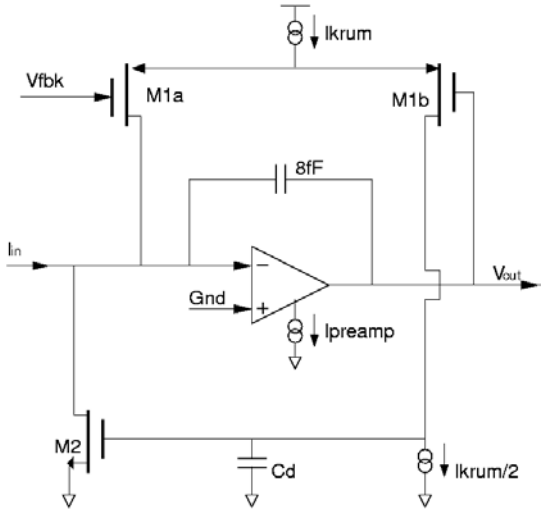

Figure 5.6: Block diagram of the Medipix2 preamplifier. A preamplifier is present in each pixel cell; it is sensitive to both positive and negative going pulses, and is capable of leakage current compensation.

The preamplifier can collect either positive or negative charges: the polarity of the charge collection is selected using the *Polarity* input pad. The Vfbk node is controlled by a voltage DAC. This node sets the DC output voltage, which optimizes the dynamic range depending whether holes or electrons are being collected. Changing the Vfbk voltage affects the overall gain of the preamplifier due to the change in the biasing point. This results in slightly different gains for the two collection modes (see table 5.2).

5.1.1.2 The threshold discriminators

Two identical comparators are included (instead of only one as in the case of the Medipix1 chip). Each of the them has three main blocks (see fig. 5.7): an

	Electron collection	Holes collection
Polarity	Low	High
Vgnd (default)	1.1 V	1.1 V
Vfbk (default)	600.2 mV	1.605 V
IPreamp (default)	700 nA	700 nA
Ikrum (default)	14 nA	14nA
Gain	12.5 mV/ke-	13.25 mV/kh+
Peaking time	150 ns	150 ns
Linearity	Up to 100 ke-	Up to 80 kh+
Leakage current compensation	0 to 7 nA per pixel 0 to 2.3 μA/mm^2	0 to 20 nA per pixel 0 to 6.6 μA/mm^2
Output noise	90e- (Ileak = 0 nA)	120h+ (Ileak = 10 nA)

Table 5.2: Medipix2 preamplifier settings and characteristics (simulated values)

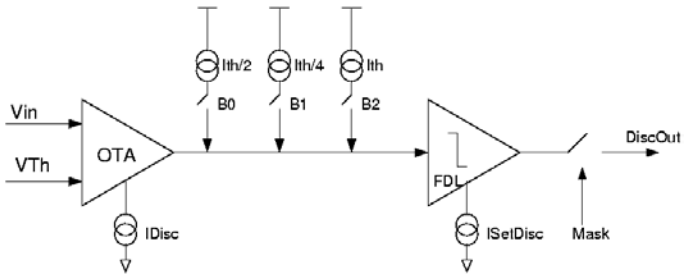

Figure 5.7: Block diagram of the discriminators present on each pixel of the Medipix2 chip. Each pixel has two discriminators for operation in window mode, but since they are identical only one is shown in figure. The OTA amplifier, the 3-bit threshold adjust and the fast logic FDL are visible.

OTA amplifier (Operational Transconductance Amplifier), the 3-bit threshold adjust and the FDL (FastDiscriminatorLogic) circuitry.

The differential amplifier is configured to work as an OTA. It takes as input the output voltage of the pixel preamplifier, and generates an output current proportional to this voltage. This current is positive if the input voltage V_{in} is higher than the main voltage threshold V_{Th}. The current is negative if V_{in} is lower than this main voltage threshold. The value V_{Th} is a global value of the threshold common to all the pixels in the chip, and it is set through an 8-bit DAC. Since there are two independent discriminator branches for operation in window mode, two independent 8-bit DACs are needed (one for each branch): V_{thL} for the low threshold discriminator and V_{thH} for the high threshold discriminator.

The OTA output current goes to the FDL. The FDL switches its digital output when the input current crosses the zero value. There is also an external

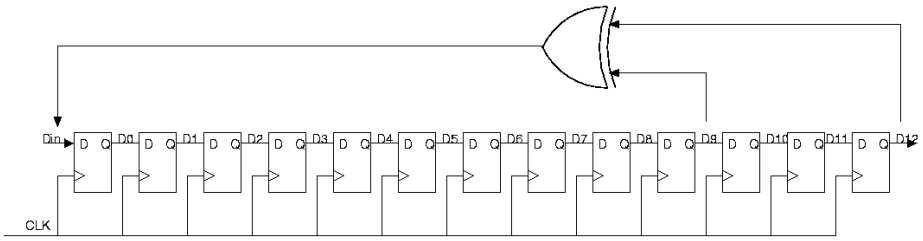

Figure 5.8: When the Shutter *signal (see fig. 5.5) is low, the 14-bit Shift Register acts as a pseudo-random counter.*

control line to mask out the digital output of the pixel. This can be used to switch off the output of noisy pixels that are malfunctioning (usually overcounting).

5.1.1.3 Double Logic Discriminator

The digital outputs from the two discriminator circuitries are given as input to the *Double Discriminator Logic* (DDL). Two working modes are possible:

- Single threshold mode: this mode is set when the high threshold level is lower than the low threshold level. An output pulse is generated when a hit from the low threshold discriminator is received (and the output of the high threshold discriminator is ignored).

- Energy window mode: this mode is set when the high threshold level is higher the the low threshold level. An output pulse is generated when a hit from the low threshold discriminator is received and at the same time no hit is received from the high threshold discriminator.

5.1.1.4 Shift Register

The shift register has two modes of operation, depending on the state of the *Shutter* signal.

- Shutter = 0. When *Shutter* is low the shift register works as a pseudo-random counter of 13 bits. An exclusive-OR operation is performed between the 9^{th} and 12^{th} bits, and the result is sent again as input to the first bit (see fig. 5.8). The output of the counter is then compared to a look-up table in the software, and the value of the counter is then established. The maximum number of counts that can be reached with this technique is 8001. After this value, the pseudo-random sequence repeats from the start. A 14^{th} overflow bit is also present: when the maximum count of 8001 is reached, the overflow logic detects an overflow and sets the overflow bit (14^{th}) to 1.

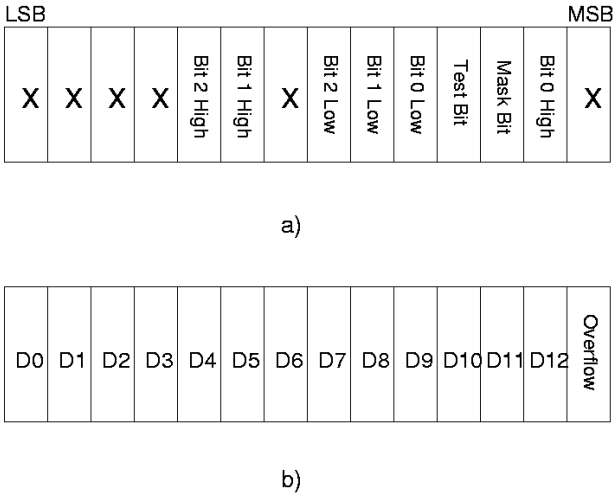

Figure 5.9: When the Shutter *signal is high, an external clock is used to shift the data from pixel to pixel. When the configuration matrix is being set, the data structure is shown in* a) *(*Low *refers to the Low Threshold and* High *refers to the High Threshold).When the counter information is being read out, the data structure is as shown in* b)*.*

- Shutter = 1. When *Shutter* is high the 14-bit shift register of each pixel is connected to the next and previous pixel in a column to form a 3584-bit register. Data flows along the column from top to bottom using an external clock. This mode is used both for setting the 8 configuration bits of the pixel (fig. 5.9a) and for reading the content of the 14-bit counter (fig. 5.9b).

5.1.1.5 Pixel Configuration Register

Through this 8-bit register, the pixel can be configured independently from the others. The configuration parameters are:

- 3-bit Low Threshold Adjust
- 3-bit High Threshold Adjust
- Test_Bit: enables the external testing of the pixel via a test pulse. If its value is 0, the test is disabled, if the value is 1, the test is enabled.
- Mask_Bit: masks out the pixel cell. Very noisy pixels are overcounting and not reliable for imaging. Usually, their contribution is not taken into account in the image - they are masked out. If the value of this configuration bit is 1, the pixel is enabled, if it is 0 the pixel is disabled.

5.1.2 IO logical description of the Medipix2 chip

The Medipix2 pixel readout cells are organized as a 256 × 256 matrix. All the Input/Output operations are based on 256 × 14-bit = 3584-bit columns (see fig. 5.10). The communication between the pixel matrix and IO logic is done through the 256-bit FSR. For yield reasons, two identical and independent FSRs have been implemented, since this is one of the most critical parts of the IO path. The FSRs are externally selectable through the *SPARE_FSR* input line.

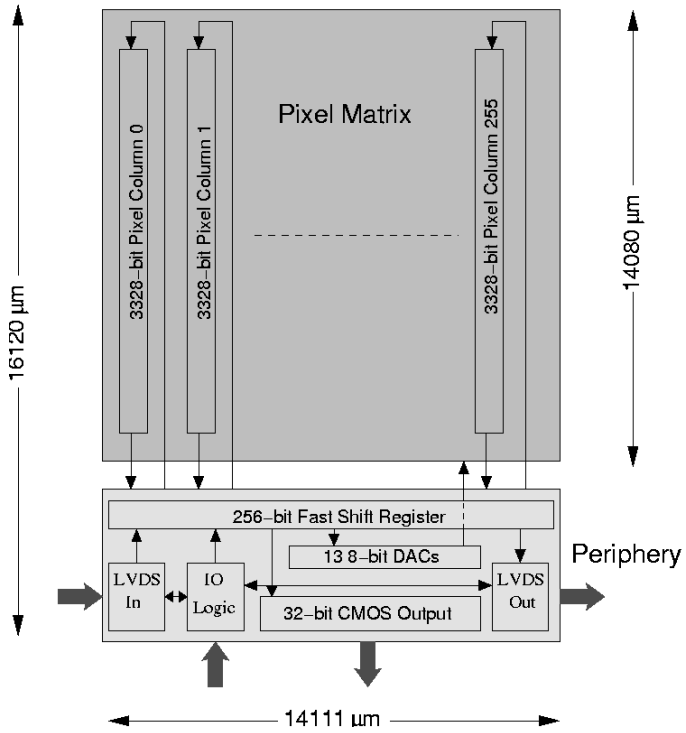

Figure 5.10: IO block diagram of the Medipix2 chip.

The Medipix2 chip has several possible IO operation modes, which are set by the *M0, M1, ENABLE_IN, SHUTTER* and *RESET* lines as shown in table 5.3. These different operation modes are:

- General reset of the chip: the *RESET* line is the master for all the other control lines. When its value is Low, a general reset of the chip is performed: the LVDS drivers are not active, the FSR are set High, the IO counters are reset to default and all the DACs are set to mid-range values.
- Counting mode: when Reset is High and Shutter goes Low, each pixel is ready for counting.

M0	M1	ENABLE_IN	SHUTTER	RESET	OPERATION
X	X	X	X	0	General reset
X	X	X	0	1	Counting mode
0	0	0	1	1	Matrix readout
0	1	0	1	1	Matrix setting
1	0	0	1	1	DACs setting
1	1	X	1	1	Matrix reset
0	1	X	0	1	FSR test

Table 5.3: IO operation modes of the Medipix2 chip. Each specific mode is selected via the M0, M1, ENABLE_IN, SHUTTER and RESET lines.

- Matrix readout mode: if M0 and M1 are both at Low status and Enable_In goes low, then the matrix readout operation is started. An external clock must be provided through an LVDS line. The readout can be performed in two different ways: serial readout or parallel readout. The selection is made via the P_S pin:
  - Serial readout (P_S=0): the serial readout uses an LVDS line to transfer all the data stored in the the pixel counters for the full matrix. The number of clock cycles needed to readout one chip is $8 + 256 \times 256 \times 14 = 917512$ (the first 8 bits are due to the 8-bit preload register, and the rest is the total number of bits in the matrix). If there is more than one chip to be read, the procedure is similar, but in this case the total number of cycles is N $\times$ 917512, where N is the number of chips.
  - Parallel readout (P_S=1): the parallel readout uses a 32-bit CMOS-HiZ bus to shift all the data in the shift register. The number of clocks necessary to shift out the data for one chip is $256 \times 8 \times 14+8=26632$. If more than one chip has to be readout in a daisy-chain mode, there will be a gap of 8 clock pulses between two neighbouring chips.
- Matrix setting mode: the 8 configuration bits of every pixel in the matrix are set (serially) through the LVDS lines. In a multichip system the configuration of a chip is loaded only after the configuration of the previous chip has already been carried out. When the configuration of all the chips has been loaded, ENABLE_IN is high, and the data in each pixel shift register is transferred to an 8-bit static flip-flop. The number of clocks needed to set the configuration of one chip is $8 + 256 \times 256 \times 14 = 917512$.
- DACs setting mode: this operation sets the 13 8-bit DACs present on the Medipix2 chip. The value of each DAC is set through the 256-bit FSR. The FSR is loaded serially using the LVDS port and the transferred values are stored in an 8-bit parallel register. The time needed to load the DACs values is $256 + 8 = 264$ clock pulses for one chip, or $256 \times N + 8$ in system with N chips. Note that the setting of the DACs uses only $13 \times 8 = 104$

bits out of the 256 bits of the FSR. An extra 5 bits are reserved for two special operations: the use of an external DAC to substitute any of the on-chip DACS, and the sense-out of the value of each DAC. Every time a Reset operation is performed, all the DACs are set to the mid-range value (binary value = 10000000, decimal = 128).

- Matrix reset mode: all the counter bits of each pixel in the matrix are set to 1. If more than one chip is present in the system, this operation is performed in parallel for all the chips in the daisy chain. The time needed to perform this operation is $256 \times 14 \times 8 + 8 = 28680$ clock cycles.

- Fast Shift Register test: the FSR present on the chip is tested with this operation mode. The data is sent from the DATA_IN LVDS port to the DATA_OUT LVDS port through the FSR. If the output data is different from the input data, the Fast Shift Register has failed and it is not functioning properly.

5.2 Additional features of the Medipix2 chip

Two more important test features are present in the Medipix2 chip. The first is the possibility to see the analog output of the preamplifier for a few adjacent pixels in the matrix. The second is the possibility to send an analog test pulse to the matrix.

5.2.1 The Charge Sharing Test (CST)

This feature is implemented only for nine pixels. These pixels are arranged as a 3×3 matrix, located at the bottom row of the chip, approximately in the center of the line (rows 0-1-2 of the total range of 0...255, and columns 121-122-123 of the total range of 0...255 - see also fig. 5.11). The preamplifier analog output of these pixels is connected through a double stage analog buffer to nine output pads.

The most important application of this feature is the *Charge Sharing Test* or *CST*. If one of these nine pixels (which are usually referred to as *CST pixels*) is hit, the amplifier response of its neighbouring pixels can be studied by reading the CST analog output.

In some cases, despite the fact that the photon has hit a single pixel in the semiconductor sensor and converted inside, a signal can be observed also on the adjacent pixels. This is mostly due to the lateral diffusion of the electron/hole cloud created by the primary electron. Sometimes the signal collected in the neighbouring pixels can rise above the discriminator threshold, and will generate a count.

An additional output pad carries the result of an OR operation between the digital outputs of the low threshold discriminator of all the nine CST pixels. This digital signal is used as trigger for the CST test.

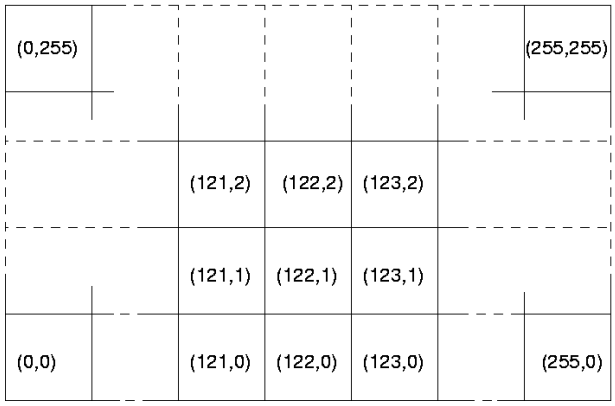

Figure 5.11: Position of the nine Charge Sharing Test pixels in the Medipix2 pixel matrix.

5.2.2 Test pulse

It is possible to send a test pulse to the entire pixel matrix. In this way the functionality of each pixel can be tested without an X-ray source. Test pulses are also used for procedures like calibration and threshold equalization.

The test pulses have to be sent from an external pulse generator. Each pixel has an 8fF test capacitance which allows an individual input charge test. The equivalent input test charge to the pixel preamplifier can be calculated:

$$Q = \frac{0.825 \times (2.2V - V_{test}) \times 8fF}{1.6 \times 10^{-19}C} = 0.825 \times (2.2 - V_{test}) \times 50ke^{-} \qquad (5.1)$$

where V_{test} is the amplitude of the test pulse, 0.825 is the simulated value for the gain of the analog buffers, 8 fF is the value of the test capacitance of the pixel, and 1.6×10^{-19}C is the charge of the electron. The analog buffer is linear between 0.8V and 2.2V. The maximum test charge that can be injected is approximately equal to 60 ke^{-}.

Two analog buffers are positioned at the bottom of every column. Their function is to minimize the voltage pulse rise/fall time, due to the capacity and resistance of the internal electrical connections. These two buffers limit the maximum input test charge, due to their linearity and gain.

A rising or falling edge of the test pulse reproduces a positive (hole collection) or negative (electron collection) charge at the pixel preamplifier input (respectively), depending on which collection mode has been selected.

5.2.3 Fine threshold tuning

The main threshold value is globally set for the full matrix, but additional threshold fine tuning for each individual pixel is available. Optimization is

achieved in the following way: each discriminator branch has three independent selectable current sources. Their value is controlled by the V_{Ths} DAC, which gives currents in the range I_{th} = 0 - 200nA. These sources are selectable through 3 external bits and behave like a 3-bit current DAC.

A *threshold mask* is calculated via software algorithm for each chip. This mask file contains three types of information for each pixel (see also section 5.1.1.5):

- *Enable mask*: the pixel is enabled or disabled
- *Low threshold configuration*: the 3-bit setting that determines the low threshold correction for the pixel
- *High threshold configuration*: the 3-bit setting that determines the high threshold correction for the pixel

Equalization minimizes the spread of the threshold distribution over the whole detection area. A good uniformity of the discriminator levels allows an equalized chip to operate at a significantly lower threshold. Threshold distributions prior to and after equalization are shown in fig. 5.12.

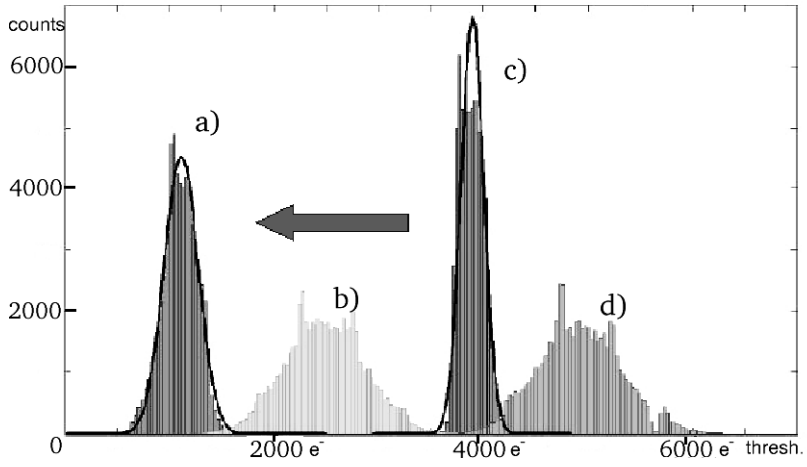

Figure 5.12: Threshold equalization procedure: b) and d) represent the unadjusted distributions for the low and high discriminators respectively. After equalization, the distributions a) (low) and c) (high) are obtained.

5.3 The Medipix2 Serial Readout

The readout of the Medipix2 is possible in both parallel and serial modes. At NIKHEF the serial solution has been developed, while other members of the

collaboration are developing parallel readout systems [38]. A representation of a typical readout setup is given in fig. 5.13.

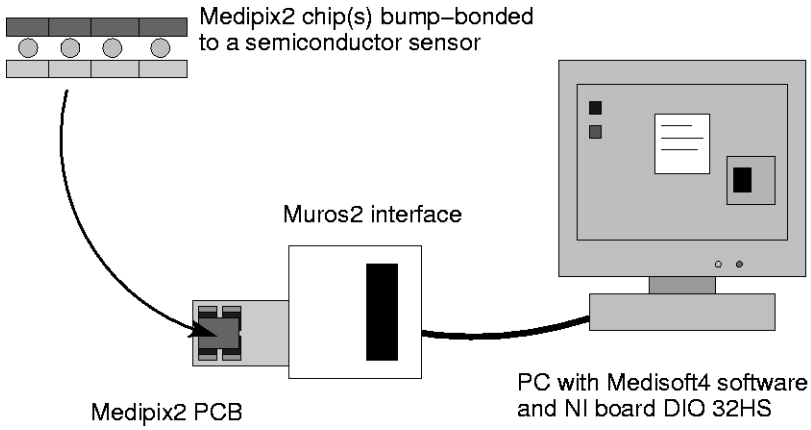

Figure 5.13: A typical Medipix2 setup consisting of one or more Medipix2 chips bump-bonded to a silicon sensor, mounted on a chipboard and connected to a PC through the Muros2 interface.

The serial readout chain is organized as follows. A variable number of Medipix2 chips arranged into an array is bump-bonded to a sensor and glued onto a chipboard. The chipboard is a standard *Printed Circuit Board* (PCB), used for single chip applications, or a more advanced chipboard realized in build-up technology, capable of hosting up to 8 chips (see Chapter 6). Electrical contacts from chips to chipboard are obtained through wirebonding.

The chipboard is connected through a SCSI cable to the Muros2 board [39], which interfaces the Medipix2 chip to a standard PC equipped with a National Instruments data acquisition board. On the Muros2 interface, the control and data acquisition subsystems are implemented in an FPGA, since the use of programmable logic allows maximum flexibility. The Muros2 also includes a clock generator and a test pulse generator. Another fundamental function of the Muros2 board is the translation between the different logic levels on the PC (TTL), the FPGA (3.3V CMOS) and the Medipix2 chip (2.2V CMOS and LVDS). Fig. 5.14 shows the Muros2 board.

The Medipix2 serial readout system requires only one single National Instruments board, the PCI-DIO 32HS (or an equivalent model like for instance the PCI-DIO 6533) since the on-chip DACs generate all analog bias voltages.

The user controls the system through a standard PC running Medisoft software version 4.0 [40] or higher. This package is written in ANSI C under the LabWindows/CVI development environment, and provides the user with a suitable interface for data acquisition operations. Several other routines are included in this package, for instance routines for image manipulation and display, threshold

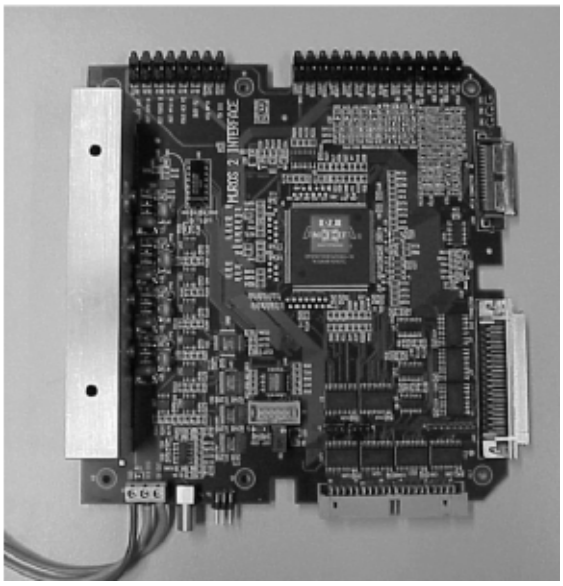

Figure 5.14: A view of the Muros2 interface. The programmable logic is visible at the centre of the board. Dimensions are 16 × 16 cm^2.

equalization, and threshold scans.

5.4 Medipix2 production and quality control

As contrary to the Medipix1 chip, the processing steps are performed on 200 mm diameter silicon wafers (see fig. 5.15), which allows 94 chips to be realized on each wafer. However, due to production defects and impurities in the silicon, the yield will be lower than 100%. Chips are carefully selected prior to the bonding process.

The test set-up is similar to the one for the Medipix1. A custom design probe card is used for wafer probing. Connected to the Muros2 board and provided with 75 needles, it makes possible to contact the test pads on the chip under investigation. In this way the chips can be read out and tested while still on the wafer.

The probecard is mounted in a wafer probing station. The Medipix2 wafer under test is fixed (through vacuum suction) onto a translation chuck below the probecard position. Contact is then made between the probing needles and the testing pads on the chip. Measurements are performed, and then the probe station can automatically step to the next chip.

At the end of a wafer probing test, a *wafer map* summarizes the most important measurements. Next, those chips are selected that pass a set of selection criteria. An example of Medipix2 wafer maps is given in fig. 5.16.

Figure 5.15: A 200 mm diameter wafer contains 94 Medipix2 chips.

5.5 Medipix2 wafer testing procedure

For each chip on the wafer, several tests have to be performed. Depending on how many of these tests are successful, the chip is classified.

- Power consumption check. Very high current consumptions (more that 300 mA) are a clear sign of a malfunctioning chip. This is a quick test to discriminate malfunctioning chips

- FSR test: the correct behaviour of the Fast Shift Register in the chip periphery is tested for basic communication with the chip. If it is failed, the chip is classified as *BAD*, and cannot be used in subsequent applications. Usually, chips giving a bad FSR also have a high power consumption and vice-versa, but some chips have the correct current consumption and yet their FSR test is negative. Some of these non-working chips can be recovered: their bad behaviour is probably due to some flaws in the probing setup, and at a later stage (after being wirebonded to a chipboard) some of them may prove to work. They are marked as *recoverable*.

- CSR test: a matrix of random numbers is written to the pixel matrix and then read back. Each pixel that returns back the same number is considered a digitally good pixel, while each pixel that gives back a different

number is considered a dead pixel. The information is recorded and used for chip classification together with the successive tests.

- DAC test: a calibration of the 13 DACs of the chip is performed. Digital values from 0 until 255 are sent to each DAC, and the analog value given by the DAC is read and plotted versus the digital input. If several DACs fail, the chip is classified as *not correctly working*. It can be used for some electrical tests, but will further be ignored. If only a single DAC is not correctly working, the chip can be recovered through the use of an *external DAC*, and the successive tests in the testing chain are performed.

- Noise platform test: several image acquisitions are performed while lowering the low threshold. Initially, no counts are seen, since the noise is removed by the comparator. But for very smalll thresholds, the chip starts counting the noise. The corresponding image is called *noise platform* and it is useful for understanding the homogeneity of the pixel matrix. The image is saved and used for the subsequent classification of the chip.

- ANIN test: during this test, a fixed number of pulses (usually 1000) is sent to the input of the pixels. The lower threshold is then optimized to have an uniform response. With a perfectly working chip, every pixel should display a count of 1000. However, this is not always the case. Very often non-working columns are present and many pixels (sometimes even entire areas of the chip) may be overcounting, or not counting at all.

If the chip under test has successfully passed the first four tests it is considered a good chip. Depending on the outcome of the last two tests, a good chip is further classified as *class A, class B* or *class C*. A class A chip has no dead columns and less than 5% of dead pixels. A class B chip has less than 10 dead columns and less than 10% of dead pixels. A class C chip is a good chip which either has more than 10 dead columns or more than 10% non-working pixels.

The wafer maps in fig. 5.16 correspond to wafers from two different Medipix2 productions. Earlier runs gave a very low yield. This lead to a subsequent series of investigations in close contact with the manufacturer. It turned out that the dielectric between two of the metal layers in the chip was too thick, and the subsequent via etching process failed.

Therefore, waferprobing is essential for giving immediate feedback to the manufacturer. Table 5.4 shows the yield improvement over time.

	Class A	Class B	Class C	Total working chips
First batch (Jan. 2002)	4.25%	2.1%	-	6.35%
Second batch (Jan. 2002)	16.0%	12.8%	5.3%	34.1%
Third batch (Aug. 2003)	57.4%	16.0%	6.3%	79.7%

Table 5.4: Average fraction of good chips per wafer, for three different production runs. A defect in the production procedure was found. The last batch of Medipix2 wafers is significantly better than the previous two, with a yield of approximately 80%.

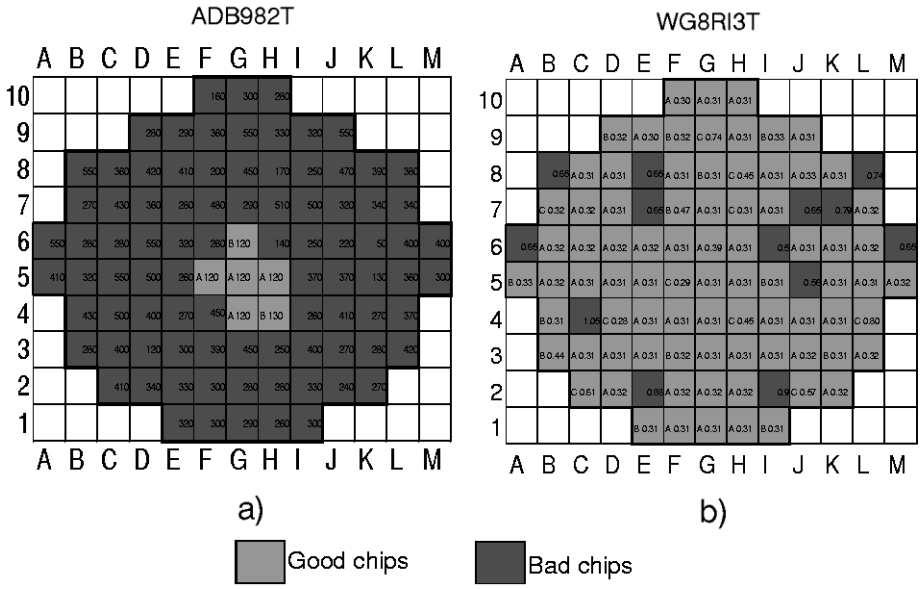

Figure 5.16: Wafermaps corresponding to the wafers ADB962T *(a) and* WG8RI3T *(b). ADB962T is one of the first wafers that have been produced, and all the wafers in that batch showed the same behaviour (only a few good chips in the wafer centre, surrounded by non working chips). After a careful evaluation of the processing steps by the chip manufacturer, a much better wafer quality was obtained. Recent production series show a quality comparable to the wafer WG8RI3T.*

5.6 Medipix2 image gallery

In the following pages a few images obtained with Medipix2 300 μm silicon assemblies are shown. Different X-ray sources have been employed.

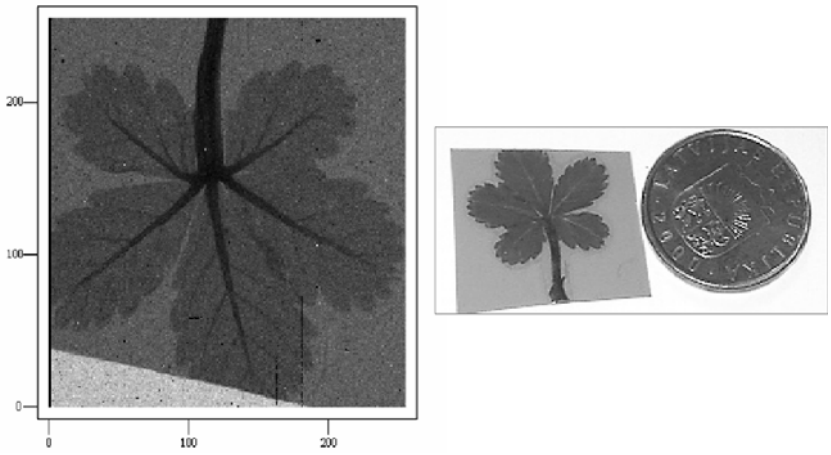

Figure 5.17: Image of a leaf obtained with a Medipix2-silicon assembly (300 μm thickness) and a Fe^{55} source. Exposure time was 10 min. A flat field correction was applied [41].

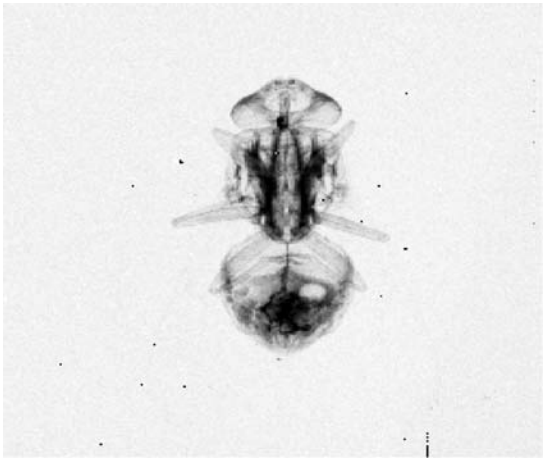

Figure 5.18: Image of a fly obtained with a Medipix2-silicon assembly (300 μm thickness) and a 14 kV W-tube [41].

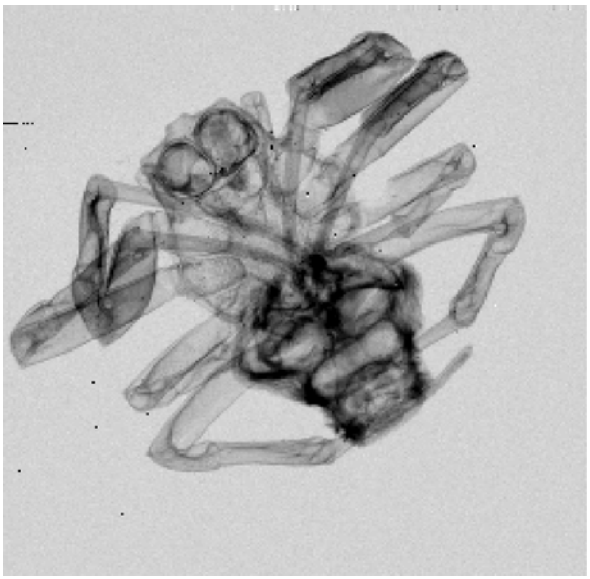

Figure 5.19: Image of a spider obtained with a 300 μm thick Medipix2-silicon assembly and a 14 kV W-tube [42].

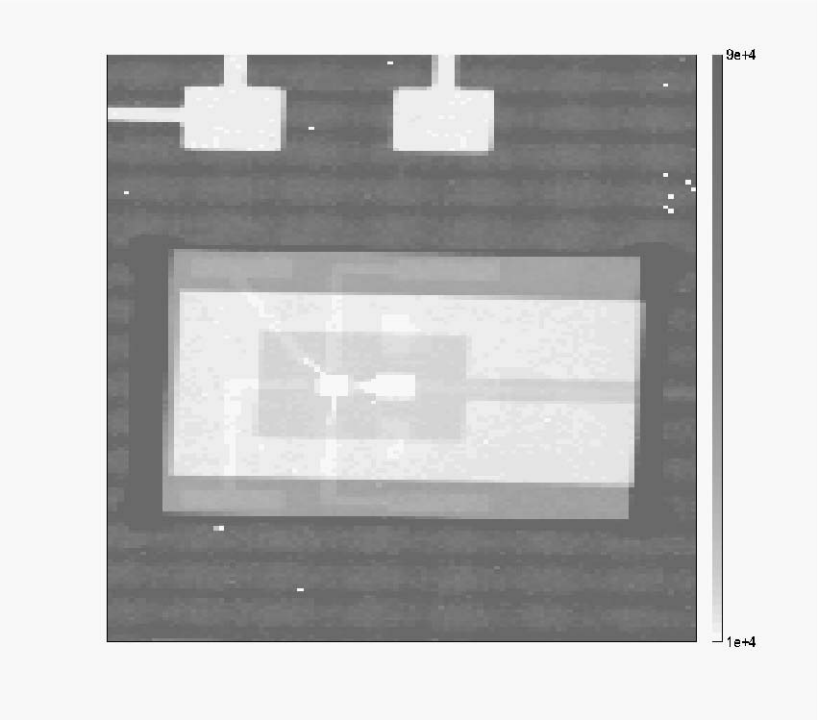

Figure 5.20: Image of an encapsulated laser diode obtained with a Medipix2-silicon assembly of 300 μm thickness. A 20 kV W-tube was used, and a flat field correction applied [42].

5.7 Conclusions

The design characteristics of the Medipix2 detector are examined, with special focus on the improvements with respect to its predecessor, the Medipix1 chip.

The components of a typical Medipix2 setup (detector - chipboard - Muros2 interface - PC with NI card - software) are described. The setup demonstrates to be reliable and stable.

The Medipix2 on-wafer testing procedure, carried out at NIKHEF, is also described. A large sample of data has been collected via wafer probing. The first production runs of the Medipix2 presented a very low yield of good chips, with typical values of 10%-20%. A problem in the manufacturing process has been identified. Correction of the production procedure resulted in a sharp increase in the yield (reaching typical values of about 80%).

The Medipix2 features and testing procedures discussed in this chapter refer to single chip assemblies. In the next chapter, the tiling of several chips into a large area detector will be described.

Chapter 6

A tiled array of Medipix2 chips for X-ray imaging

In order to increase the maximum sensitive area of Medipix2 detectors, a prototype multi-chip hybrid has been developed. The prototype combines eight Medipix2 chips onto a single large silicon sensor. The total sensitive area becomes 28 × 56 mm^2. This multi chip hybrid is mounted on a dedicated chipboard realized with a new Chip-On-Board (COB) technology called *multi-layer build up with staggered micro-vias*.

The Medipix2 2 × 4 chipboard is described in this chapter, and results obtained with multi-chip assemblies are reported.

6.1 Size limitations of an hybrid pixel detector

The maximum size of a semiconductor sensor is limited by the maximum wafer diameter obtainable. Status-of-the-art technology allows manufacturing of high-resistivity silicon ingots of 150 mm diameter, while the maximum diameter for crystals of high-Z materials like GaAs and Cd(Zn)Te is considerably smaller.

The maximum practical size of a CMOS chip, however, is much smaller. CMOS ASICs are produced on 200 mm (or even 300 mm) diameter, low-resistivity silicon wafers with an epitaxially deposited, high-resistivity layer. The maximum chip size is restricted to about 25 × 25 mm^2, due to the reticle size of the wafer stepper. This constitutes the main limitation for large-area applications of hybrid pixel detectors.

There exists techniques to produce larger CMOS chips by connecting several adjacent chips on a wafer (by overlapped exposure of the mask during the wafer stepping - the so-called *stitching*). However, these processes are non-standard, expensive and, most importantly, the yield is inversely proportional to the chip area, due to the density of point defects and other contaminations.

Nonetheless, for many applications it is desirable to have a large sensitive area. As an example, for diagnostic purposes in radiology, amorphous silicon

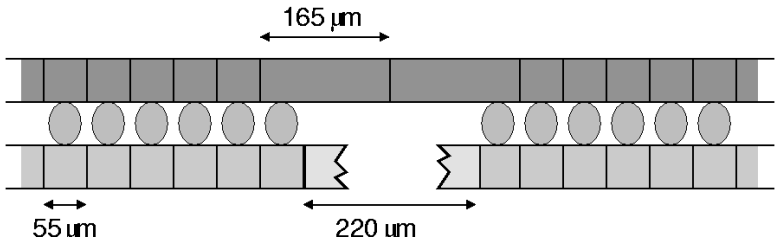

Figure 6.1: Two neighbouring chips in an array are spaced by 220 µm (4 pixels distance). The length of the sensor diodes corresponding to the cells at the chip boundary is increased to 165 µm (three times a standard pixel length of 55 µm). There is no dead area. However, because of this difference in pixel size, a slight non-uniformity is introduced near the boundary between two adjacent chips. This non-uniformity can be partly corrected for by software.

thin film arrays have been developed with a size of up to 40 × 40 cm^2 and have led to clinical applications [43]. Such detectors, with 20 × 20 cm^2 sensitive area, are used for angiography (dynamic imaging at 25 frames/sec). However, noise level, dynamic range, resolution and sensitivity in such applications could be considerably improved with hybrid pixel technology.

In the case of the Medipix2 detector, the strategy for arriving at large sensitive areas is that of tiling together multiple electronics chips, all of which are then bump-bonded to the same large semiconductor sensor. Dead area between neighbouring chips is avoided because the readout cells at the chip boundary are connected to larger sensor diodes, which have the same width as a standard pixel (55 µm) but are three times longer (see fig. 6.1). This, in turn, introduces a non-uniformity in resolution and a higher count rate along the border between neighbouring chips.

A completely uniform sensor device can be obtained by introducing a pitch adapting structure between sensor and ASIC. This approach has not yet been followed for Medipix2 detectors because of the high manufacturing costs. Moreover, non-uniformity along chip borders is not critical in our applications.

Multi-chip hybrids, also called ladders, can then be tiled into an even larger sensitive area. Dead regions then become unavoidable mainly due to the presence of guard-ring structures on the semiconductor sensor. However, new developments in 3D detectors [44] and active edge planar sensors [45] may enable a future reduction of the dead area from sensor tiling to a few tens of micrometers.

6.2 Pixel detector array systems

Table 6.1 provides an overview of devices that are based on a hybrid pixel array structure.

The Medipix2 pixel density is very high due to its small pixel size. This requires a reliable interconnection technique between sensor and chips. To solve

System	Pixel size [μm^2]	Circuit size [mm^2]	Sens. area [mm^2]	Chips/ sensor	Pixels/ circuit	Total pixels
Omega3/ LHC1	50 × 500	6.4 × 8.0	307	1 × 6	2048	12 10^3
Alladin RAL-UK	150 × 150	9.6 × 9.6	645	1 × 7	4096	29 10^3
Pilatus PSI	217 × 217	9.8 × 19.2	2707	2 × 8	57462	919 10^3
Atlas CERN	50 × 400	7.2 × 8.0	990	2 × 8	2880	47 10^3
LHCb CERN	50 × 425	12.8 × 13.6	984	1 × 7	8192	57 10^3
Medipix2	55 × 55	14.1 × 14.1	1590	2 × 4	65536	524 10^3

Table 6.1: A selection of tiled hybrid pixel detectors. Note that the Medipix2 system has smaller pixel size and a total number of bump-bonds roughly one order of magnitude higher than most other systems. The Alladin *and* Pilatus *arrays have uniform pixel size due to pitch adapting in one direction.*

this problem, a chipboard in advanced High-Density Interconnect (HDI) technology called *multi-layer build-up with staggered micro-vias* has been made. This chipboard provides mechanical support and electrical connections for a 2×4 Medipix2 array.

6.3 Medipix2 interconnectivity

As explained in Chapter 5, the Medipix2 chip uses serial, high speed LVDS logic for setting the configuration register of the entire pixel matrix and the values of the 13 DACs. Readout can be performed either serially through LVDS lines or in parallel by using a 32-bit parallel, single ended CMOS bus.

The system presented here implements the serial option (see fig. 6.2). The Medipix2 chips are arranged in a serial daisy chain with a token passing protocol. Each chip in the array is connected to either one or two neighbours. During readout, the first chip receives the readout token (via the *ENABLE_IN* line) and its shift registers sends out the data ($256 \times 256 \times 14 = 917504$ bits). After these 917504 clock pulses, the $ENABLE\_OUT_{chip1}$ line goes low. Since this line is connected to the *ENABLE_IN* input of the second chip in the daisy chain, the data from the second chip are read out. The token is passed on until the data from all the chips are collected.

There are three LVDS lines: DATA, CLK and the enable token. The nominal maximum CLK speed is 160 Mhz. A common single ended CMOS bus is used for other signals, both digital (shutter, mode control, reset, polarity, parallel/serial readout switch) and analog (DAC biases, pixel test input and DAC test output

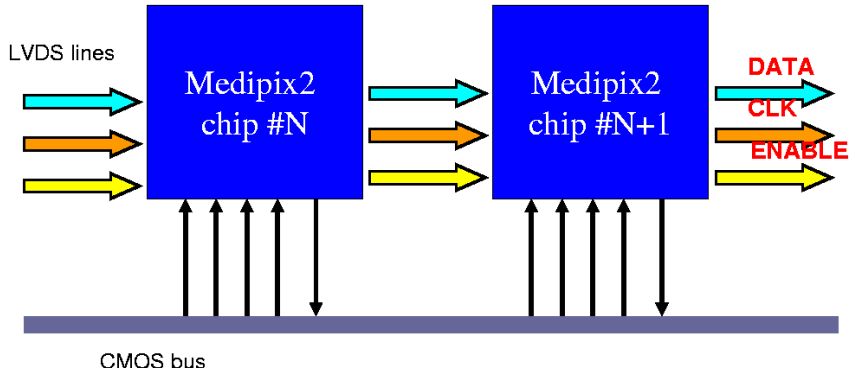

Figure 6.2: Medipix2 serial daisy chain, showing the three fast LVDS lines (data, clock and enable token) and a single-ended (slower) CMOS bus used for other signals (shutter, polarity, test input etc.).

from the chip).

Since a single-chip image is approximately equal to 1 Mbit (917504 bits), it follows that, with an operational clock speed of 160 Mhz, a total rate of 160/number of chips frames per second can be achieved.

Serial LVDS has been chosen over the parallel readout because of several reasons. Parallel readout offers in principle a higher readout speed. In the Medipix2 case, since 32 lines are available, the matrix is read out 32 times more quickly than in the serial case. However, parallel readout implies an increase in the amount of interconnectivity, in a system where the density of connections is already extremely high. The required density will be beyond the current capability of commercial chipboard manufacturers. Serial readout minimizes the amount of interconnectivity. At the same time, a high frame acquisition rate is achieved through LVDS transmission, which allows the system to reach the operating clock speed of 160 Mhz. This speed cannot be attained single-ended CMOS with a rail-to-rail swing (V_{dd}=2.2V).

6.4 The 2×4 Medipix2 chipboard in build-up technology

The chipboard is based on laminated build-up technology [46]. Typically, a thin foil (for instance kapton, or epoxy) is glued upon a substrate and then holes are etched into it. Copper is deposited by sputtering and a first layer is formed. Then a second foil is deposited on top of this layer, holes are etched and again a layer of copper is sputtered. By repeating this procedure several times an interconnected multi-layer structure is obtained. The copper that enters the holes forms contacts called *vias* (in this particular case, *staggered microvias*) between tracks in the adjacent layers.

Other connections, named *through vias*, are drilled through the full thickness of the board once the multi-layer structure has been completed, and then metalized on the inside to provide contact with the inner and outer metal layers, where appropriate. An example of build-up technology (not specific to the Medipix2 case) is shown in fig. 6.3.

6.4.1 The 2 × 4 chipboard design

The design of the Medipix2 2 × 4 chipboard was carried out at NIKHEF. Production was carried out by an industrial partner [47].

A 10-layer symmetric design has been chosen. The four central layers are realized in standard printed-wire-board technology and are organized as two double-sided layers. On both sides of this substrate, three build-up layers are made, and in this way a symmetrical structure is obtained (see fig. 6.4).

A symmetric design provides the best mechanical stability. By putting power planes and bus lines symmetrically with respect to the central plane, the heat load will also be symmetrical. Thus, the mechanical stress corresponding to thermal dilatation/contraction are more balanced with respect to a non-symmetrical design. Details about the layer structure of this board are given in table 6.2.

The built-up layers are made with epoxy foils, and micro-vias are realized through laser drilling. Connections between the two symmetrical sets of built-up layers are made with buried through-vias. The central layers host the power planes (digital, analog and LVDS power supplies and ground), while the built-up layers contain the LVDS lines and the CMOS bus. The chipboard contains 620 through-vias and 4348 micro-vias, about 2000 of which are not electrical connections and are used to improve thermal conduction. The layer structure of the board is shown in fig. 6.4. Vias and track size is given in table 6.3.

Pixel hybrids are die-bonded on the chipboard using conductive thermoplast sheets. Electrical connections between chips and chipboard are established with standard wire-bonds. To reduce noise, power lines are kept close to the

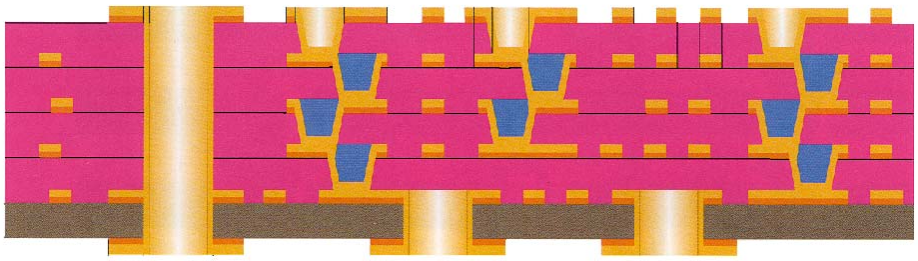

Figure 6.3: An example of high-density interconnect with build-up technology [46].

3 build-up layers: 12 μm Cu 50 μm epoxy	Layer 1: 100Ω LVDS dual tracks layer 1,2: GND Layer 3: 50Ω tracks CMOS bus
4 PCB layers: 70 μm Cu 350 μm epoxy	Layer 4: VDDA Layer 5: VDDLVDS Layer 6: VDD Layer 7: GND
3 build-up layers: 12 μm Cu 50 μm epoxy	Layer 8: 50Ω tracks CMOS bus Layer 9: 50Ω tracks CMOS bus Layer 10: decoupling

Table 6.2: Multi layer structure of the Medipix2 2×4 chipboard

Structure	Width [μm]
CMOS tracks	100
LVDS tracks	100
Micro-via	100-150
Through-via	500-650

Table 6.3: Via and track sizes in the 2×4 Medipix2 chipboard, showing relaxed technology parameters to increase the yield.

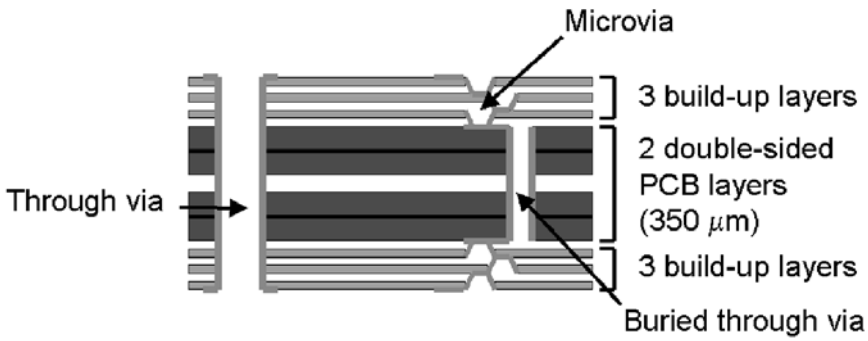

Figure 6.4: Layer structure of the 2×4 Medipix2 chipboard. A symmetrical structure has been adopted. The build-up layers are based on an epoxy foil, and the vias are made with laser drilling.

chip so that the corresponding wirebonds remain short. This minimizes their impedance. In addition, decoupling capacitors have been mounted at close distance on the backside through via holes. The LVDS lines are further away from the chip since they are less sensitive to the noise. To avoid reflections, the LVDS lines are terminated with 100 Ω impedance.

In addition to the decoupling capacitors, one analog FET multiplexer switch per chip is mounted. Its purpose is to provide analog test input pulses to all pixels. The amplitude of the pulse is determined by the voltage difference between two lines from the Muros2 interface.

The chipboard is mounted in an aluminum frame for handling and cooling. A thin beryllium foil protects the hybrid from light and moisture. A cooling system can be mounted on the backside. A Peltier cooler can be mounted on the backside and keeps the detector at room temperature (or slightly below). The power dissipation of an 8-chip setup is about 6-8 W.

6.5 Current status

To date, 16 boards have been produced by [47] with a yield of 100%.

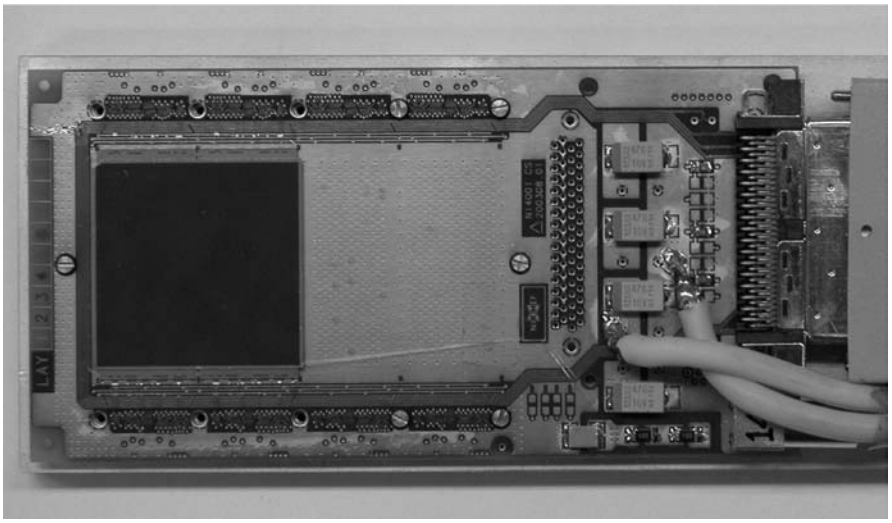

*Figure 6.5: View of the Medipix2 2 × 4 chipboard. A 2 × 2 detector (*quad*) is mounted on the board. A second 2 × 2 detector can also be added.*

Test have been done with the 2 × 4 carrier board, replacing the chips with simple shorted wires. Clock rates of 200 Mhz were achieved without loss of any data bits (bit error rate $< 10^{-12}$). This shows that the bandwidth of the boards exceeds the chip clock speed.

Several Medipix2 detector arrays have been mounted on the chipboard pro-

totypes and tested with success (see fig. 6.5). These detectors are 2 × 2 chips systems with a 300 μm thick silicon X-ray sensor (28 × 28 mm^2), and are referred to as *quads*. Fig. 6.6 is an example of a large-area image collected with a Medipix2 2 × 2 system.

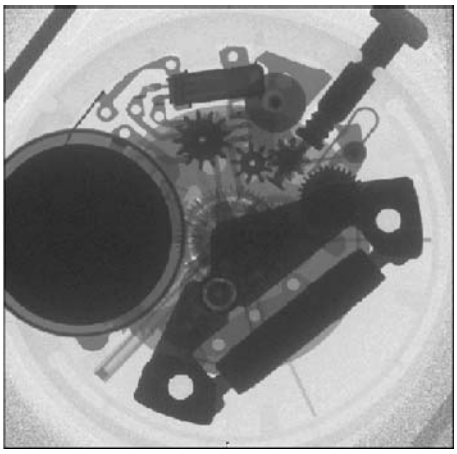

Figure 6.6: Image of a watch, taken with a Medipix2 2 × 2 array (quad)*. The image size is 28 × 28 mm^2. Each wider pixel at the chips boundaries has been software interpolated into three normal size pixels.*

6.6 Conclusions

A system for tiling up to 8 Medipix2 chips into a large area detector array has been developed. The most important and innovative element in the system is the 2×4 Medipix2 chipboard. Realized in High Density Interconnect technology, this carrier can host up to a maximum of 8 chips connected to a large area semiconductor X-ray sensor. The board provides mechanical support for the chips, as well as interconnections with the readout system. A thermoelectric cooling system can be easily added on the backside of the board.

Prototype boards have been produced with 100% yield providing excellent X-ray images with 2×2 Medipix2 detectors. This demonstrates the proper functioning of the Medipix2 chipboard, and proves that a tiled array of hybrid pixel chips is a successful approach toward large area X-ray imaging.

Chapter 7

The readout of a gas detector with the Medipix2 chip

The Medipix2 chip has been designed to connect to a semiconductor sensor for X-ray detection. However, a completely different application is presented here. Returning to high energy physics, the Medipix2 chip is used to read out signals from charged particles in a detection system based on a gas ionization chamber.

The goal is to construct a high granularity, high resolution *Time Projection Chamber* for application in experiments at the future high energy electron-positron collider, the ILC (*International Linear Collider*).

A brief introduction to gas tracking devices is given, subsequently the development of a prototype TPC with pixel readout is described.

7.1 Collider experiments

In high energy physics experiments, tracking systems are needed to reconstruct trajectories of charged particles. Usually, they are positioned as close as possible to the interaction point. Thus, a typical tracking detector is operating in an environment with high rate and high track-multiplicities. The main requirements are the following:

- Very good granularity
- Sufficient radiation hardness

During the past 40 years, several tracking techniques have been developed. Today, semiconductor trackers are the state-of-the-art technique for operation in high flux, high track density experiments.

In the following sections, a quick overview on gas detectors used for tracking in high energy physics is given. Then we present what we believe is an interesting evolution for the readout of these devices.

7.2 Gas Filled detectors

Until 1970, all the tracking detectors were optical in nature: photographic emulsions, bubble chambers, cloud chambers, etc. All these technologies required the recording of the track information on film. The film was then later examined offline frame by frame for interesting events.

Detectors based on gas ionization were the first electronics devices for radiation detection, and have always been widely used for charged particle tracking in high energy physics experiments.

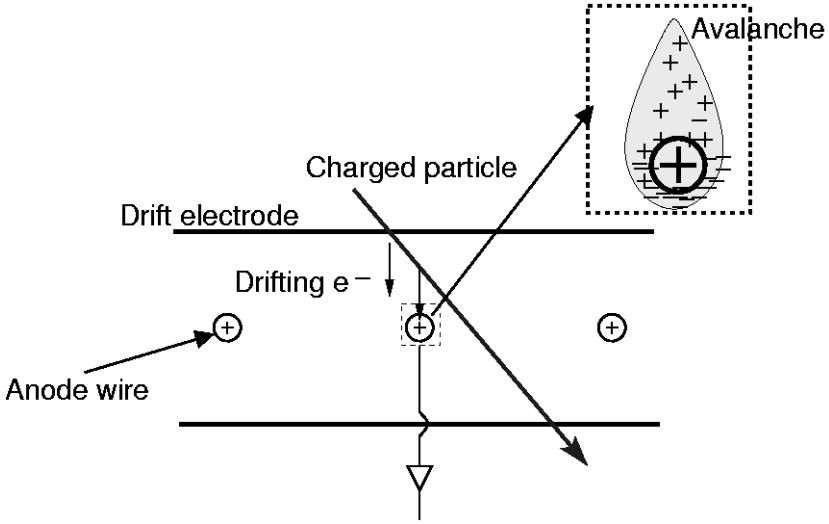

Figure 7.1: Typical layout of a multi-wire proportional chamber. The cathode planes enclose a set of anode wires (perpendicular to the plane of view). When a drifting primary electron is close to an anode wire, an avalanche develops. The charge is collected at the anode wire.

7.2.1 Multi-wire proportional chambers

One of the first gas filled tracking chambers was the *Multi Wire Proportional Chamber* (MWPC) [48]. In this device a set of parallel thin anode wires is put in between two cathode planes (see fig. 7.1). Typical wire spacing is 2 mm with an anode-cathode gap of 7-8 mm. A voltage is applied across the cathode planes and the anode wires. Except for the region very close to the

anode wires, the field lines are essentially parallel and almost uniform. Great care must be taken in the positioning and alignment of the wires, since even a small wire displacement can drastically modify the field lines, the drift path and acceleration of the electrons.

This system is contained in a chamber filled with (a mixture of) gas. Charged particles entering the chamber create electron/ion pairs through ionization of the gas molecules. The (*primary*) electrons drift toward the anode wires, while the remaining ions migrate toward the cathode plane.

In the high electric field close to the anode, the primary electrons liberate *secondary* electrons and an *avalanche* or *multiplication* effect develops (fig. 7.2). The avalanche charge is proportional to the number of primary electrons released. Typical values for the *gas multiplication* (or *gas gain*) are of order 10^3-10^7.

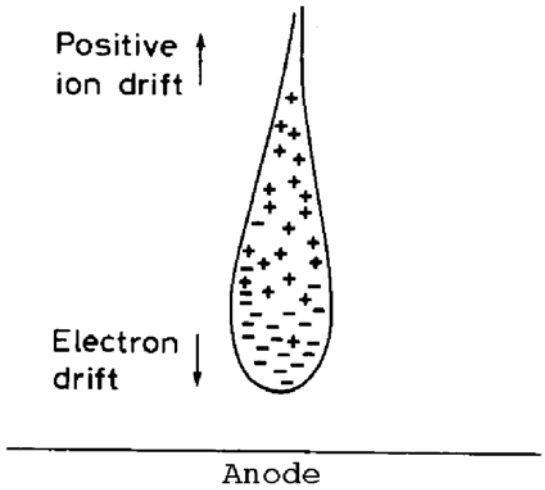

Figure 7.2: Formation of a charge avalanche in a gas detector. Since the electrons are more mobile than the positive ions, the avalanche takes the form of a liquid drop with the electrons at the lead.

Electrons are collected at the local anode wire, causing a negative pulse. The positive ions liberated in the multiplication process induce a positive signal on the wire close to which the avalanche appeared. Shortly after the avalanche, the negative electron charge is almost completely compensated by the induced ion charge and the net charge on the wire is small. The negative wire charge appears as the ions migrate toward the cathode. The neighbouring wires are also affected: however, the signals induced on these wires are positive and their amplitude is smaller. Similarly, a positive signal is induced on the cathode plane. There will be no ambiguity as to which wire is closest to the traversing

charge. We note that the signal is mainly induced by the ions, while the electrons contribute to about only 1% of the signal. This is because the majority of the ions, due to the avalanche mechanism, are produced very close to the anode wire. Thus, the electrons travel only a small distance before being collected at the anode, while the ions travel a longer distance towards the cathode, and so induce the majority of the signal.

The spatial resolution of a MWPC depends on the spacing of the anode wires, and it is equal to half of this value. For a typical wire pitch of 2 mm, therefore, the spatial resolution becomes 1 mm. Thus, the wire pitch determines the granularity of the detector. The maximum counting rate for these devices is about 10^4/s-mm per wire, due to space-charge build-up limits in the avalanche region.

7.2.2 Drift chambers

Fig. 7.3 shows further development of the MWPC. The drift time of the charge over large distances can be determined and gives additional space-point information. This type of detector is called *drift chamber* [49].

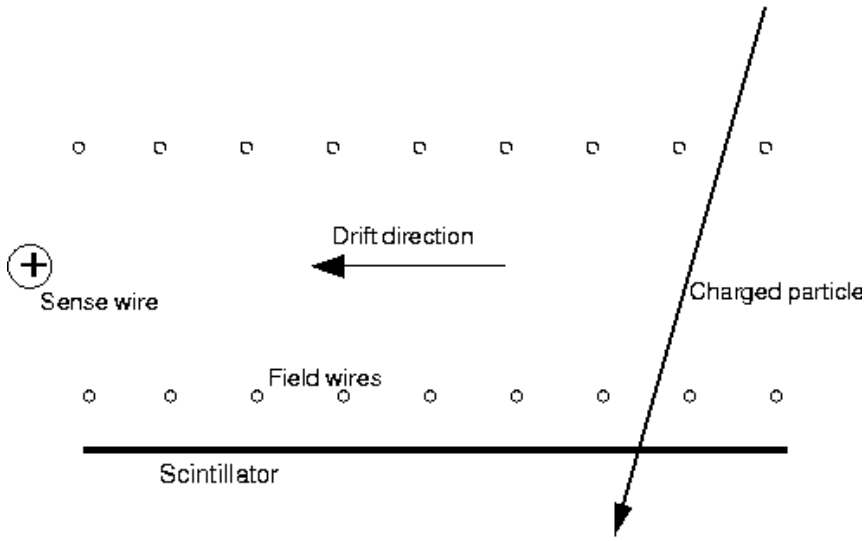

Figure 7.3: In a drift chamber, the arrival time t_1 of the avalanche caused by a primary electron is measured. Usually the charged particle crossed a trigger device (scintillation counter) providing t_0. The drift time $t_1 - t_0$ is easily calculated, and the track position can be reconstructed.

It is highly desirable to have a constant and uniform drift field. In this way, the drift velocity is constant and a simple linear relationship between time measured and distance traveled by the primary electrons is achieved. For this

reason, cathode field wires are employed in addition to anode sense wires.

The drift time of the electrons from an ionizing event is calculated in the following way: $t = t_1 - t_0$, where t_0 is the arrival time of the particle as measured by for instance a scintillation counter, and t_1 is the time at which the pulse appears at the anode.

Usual drift lengths are about 5-10 cm (but drift paths up to 50 cm have been achieved). Many adjacent drift cells can be combined to cover large detection areas. Since typical drift velocities are of the order of 5 cm/μs, it follows that common drift times are of the order of 1 - 2 μs (this is also known as the *memory time* of the chamber). Wire spacing is larger than in MWPCs.

The main advantages of a drift chamber over a multi-wire proportional chamber are the smaller number of wires and electronics required, the larger detection areas achievable and the better spatial resolution. However, greater care must be taken with the field uniformity. Since the density of wires in a drift chamber is smaller than in an MWPC, the maximum particle rate also become smaller. For a drift length of 5 cm, resolutions of 200 μm can be obtained.

7.2.3 Time projection chambers

A natural evolution of the drift chamber is the *Time Projection Chamber*, or TPC [50, 51] (see fig. 7.4).

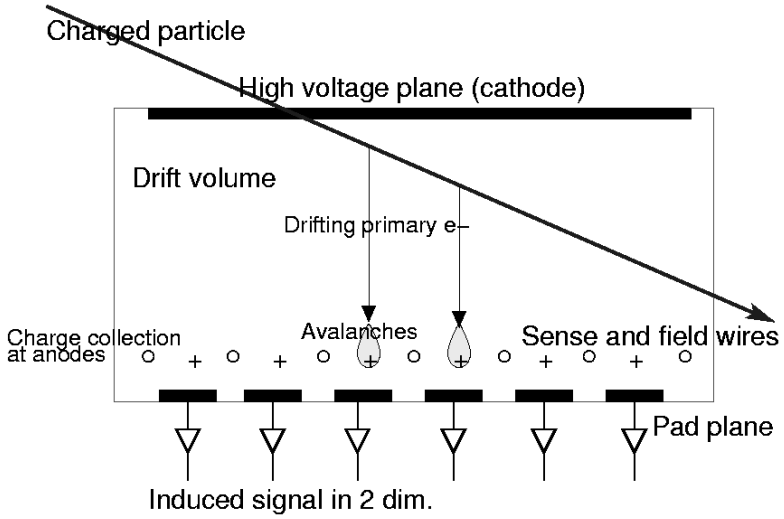

Figure 7.4: Schematic view of a Time Projection Chamber. The field cage creates a homogeneous electric field. Primary electrons drift toward the sense anode wires, and the resulting avalanche is read by the pads, in two dimensions. The third coordinate is obtained by measuring the drift time of the electrons.

A TPC consists of a gas filled drift space in which a homogeneous electric field is created between a cathode plane and a set of anode wires. The primary electrons drift toward the wires, where a charge avalanche is produced. A set of cathode pads is placed behind the anode wires: the charge avalanche induces a signal on the pads, and thus its position is measured in two dimensions. The third coordinate is determined by measuring the drift time of the primary electrons along the electric field (as in a drift chamber). Thus, a TPC enables a true 3-dimensional reconstruction of the track position and curvature.

Because of the relatively long drift distance (up to 2 meters), lateral diffusion of the primary electrons may become a serious problem. For instance, for Ar/Isob. 75/25 and a drift path of 1 m, the width of the diffusion distribution is about 2 mm. The width scales as the square root of the drift path. A common solution is to create a magnetic field in the drift volume, parallel to the electric field[1]. This may reduce the diffusion by as much as a factor of 10. However, the alignment of the electric and magnetic field must be accurate down to about 1 in 10^4.

Typical pad sizes are of the order of 1 cm^2, and provide a resolution within 300-500 μm thanks to interpolation on the induced signals. The important advantage of using a TPC is that 3-dimensional space points are obtained.

7.2.4 Recent improvements: gas-filled chambers without wires

Recently, several gas detectors without sense or field shaping wires were designed.

The Micromegas (Micro Mesh Gaseous Structure) [52] uses a nickel or copper foil of thickness 5-15 μm (fig. 7.5). By etching, tiny holes are made. The foil is then placed parallel to the pad anode plane, and fixed at a distance of 50 μm with insulating spacers. A voltage (300-500 V) is applied across the Micromegas and anode plane. This electrical field allows the multiplication mechanism in the gap between foil and readout pads. In this way a primary electron reaching the Micromegas causes an avalanche in the gap between the foil and the anode plane. The charge is then collected by the anode pads. Thus, Micromegas replaces the anode wires.

Alternatively, another innovation replacing the anode wire plane is the *Gas Electron Multiplier* (GEM) foil [53]. A GEM consists of a 50 μm thick insulating kapton foil. Thin copper layers (about 5 μm thick) are deposited on both sides of the foil, and holes are etched into the copper by photolitography. Special care is taken in aligning the holes of the two copper layers, since they have to match accurately. The structure is then exposed to a liquid that dissolves the kapton but leaves copper unaffected, leaving (gas-filled) tubes in the foil. An electron microscope view of a GEM foil is shown in fig. 7.6.

A voltage (about 400 V) is applied across the two copper layers. A primary

[1] This magnetic field is required to measure the momentum of the particles. As a side effect, it also reduces lateral diffusion

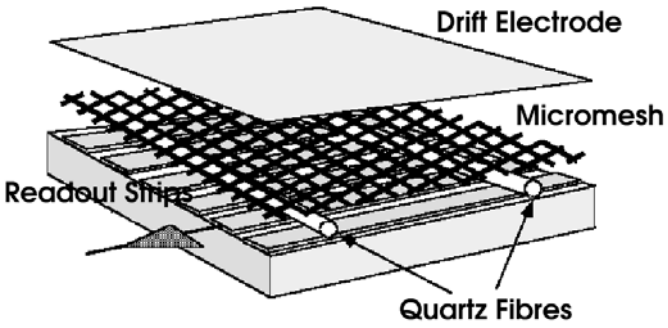

Figure 7.5: Schematic view of a gas detector with a Micromegas plane.

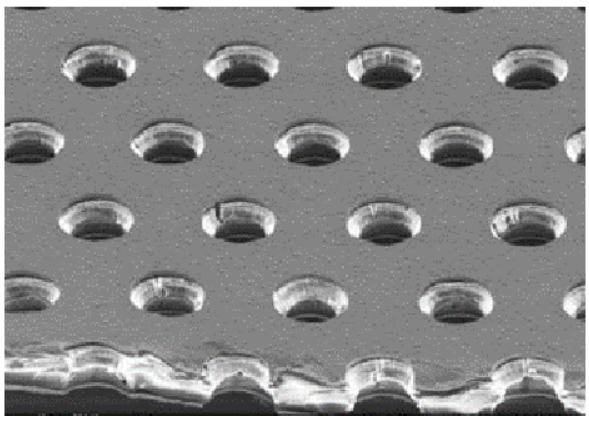

Figure 7.6: Electron microscope view of a GEM foil. The diameter and pitch of the holes are 70 and 140 μm, respectively.

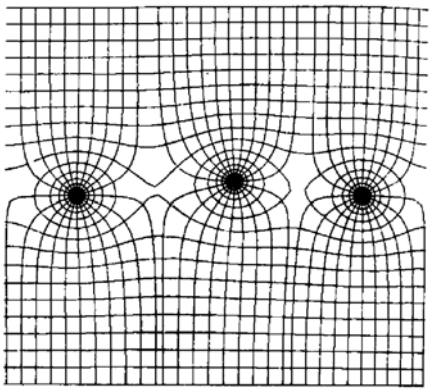

Figure 7.7: A slight displacement of a wire in a multi-wire proportional chamber may result in severe distortions of the electric field.

electron reaching the GEM causes an avalanche inside one of the tubes. The electrons then drift toward the anode pads.

The GEM foil and the Micromegas are often referred to as *gas gain grids*. They completely replace the anode wire plane.

There are several advantages in replacing a wire system with a gas gain grid. A better granularity is achieved, since the minimum possible wire spacing severely limits the number of readout channels. In addition, wires are extremely delicate structures and can be easily damaged by mechanical handling, electrostatic forces and accidental sparks. Furthermore, a constant stretching force must be kept to avoid the bending of the wires due to gravitational and electrostatic forces, resulting in worse spatial resolution. Less material is needed since there is no wire support. Moreover, the delicate wires have to be accurately aligned. Displacement may induce large inhomogeneities in the drift field (fig. 7.7).

7.3 A semiconductor readout for a gas detector

In this section we present the various aspects (objectives, ideas, results and future projects) of the application of the Medipix2 chip as readout system for a gas-filled tracking chamber.

7.3.1 Readout using a CMOS chip

Independently of whether anode wires or a gas gain grid is used, TPCs have a readout based on metal pads. Each pad (typical areas of the order of 10 - 50 mm^2) has a feedthrough and is connected to external readout circuitry.

We propose a new approach, with two important features:

- Replacement of the readout system by a single element: a CMOS chip that can detect the cloud of avalanche electrons and process this signal. The avalanche charge is collected at small pads integrated on the readout chip.

- Integration of the gas gain grid on the chip through a post-processing procedure.

This will lead to:

- Reduction in pad size (about 100×100 μm^2). The number of readout channels will become extremely high: about 10^9 for a large TPC. This provides excellent granularity and low hit occupancy.

- Simplified mechanics since the wires are removed and the grid is introduced by post-processing of the readout chip. The readout system becomes very compact. In addition, mass production of the chips will reduce the cost of a high-granularity TPC.

- Detection of single primary electrons due to improved resolution, instead of determining the center of gravity of a cloud of about 30 electrons. This, in turn, offers several improvements over the more conventional technology:

  - Best possible TPC performance in terms of spatial resolution due to the precise measurement of the space coordinates of each single primary electron;
  - Possibility to measure the energy loss per unit length (dE/dx) by measuring the number of clusters (and electrons) per unit length. Information about dE/dx can be used can be used for particle identification;
  - The effect of δ-rays[2] can be eliminated. As individual primary electrons can be detected, the cluster of primary electrons left by the δ-ray can be recognized and excluded from the track fit.

7.3.2 Readout implementation with the Medipix2 chip

Two different prototype pixel TPCs have been designed based on the Medipix2 readout. Although not designed for this purpose, we demonstrate that the concept may outperform the classical TPC.

The first prototype uses a triple GEM foil system, while in the second a Micromegas mesh is applied. Both setups are examined in the following sections.

[2] δ-rays are energetic secondary electrons leaving electron clouds not correlated to the original track, and which may cause a systematic error in the track position measurement.

7.4 The GEM/Medipix2 TPC

The first prototype consists of a gas multiplication system made by a stack of three GEM foils (see fig. 7.8). With a three-foils combination, higher gains are achieved since the avalanche effects of the individual foils are combined in a cascade.

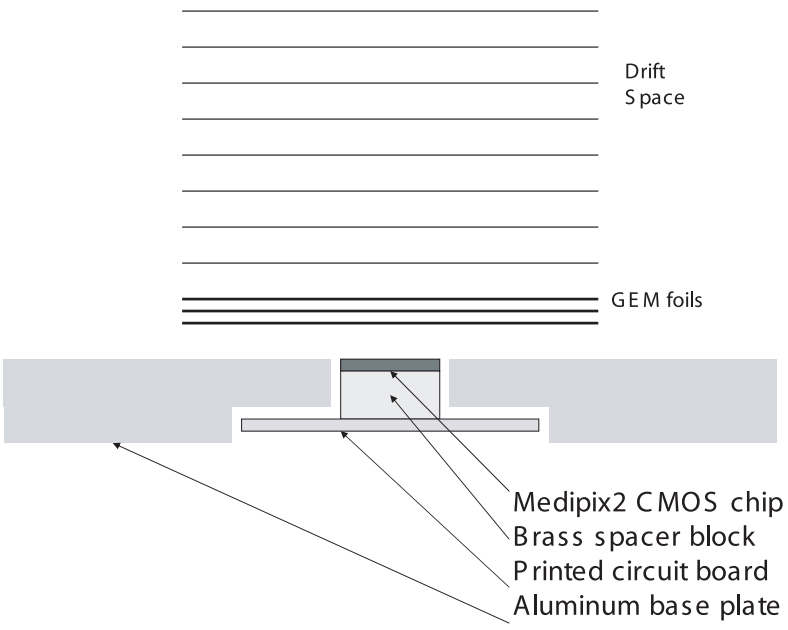

Figure 7.8: Schematic view of the GEM/Medipix2 setup. An electric field (about 100V/cm) is generated in the drift region. Below the drift space, a stack of three GEMs provides gas gains up to 4×10^4. Avalanches are detected by a Medipix2 chip inserted in the aluminum base plate.

The drift volume measures $100 \times 100 \times 100$ mm^3. The low electric field is generated by electrodes, in the form of square wire loops, put at linearly decreasing potential. In the corner of the wire loops, insulating pillars (positioned outside the drift volume) support the loops. The distance between the loops is 6.25 mm; the GEMs are 1.6 mm apart. The distance between the bottom GEM and the base plate of the chamber is 6.6 mm.

The Medipix2 chip is mounted on a standard printed circuit board, positioned in an insert in the aluminum base plate of the chamber. In this way, the chip surface is aligned with the top of the aluminum base plate. This ensures a homogeneous drift field between the bottom GEM and the Medipix2. The PCB is then connected to a PC via the Muros2 interface. A picture of the prototype

is shown in fig. 7.9.

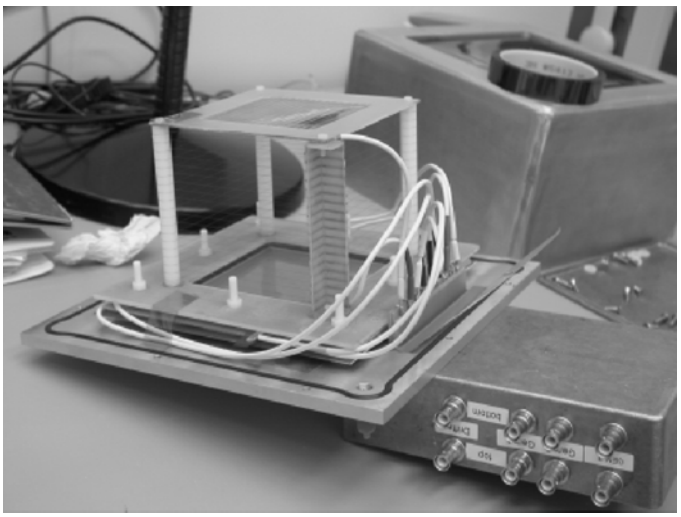

Figure 7.9: The GEM/Medipix2 prototype TPC.

The effective gas multiplication can be varied by changing the voltage across the top electrode and bottom GEM. Intermediate electrodes and GEMs are coupled via a passive network (resistors) providing a continuous potential gradient.

Different gas mixtures have been employed with this prototype chamber. Initially, an Ar/Methane 90/10 mixture was used. However, with an Ar/Isobutane 95/5 mixture much higher gains were reached (up to 4×10^4).

This high gain implies large signal easily crossing the threshold on the pixels. Note that the bond pad is now used as electron collecting pad.

Since the Medipix2 cannot provide time stamp information, and since no trigger hardware is included, the drift time measurement was ignored.

7.4.1 Results

The chamber was irradiated with X-rays from ^{55}Fe, using an Ar/Methane (90/10) gas mixture, with a gain of 1.3×10^4. An image acquired with a 5 sec. exposition time is shown in fig. 7.10). Charge clusters with a diameter of about 30 pixels (1.5 mm) are detected. Here the Medipix2 threshold is set to a very low value, and many noisy pixels are visible. This image is one of the first ever acquired with the TPC (March 2003).

More measurements have been carried out. A mixture of Ar/Isob. 95/5 (higher gain, 1.8×10^4), and β's from a ^{90}Sr source were used. Since the radioactive source was much more intense, the acquisition time was only 0.001 sec. A different Medipix2 chip, with different threshold settings and noise properties, was used. An image is shown in fig. 7.11. Large charge clusters are still visible.

These clusters are slightly wider than the ones from fig. 7.10), due to the higher gas gain.

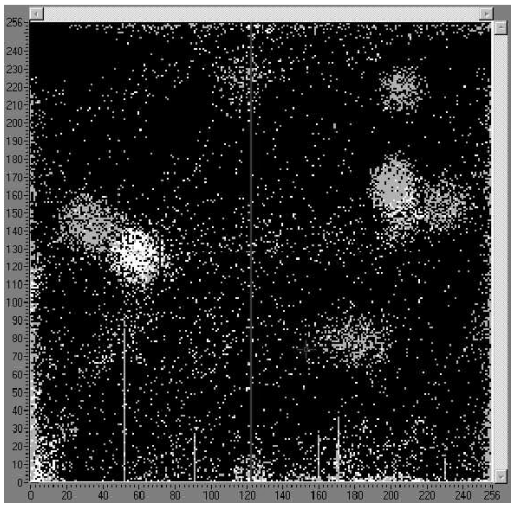

Figure 7.10: Raw image recorded with the three-GEM prototype TPC. Acquisition time was 5 seconds and an ^{55}Fe source was used. The gas is a mixture of Ar/Methane (90/10) and the gas gain is 1.3 × 10^4. The clusters are observed in the presence of the source. the black areas imply no signal, gray corresponds to a single hit and white to 2 hits.

The same setup has been used without a radioactive source to detect cosmic radiation (mainly muons). A series of 2 sec. exposures was performed. Since no trigger hardware was present, the majority of the images contained no interesting information. However, in a few cases tracks from cosmic rays are visible. A selected image is shown in fig. 7.12. Again, the charge distribution is about 30 pixels (1.5 mm) wide.

Diffusion effects due to long drift distances, in combination with de-focusing effects in GEMs as reported by other groups [54, 55], may explain the large cluster sizes in the images. Diffusion effects may be cured by operation in a magnetic field. However, due to limited availability of a magnetic field, this has not been attempted in our case. A second prototype TPC was instead developed, that is less sensitive to diffusion and de-focusing effects because:

- The drift length is considerably reduced (15 mm instead of 100 mm)

- A Micromegas is used instead of a stack of 3 GEMs

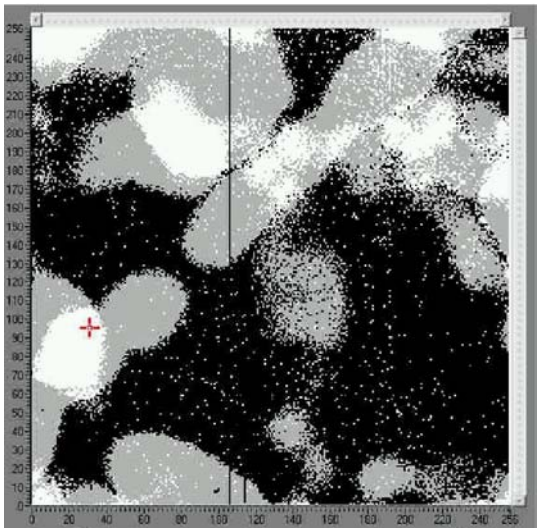

Figure 7.11: As fig. 7.10, but with Ar/Isobutane 95/5, a gain of 1.8×10^4 and 0.001 sec. acquisition time. The radioactive source employed is ^{90}Sr. Colour scheme: black = 0 hits above threshold, gray = 1 hit, white = 2 hits.

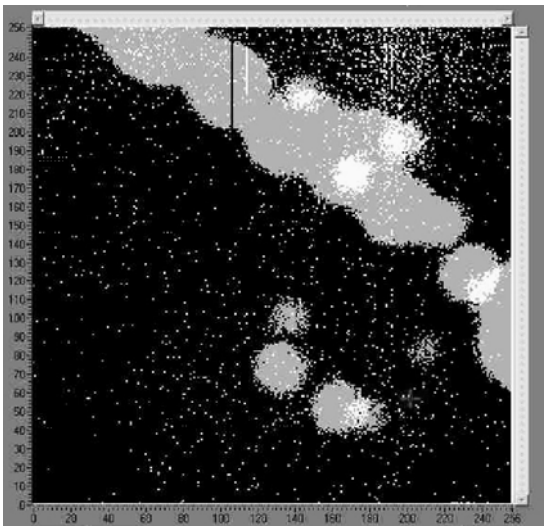

Figure 7.12: As fig. 7.10, but with Ar/Isobutane 95/5, a gain of 1.8×10^4 and 2 sec. acquisition time. No radioactive source is present. A cosmic ray track is clearly visible. Colour scheme: black = 0 hits above threshold, gray = 1 hit, white = 2 hits.

7.5 The Micromegas/Medipix2 TPC

The second prototype chamber was optimized to avoid the large charge spread met with the 3-GEM setup. A Micromegas mesh is now used, and it is positioned only 50 μm above the Medipix2 surface. A smaller drift space has also been chosen (only 15 mm, compared with 100 mm in the previous setup).

An overview of the layout is given in fig. 7.13. Above an aluminum base plate, a cathode foil is fixed, by means of spacers, forming a drift gap of 15 mm height. The Medipix2 chip is mounted on a small brass pedestal and inserted in a slot in the base plate, so that it is flush with the base upper plane. The Micromegas foil, fixed on a frame, is placed above the chip thanks to its insulating spacers, and held in position by means of two silicon rubber strings. The prototype is pictured in fig. 7.14: in a), the assembled detector is illustrated, while b) shows the support (silicon rubber stripes) for the Micromegas.

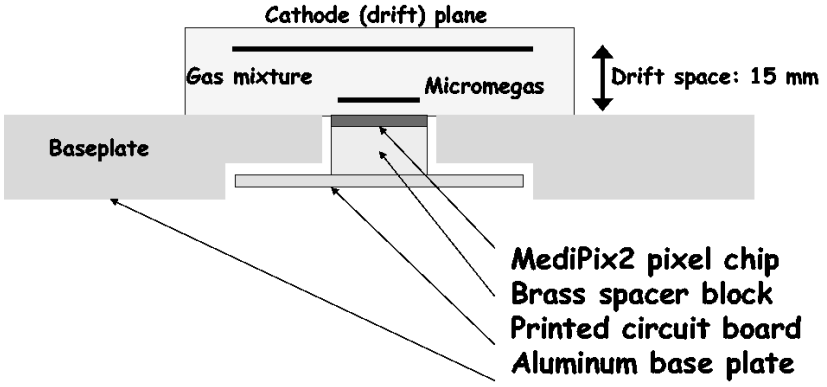

Figure 7.13: Layout of the Medipix2/Micromegas chamber.

The Micromegas that we used is a copper foil of 5 μm thickness, with 35 μm diameter holes in a square pattern with 60 μm pitch. Poly-imide pillars are attached on the side of the foil that faces the Medipix2. They have an height of 50 μm, a diameter 80-140 μm with a square pitch of 840 μm), and their function is to keep the Micromegas mesh at fixed distance (50 μm) to the anode plane (i.e., the Medipix2 chip). When the voltage on the Micromegas is applied (200-500 V), the electrostatic force pulls the mesh toward the chip, and the spacing pillars define the proper gap size.

In order to prevent HV breakdowns, a square kapton foil (with a square hole of 9×9 mm^2) has been placed between the Micromegas and the Medipix2. The drift direction is vertical. Calculations show that a charged cosmic ray particle traverses the fiducial drift volume of $9 \times 9 \times 15$ mm^3 about once per minute.

Several Medipix2 chips have been used during the tests, coupled with several identical Micromegas meshes. While some are standard Medipix2 chips, many others have been modified by means of wafer post-processing techniques to have

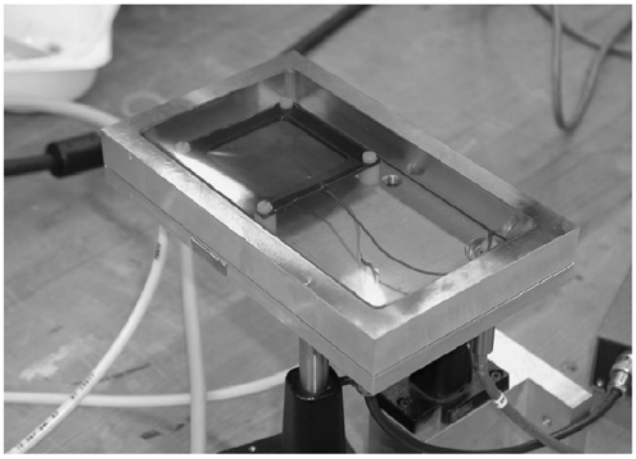

a)

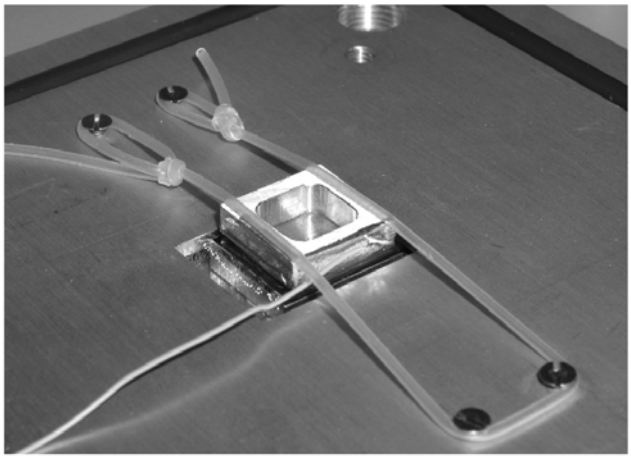

b)

Figure 7.14: a) View of the assembled Medipix2/Micromegas prototype gas chamber. b) The support for the Micromegas (silicon rubber stripes) is shown.

an increased metalized area on each pixel.

7.5.1 The post-processed Medipix2 chips

With a *lift-off* lithography process, a thin layer of aluminum (about 5 μm thick) is deposited on each pixel.

The Medipix2 pad area is of octagonal shape, with a 20 μm diameter. This covers roughly 20% of the pixel surface. The remaining surface is covered with insulating material (SiN_2). The metalization procedure increases the total metalized surface of each pixel, leaving only a 5 μm wide insulator band at the border of each cell. In fig. 7.15 the Medipix2 before (a) and after (b) post-processing is displayed.

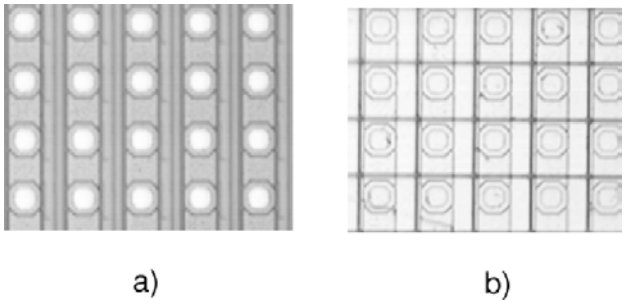

Figure 7.15: The orthogonal bonding pads on the Medipix2 chip before (a) and after (b) post-processing in which a metal layer is deposited to enlarge the charge collection area.

The increased charge collection area also avoids charge build-up in the insulating surface dielectric, improving the electric field properties in the area.

The post-processing of the Medipix 2 has been carried out at the University of Twente/MESA+. The lift-off lithography procedure includes:

- Chemical wafer cleaning; baking the wafer will ensure complete removal of the solvent.
- Application of a photoresist via spin-on.
- Exposure of the photoresist layer to UV light with a mask
- Deposition of aluminum through sputtering.
- With a lift-off mechanism, the photoresist structure still present on the chip is removed together with the aluminum that has been sputtered on top of it.
- The post-processing is completed, the wafer can be diced into chips.

The main steps of this post-processing procedure are shown in fig. 7.16.

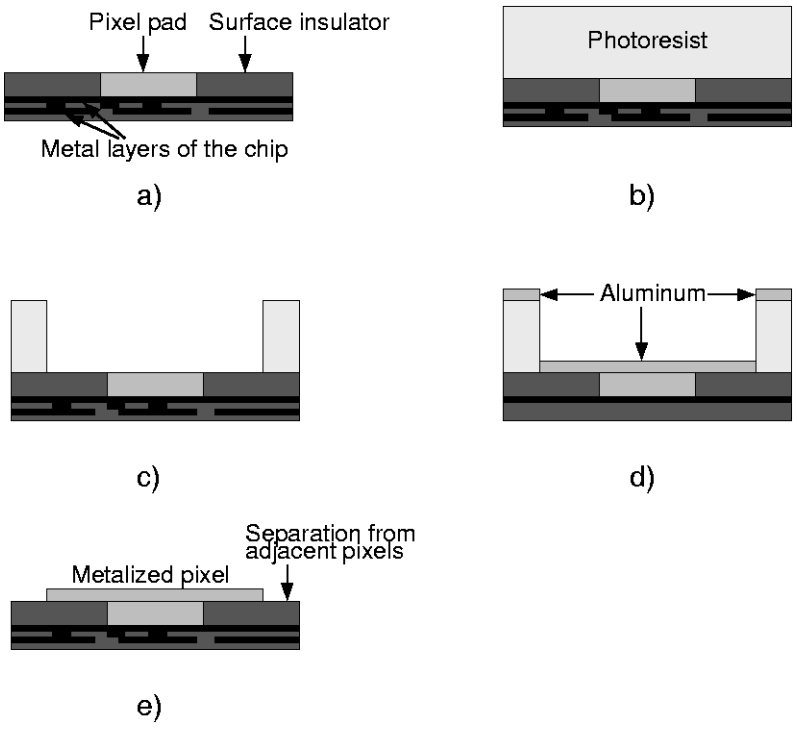

Figure 7.16: Lift-off lithography employed for the metalization of several Medipix2 chips. a) The wafer has been cleaned. b) Deposition of photoresist. c) Removal of photoresist in the areas of interest. d) Deposition of aluminum. e) Lift-off.

7.5.2 Signal development

The system has been tested with radioactive sources (^{55}Fe, ^{90}Sr, ^{241}Am) and cosmic rays (muons). The latter case is of particular interest. A cosmic muon generates clusters of primary electrons along its track when traversing the drift volume. The cluster density and distribution of the number of electrons per cluster depends on the gas composition, gas density and the muon energy deposited. If argon is the main component of the gas (at atmospheric pressure), about 3 clusters per mm are created for a minimum ionizing particle, and the average number of electrons per cluster is 2.5 [56].

The signal development proceeds as follows. After an electron has entered a hole in the Micromegas, multiplication via the avalanche mechanism occurs, with the number of electrons growing exponentially toward the anode pads. The centre-of-gravity of the electron-ion pairs is located at about 5 μm above

the anode. The electrons then arrive within 1 ns at the anode, while most of the ions arrive at the Micromegas foil within 30-50 ns, depending on the gas composition.

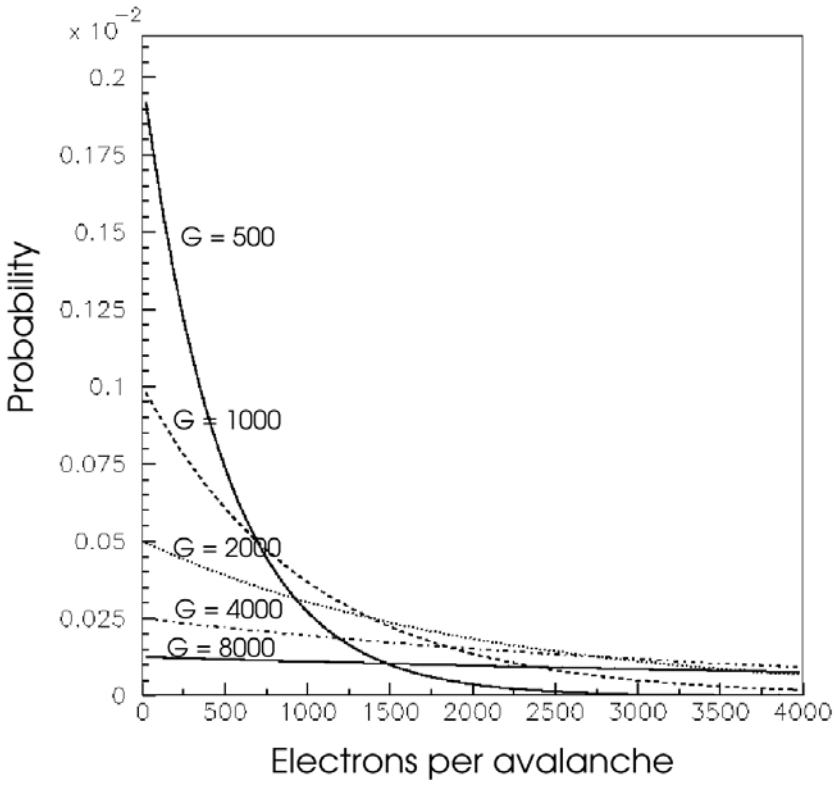

Figure 7.17: Probability of a primary e^- giving rise to an avalanche with a determined number of secondary electrons, calculated for different values of the gas gain G.

The charge on the anode pad becomes the sum of the collected negative electron charge and the induced positive ion charge. As a result, also at the pad there is a fast component to the charge build-up due to electrons and a slower contribution from ions. The fast component has an amplitude of about 10 % of the total charge; the full signal is obtained within 30-50 ns. On adjacent pixels, a small positive charge is induced, reaching a maximum after about 25 ns.

Since the peaking time constant of the Medipix2 preamplifier/shaper is 150 ns (thus large with respect to the time constant of the signal development), the output of the preamplifier is therefore proportional to the avalanche charge.

The discriminator threshold can then be related unambiguously in the number of electrons appearing at the input pad.

The probability of having an avalanche with a total of n electrons is [57]:

$$p(n) = \frac{1}{G} e^{-\frac{n}{G}} \tag{7.1}$$

where G is the gas gain. In fig. 7.17 this probability is plotted for several different values of G.

The distribution becomes less and less peaked at zero for increasing values of G. However, the probability of having an avalanche with a low number of electrons is still significant. This introduces inefficiencies when a minimum discrimination level T is applied. Thus, the efficiency to detect an avalanche signal originating from a single electron reads:

$$\epsilon = e^{-\frac{T}{G}} \tag{7.2}$$

In order to achieve an efficiency better than 50% for a minimum threshold level of 3000 e^-, a gas gain of 10^4 or higher is required.

High gas gains, though, are not desired:

- Any small discharge in the avalanches may damage the Medipix2 chip. The pixel cells are not equipped with excess current or voltage protection circuitry, and no protective layer has been applied on the pixel pads.

- The ions density in avalanche should be minimized. Although the larger part of these back-migrating ions will be neutralized at the Micromegas, the ions entering the drift volume will disturb the electric drift field.

He-based gas mixtures have been used for MIP detection, since they give a higher gain than Ar mixtures with a smaller risk of discharges.

7.5.3 Results

As a first test, the gas volume has been irradiated with several radioactive sources. ^{55}Fe clusters are shown in fig. 7.18, while an image acquired using a much more intense ^{90}Sr source is presented in fig. 7.19.

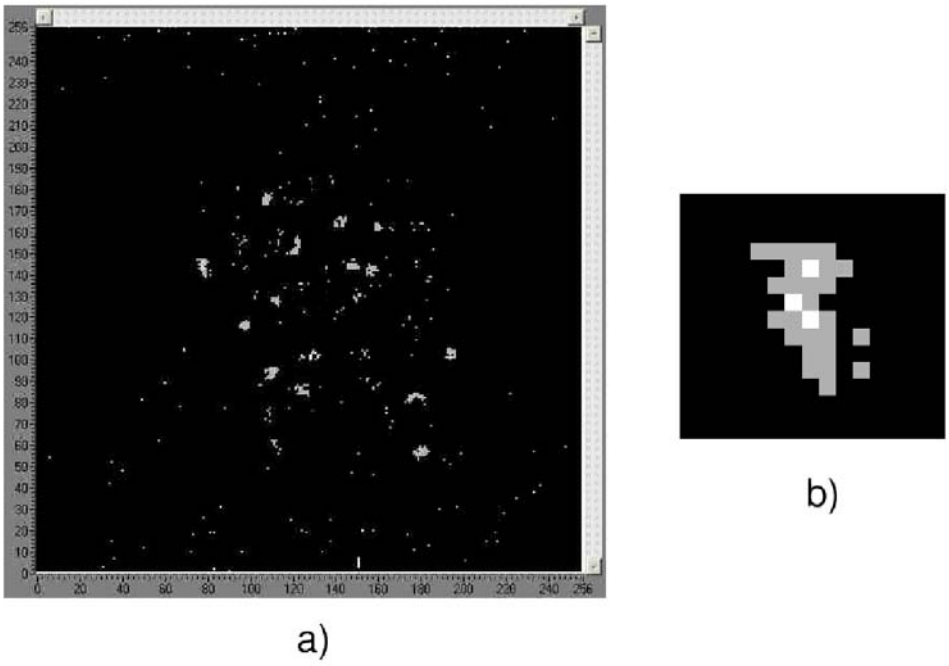

Figure 7.18: a) Raw image obtained with the Medipix2/Micromegas prototype and an ^{55}Fe source. The exposure time is 1s. The gas is an Ar/Isobutane 95/5 mixture (estimated gain of 10^4). Charge clusters are visible. b) Enlarged view of one of the clusters in a); the structure of the electrons cloud is clearly visible.

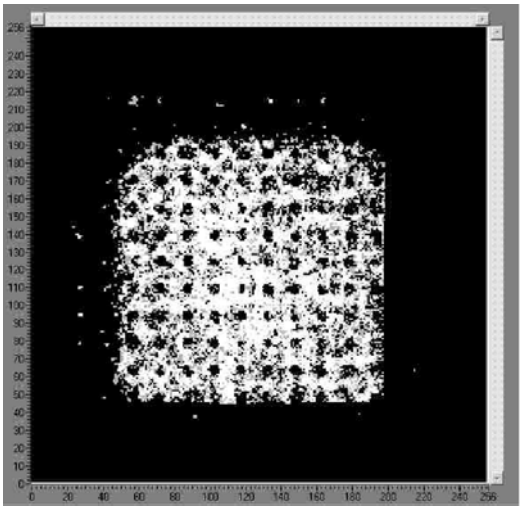

Figure 7.19: Irradiation with a ^{90}Sr source. The exposure time is 1s, with an Ar/Isobutane 95/5 mixture (estimated gas gain of 10^4). The profile of the Micromegas mesh is clearly observed. The black circular spots are the spacing pillars from the Micromegas.

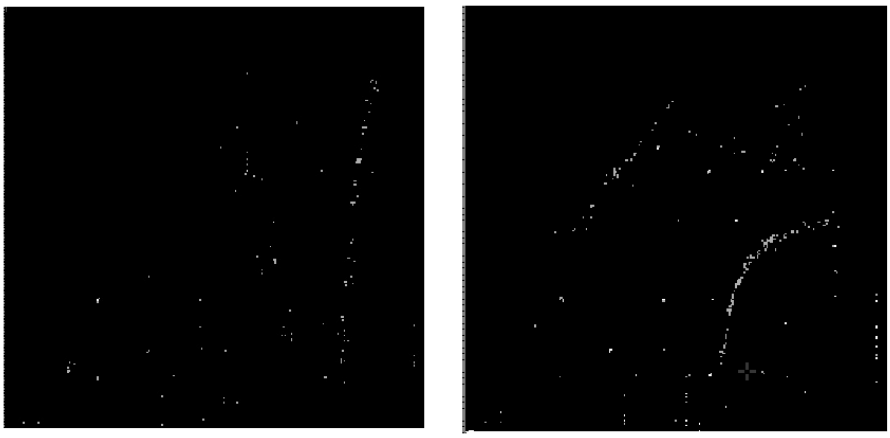

Figure 7.20: Typical raw images of cosmic ray tracks crossing the gas volume. The gas is a He/Isobutane 80/20 mixture for a gain of 1.9 × 10^4. No triggering system is used and the acquisition time is 15 seconds. The size of the images is 14.1 mm × 14.1 mm.

We note that the Micromegas TPC does not show the same diffusion and de-focusing effects encountered with the GEM prototype.

Detection of single primary electrons is more interesting for tracking application in high energy physics. For this reason, the detection of cosmic rays has been investigated. In fig. 7.20 cosmic ray tracks are observed for a set-up with a He gas mixture (gas gain 1.9 × 10^4).

This demonstrates that the Medipix2/Micromegas prototype can detect single primary electrons.

7.5.4 Single electron detection efficiency

To study the single primary electron detection efficiency, a sample of about 6000 cosmic images has been recorded. He/Isob. 80/20 mixtures have been used. However, no trigger system has been implemented. Different runs with different Medipix2 chips have been performed. The system has been operating at a gas gain of 1.9 × 10^4.

The first step of the analysis is to identify and remove defective (noisy) pixels. Then events with MIP tracks are searched for with a pattern recognition algorithm, and the length of the projection of the track on the Medipix2 plane is calculated. The following cuts have then been applied:

- The transverse projection of the track needs to be longer than 50 pixels (i.e., 2.75 mm)
- Each track has more than 5 hits

- The rms of the track fit in the Medipix2 plane is larger than 4 pixels
- The ratio between the number of pixels associated to the track by the pattern recognition algorithm and the total number of pixels hit needs to be larger than 80%

Furthermore, only tracks that do not cross the boundary of the sensitive area are selected. In this way any ambiguity relative to the third coordinate is eliminated, and it is possible to calculate the three-dimensional length of the track $L = \sqrt{d^2 + L_{proj.}^2}$, where d is the drift length (15 mm) and $L_{proj.}$ is the length of the projection of the track onto the Medipix2 plane (see fig. 7.21).

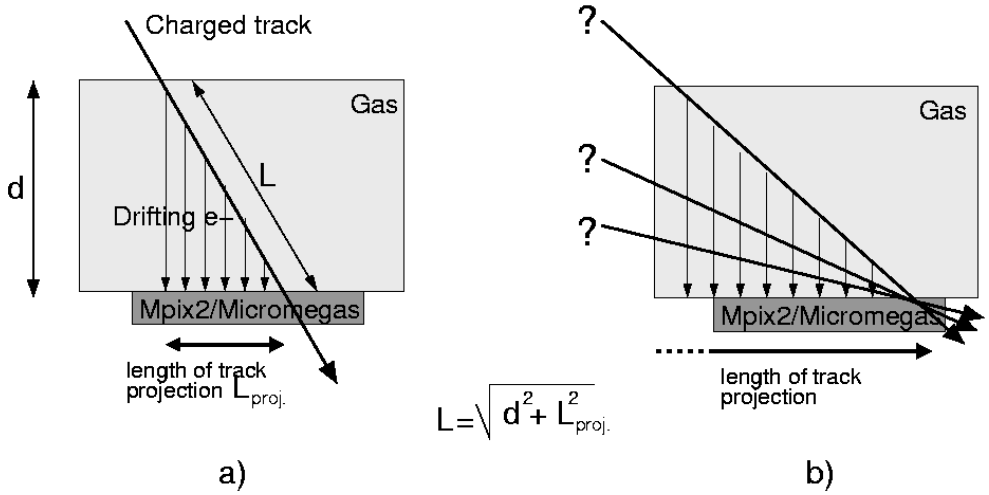

Figure 7.21: Only tracks with a projection inside the sensitive area are selected (a). When a track crosses the boundary of the sensitive area an ambiguity is introduced (b).

A set of 164 tracks satisfies the selection criteria. A typical track is shown in fig. 7.22. Noisy pixels have been eliminated.

Dividing the number of clusters for each track by the individual track length provides the average number of clusters per unit track length. This numbers equals the detected number of primary electrons per unit length ($N_{Detected}$). The expected number of primary electrons per unit length produced by a MIP ($N_{Expected}$) is determined by the gas properties. The detection efficiency becomes:

$$\epsilon = \frac{N_{Detected}}{N_{Expected}} \tag{7.3}$$

and mainly depends on the voltage applied to the Micromegas and discrim-

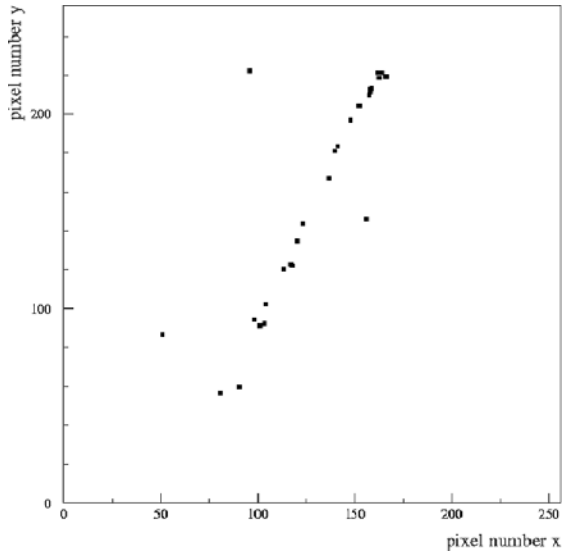

Figure 7.22: An image of a typical analyzed cosmic ray track. Noisy pixels are suppressed.

inator levels. For He-based gas mixtures operating at a gain of 1.9×10^4, with a discriminator threshold at 3000 e^-, the Medipix2/Micromegas system has a single electrons efficiency better than 90%. This value will be improved in the future: Medipix2 detectors have already shown stable operation at a threshold level of about 1000 e^-, thanks to careful tuning.

7.5.5 Suppression of δ-rays

Depending on their energy and emission angle, δ-rays may part from the original track. Furthermore, these high-energy recoil electrons will create substantial ionization (*secondary ionization*). This results in secondary tracks.

With traditional readout systems based on large pads, the charge produced by the avalanches due to δ-ray ionization is still associated to the main track, since the pad is too large to discriminate between the two tracks close to each other. This adds to the systematic error in the track measurement.

As the spatial resolution offered by our prototype TPC is much better due to a reduced pad size, discrimination against δ-rays is obtained. Fig. 7.23 demonstrates the power of discrimination: emission of a δ-ray is clearly observed.

7.5.6 The Moiré effect

Fig. 7.24 shows the uniform irradiation of the chamber with β rays from a ^{90}Sr source (the image was acquired with a standard, non-processed chip). The top-left corner of the device is clearly less efficient. This is due to the non-flatness

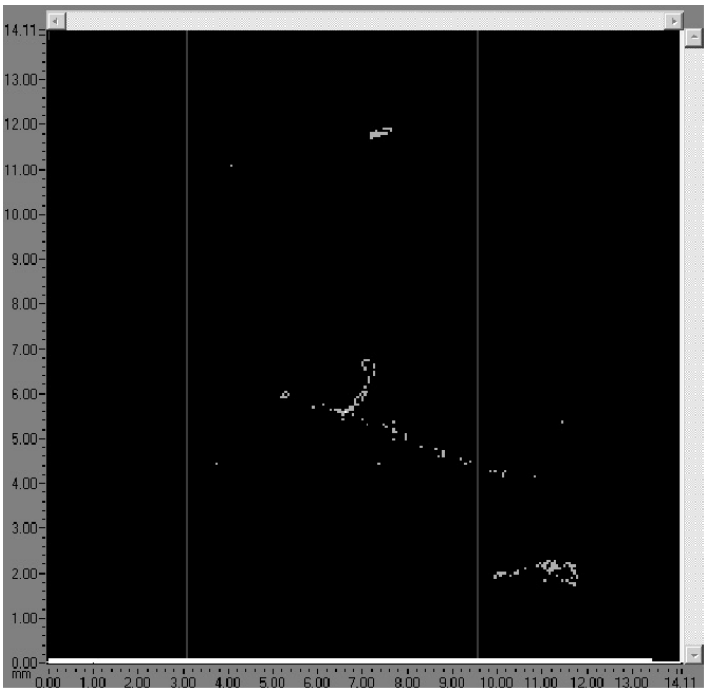

Figure 7.23: A δ-ray (raw image) departing under large angle from the main track is clearly visible in the center of image.

of the Micromegas mesh. Apparently, the electrostatic force could not entirely eliminate its non-flatness. In this area, the pillars are not in contact with the surface of the Medipix2 chip, so that the multiplication gap is wider than 50 μm and the gain is reduced.

Dead regions due the presence of the spacing pillars from the Micromegas are also visible. But another interesting structure also appears: band-shaped regions with a reduced efficiency. Note that these bands are also present in the perpendicular direction, and repeated with a periodicity of 12 pixels.

The presence of these bands can be explained in terms of the Moiré effect[3]. The pixel size of the Medipix2 chip (55 μm $\times$ 55 μm) does not exactly match the pitch of the holes in the Micromegas foil (60 μm in both directions). Consequently, the hole position with respect to its nearest pixel center shifts along the pixel row or pixel column (see fig. 7.25). The relative hole/pixel position repeats with the following periodicity:

$$P = \frac{60}{60 - 55} = 12 \quad pixels! \tag{7.4}$$

[3]Moiré fringes are an interference pattern that is formed when two grid-like patterns, with slightly different pitches, are superimposed. The result is a series of fringe patterns that change shape as the grids are moved relative to each other.

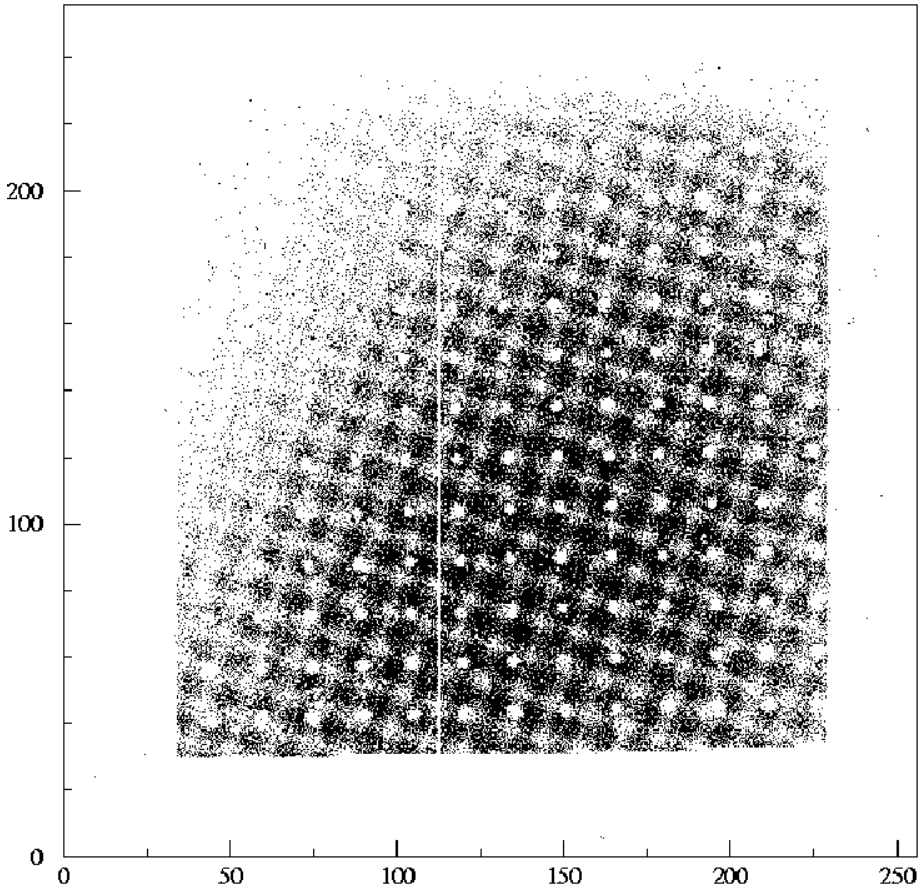

Figure 7.24: Analyzed image of ^{90}Sr irradiation (counting pixels are shown in black). Bands of lower efficiency hare visible. These bands run in two perpendicular directions and repeat with a periodicity of 12 pixels. In this particular assembly, the upper left corner has a low efficiency. This is due to a non perfect alignment (planarity) of the Micromegas mesh with the Medipix2.

Due to misalignment of the Micromegas plane, the Moiré effect may also show up at a certain angle with respect to the Medipix2 plane.

The drop in efficiency in the bands (fig. 7.25) is caused by the following effects:

- When a mesh hole is positioned above an edge between two adjacent pixels, or above the corner between four neighbours, the avalanche can be split among two or even four adjacent pixels. Thus each pixel will receive only a fraction of the total charge, which in many cases will not be sufficient to pass the threshold.
- The anode (pixel cell) is partially covered by insulating material (SiN_2). If a Micromegas hole is located above the edge of two neighbouring pixels, or above the four adjacent corners of four pixels, the electrons will be pulled toward the collecting metalized pad, which lies further away. Along this path the electric field is weaker and so less gain is achieved. The total charge produced is thus lower, and may not satisfy the threshold.
- Since the chip with which the image was obtained did not undergo post-processing, the insulating dielectric covers a large fraction of the pixel. The charge build-up in the dielectric may result in a significant efficiency drop in these regions.

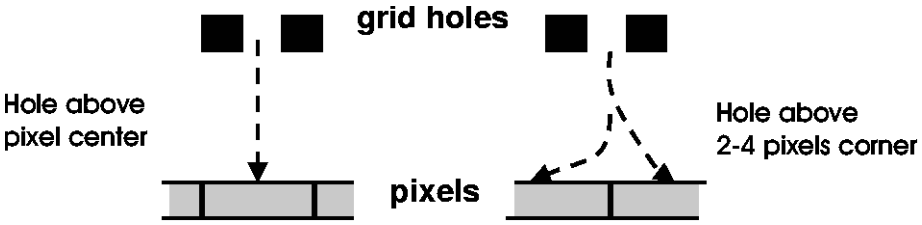

Figure 7.25: When a grid hole does not lie above a pixel center but above the edge between two or more neighbours, a drop in efficiency may occur because 1) the signal is split between the adjacent pixels, 2) the electrons drift in a weaker field with a lower gas gain, and 3) the electrons may hit the surface dielectric instead of the charge collecting pad.

The Moiré effect will be eliminated by the integration of the gas gain grid and the chip, obtaining a perfect alignment between grid holes and anode pixels.

7.5.7 Discharges and damage to the Medipix2 chips

Several Medipix2 chips have been damaged during the tests and cannot be recovered. The damage is caused by sparks in the amplification gap. To obtain larger gas gains, the voltage between the Medipix2 chip and the Micromegas

mesh was often increased to very high values. Then, the risk of HV breakdowns increases as well. In some cases sparks could be detected with a low-noise charge-sensitive preamplifier connected to the Micromegas[4].

Careful examination of the surface of damaged Medipix2 chips with a SEM at the MESA+ institute at University of Twente shows severe local damages, obviously a result of discharges. These occurred when the electrical field in a He/Isob. 80/20 mixture reached or exceeded 9000 V/mm. An example is shown in fig. 7.26: a deep hole is clearly visible in the pixel hit by the spark. The surrounding surface is covered by melted (and re-crystallized) aluminum. Melted SiN is also present in this area.

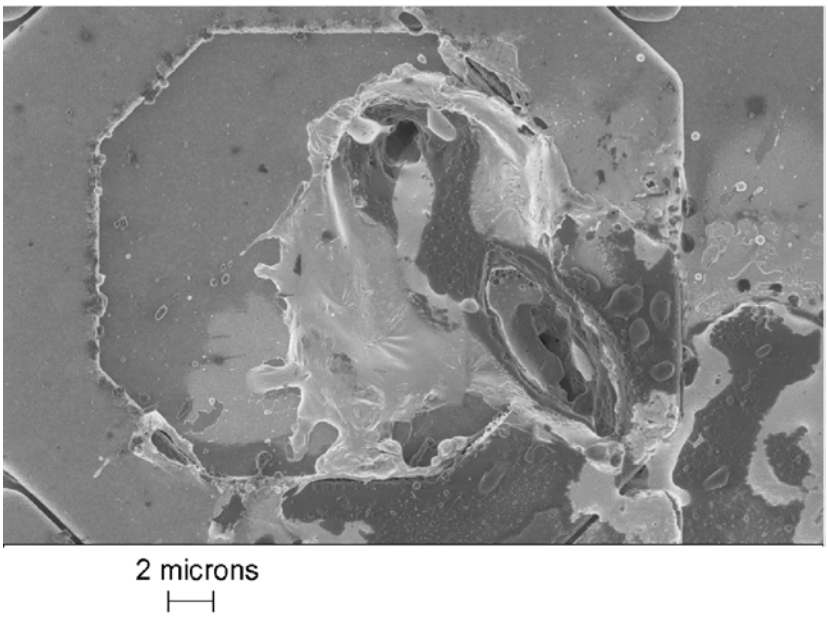

Figure 7.26: SEM image of a damaged Medipix2 chip. The result of a discharge is shown (note the octagonal bump-bonding pad). Two deep holes, reaching the inner layers of the chip, are clearly visible, while the surrounding area is covered by melted and re-crystallized aluminum.

7.5.8 Metalized and non-metalized Medipix2 chips

Both standard and post-processed Medipix2 chips have proved to be capable of single electron detection, although a detailed study of possible differences in performance and efficiency has not been carried out yet. Both types of chip

[4]This preamplifier is also used for gas gain calibration purposes

demonstrate similar damage when an excessively high electric field is created between pixels and Micromegas mesh. A detailed study is pending.

On the other hand, a different behaviour has been observed as to the Moiré effect. In the case of metalized Medipix2 chips, the inefficiency bands are not so pronounced.

7.6 Conclusions and future plans

We developed a prototype detector with a Medipix2/Micromegas combination demonstrating the feasibility of a CMOS pixel readout in a gas multiplication device. Single primary electrons have been detected with very good efficiency (>90%).

However, to study a pixel TPC in more detail, the design of a dedicated chip is indispensable. This *TimePix* chip is currently under development. It will not be a counting device, but instead it will measure the drift time of the primary electrons, replacing the counting logic with time stamping.

Essential studies for the new layout are:

- Optimization of pixel geometry (square, rectangular, hexagonal)
- Optimization of pixel pitch (spatial resolution, pixel noise, power dissipation)
- Optimization of ratio of pad/pixel surface (electron collection, minimization of dead area)
- Influence of insulating materials at the pads or near to them (dielectric may charge up in an intense electric field)
- Sensitivity for HV breakdowns between gas gain grid and pixel pads
- Required number of discriminator thresholds
- Preamplifier noise
- Time resolution
- Output data processing
- Power dissipation, cooling

Integration of the gas gain grid directly on the TimePix chip, avoiding grid alignment, will simplify the setup considerably. All components will be integrated in a single device.

By post-processing the wafer, a 50 μm layer of insulating poly-imide can be added. On top of the insulator, a thin metal layer will be deposited. Holes are etched in the metal and underlying resist, until the pixel pads are reached. By means of standard processing techniques, an on-chip GEM or Micromegas foil is created. Alternatively, small 50 μm insulating pillars can be deposited

on the chip, with a Micromegas foil on top. The approach differs only in the amount of insulating material between the grid and the pixels, and has to be optimized so that the highest possible gain is reached while minimizing risks of HV breakdown.

Application of such a grid is currently investigated at MESA+ (University of Twente) in a project called *InGrid* (Integrated Grid). First prototypes have been produced. No test results are available yet.

Another possible application of the combination CMOS readout/post-processed gas gain grid is currently examined in the *GOSSIP* (Gas On Slimmed SIlicon Pixels) project. Gossip focuses on the development of a gas tracking detector for a high-flux environment like in the LHC.

Appendix A

Bump-bonding pixel detectors

Flip-chip bonding (or *bump bonding*) [59] provides direct electrical connection of face-down (hence *flipped*) electronic components onto substrates, circuit boards, or carriers, by means of conductive bumps on the chip bond pads. For hybrid pixel detectors, bump-bonding techniques are used to connect the CMOS electronics chip to the semiconductor sensor.

Here we briefly discuss two methods used for pixel detectors: solder bump deposition and evaporative deposition of indium.

A.1 The solder bump flip-chip process

The flip-chip solder connection technology was developed by IBM. The first assemblies were produced in the 1960's. Today, the process has become a mature connection technology, applicable in large scale production.

There are four sequential steps in a solder bump process: preparing the wafer for solder bumping, depositing or placing the solder bumps, attaching the bumped die to the board, substrate, or carrier, and completing the assembly with an adhesive underfill.

A.1.1 Under-Bump Metalization

The first step is preparing the wafer bumping sites on the bond pads of the ASICs (fig. A.2 a)). This preparation includes cleaning, removing insulating oxides, and providing a pad metalization that will protect the IC while making a good mechanical and electrical connection to the solder bump and the board (fig. A.2 b)).

This *under-bump metalization* (UBM) consists of successive layers of metals with different functions. The *adhesion layer* must adhere well to both the bond pad metal and the surrounding passivation, providing a strong, low-stress

mechanical and electrical connection. It is usually made of Cr or TiW. The *diffusion barrier* layer (Cr-Cu or Cu) limits the diffusion of solder into the underlying material, especially into the chip top metal layer. The *solder wettable* layer, usually made of Cu, offers an easily wettable surface to the molten solder during assembly, for good bonding of the solder to the underlying metal. A *protective layer* may be required to prevent oxidation of the underlying layer, and a typical metal used for this purpose is Au. Thus, an example of a possible UBM is the following succession of layers: Cr/Cr-Cu/Cu/Au. Another typical UBM is Ti/W with copper (or Ni/Au) a few microns thick to adhere to the solder. The width of the openings in the passivation layer on the electronics wafer is about one-half of the bump diameter.

A.1.2 Solder Bumping

Solder bumps may be deposited or placed on the UBM in many different ways, and the results of these methods may differ in bump size and spacing, solder components and composition, cost, manufacturing time, equipment required, assembly temperature, and UBM (fig. A.2 c) and d)). A few examples are listed below:

- Evaporated UBM/Evaporated Solder
- Sputtered UBM/Electroplated Solder
- Sputtered UBM/Printed Solder
- Electroless UBM/Printed Solder

After the solder is electroplated, the wafer is etched to remove the UBM (except below the solder). The final step is to reflow the solder, to obtain spheres as in fig. A.1. The reflow occurs at different temperatures, depending on the solder composition, but usually ranges from 230C (63SnPb) to 360C (5SnPb). Eutectic solder (37% Pb and 63% Sn) is most commonly used in high energy physics detectors.

A.1.3 Assembly

Assembly operations include handling, placing, fluxing, and solder joining. The assembly procedure is affected by the bumped die packaging, the solder bump, the substrate or board material and size, assembly equipment, end product, and cost.

Bumped dies may be transported in waffle packs or tape and reel. Tape and reel transportation requires special tapes designed for carrying flip chips. Placing the bumped die may be by fine-pitch surface-mount equipment, or by high-accuracy flip chip placement equipment. In either case, the die must be aligned with the bond pads on the board before placement. Soldering may be in a belt furnace or by hot gas.

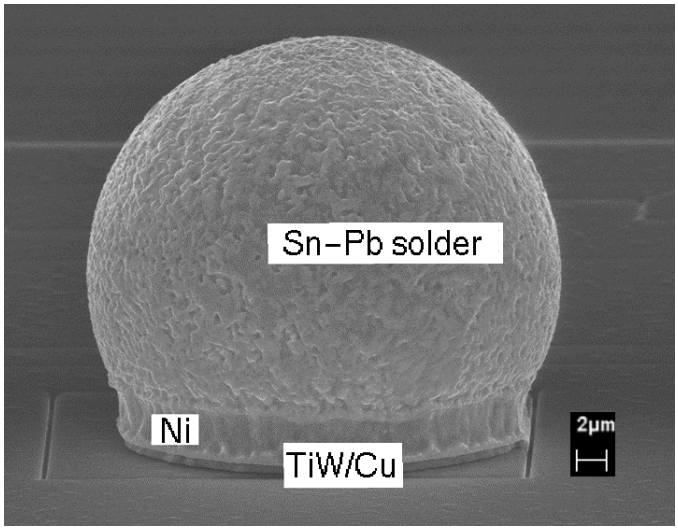

Figure A.1: A scanning electron microscope image of a single solder bump showing the metal composition described in the text [58].

A.1.4 Underfilling

The solder bump crates a small space between the chip and the board. In the last stage of the assembly process, this under-chip space can be filled with a non-conductive *underfill* adhesive, joining the entire surface of the chip to the substrate.

A.1.5 Remarks

Strong arguments in favor of the solder-bump flip-chip manufacturing process are:

- Very good uniformity and self alignment
- High connection yield
- Optimal height/pitch ratio (20μm/50μm), thus bumps are grown only on either the ASIC or the semiconductor sensor
- Excellent electrical properties (contact resistance of the order of mΩ)

On the other hand, this technique also has several critical steps:

- Complex UBM: imperfections in the metallurgy may result in poor adhesion
- Exposure to high temperatures may harm radiation hard ASICs
- The pitch is at the edge of the industrial standard

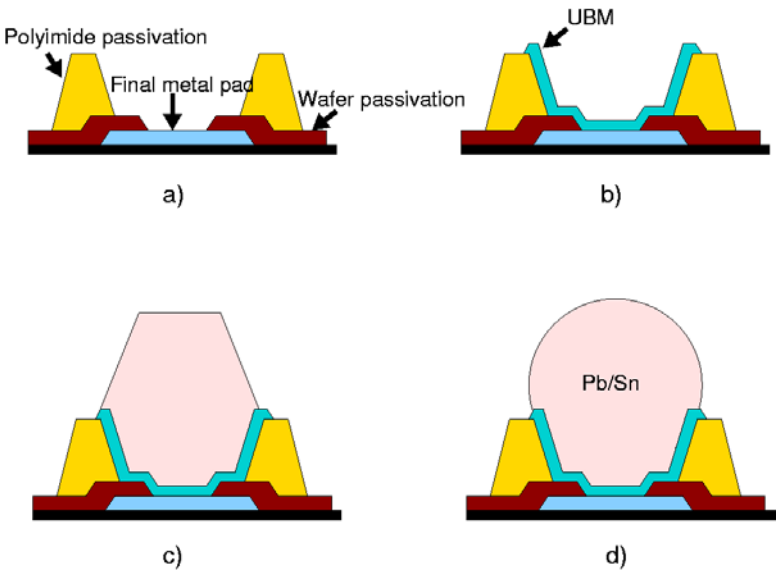

Figure A.2: Main steps in a common solder bump-bonding procedure. a) wafer cleaning, b) UBM deposition, c) Solder deposition and d) reflow to form solder bump.

A.2 The indium bump process

Indium bump technology is a unique process for mainly flip chip assembly of semiconductor components. Indium is deposited onto a wafer as the last step in a photolithography/metalization process. Both sensor and electronics are processed with indium, since the maximum obtainable height of an indium pillar is small compared to the pitch.

The main steps of the bump-bonding procedure are the following. Masks are designed for both sensor and ASIC. The wafer is cleaned (fig. A.3 a)) and the UBM is completed (fig. A.3 b) and c)), then a thick photoresist is deposited (fig. A.3 d)). For a 5 - 6 μm high indium pillar, an 8 - 9 μm thick photoresist layer is used. A vacuum-thermal evaporation of 30 nm of chromium, followed by several μm of indium, is made (fig. A.3 e)). Then a metal lift-off is carried out, and indium pillars (bumps) of several microns in height remain (fig. A.3 f)). The height and shape of the bumps are determined by the the mask design and the properties of the photoresist used.

Both the semiconductor sensor and the readout chip are inserted into a flip chip bonder and aligned. Then the parts are either compression or thermo-compression bonded together. The bump area determines the amount of pressure needed for successful bonding. If a substantial amount of indium is being used (e.g. to improve thermal conductivity) thermo-compression bonding will be necessary.

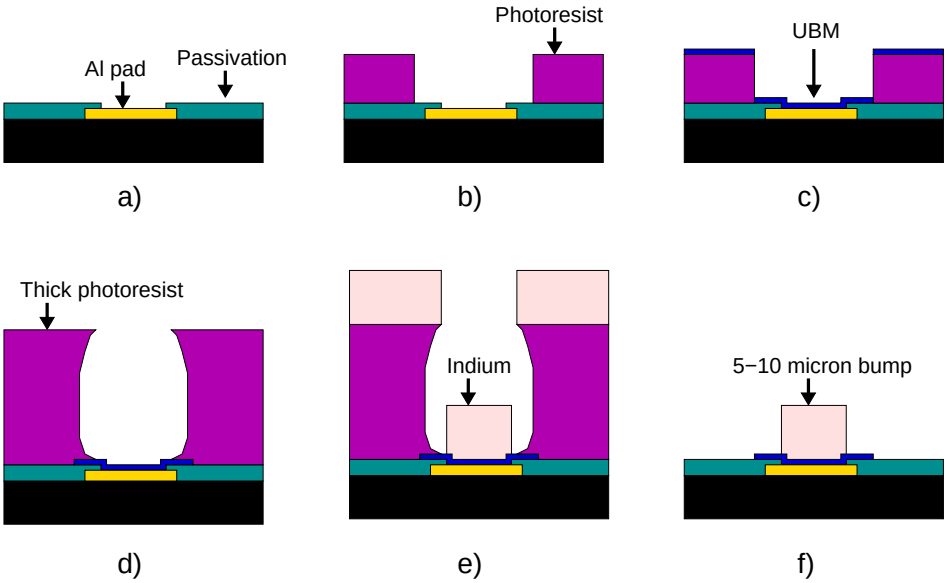

Figure A.3: Main steps in an indium bump-bonding procedure. a) wafer cleaning, b) patterning of photoresist, c) UBM deposition, d) lift-off, patterning of thick photoresist, e) evaporation of indium and f) lift-off to leave only the indium bump.

The indium bump-bonding process presents several advantages over other techniques:

- Simple UBM: adding a Cr adhesion layer is sufficient
- Low temperatures, in the range 20-100C, are sufficient
- The pitch is well within industrial standards (30 μm pitch)
- The elasticity of the indium can help against thermal fatigue

This technology is relatively inexpensive and easy to introduce into a wafer-processing run. Shape, size and positioning of the bumps are well controlled and flexible.

However, other aspects of the bonding procedure are more critical:

- To achieve a high contact yield, excellent planarity and bump uniformity are required
- Due to the small height/pitch ratio (5 μm/50 μm), bumps have to be grown on both components (semiconductor and electronics)
- The applied pressure may damage the bonded devices

- Indium bumps are not easily reworked

In the case of the Medipix1 detector, a stronger capacitive coupling between readout pixels and sensor diodes has been observed. Indium bump bonds are much smaller than solder bumps (typical diameter of 20 μm instead of 50 μm), and thus the distance between sensor and electronics chip is reduced. This larger capacitance leads to an increase in input noise.

A.3 Inspection

Quality assurance before and after flip-chip assembly is important to obtain the highest yield. The bumps are inspected at wafer level in an automatic procedure. Several procedures, both 2D (camera and pattern recognition) and 3D (laser interferometry) are now available to trace missing bumps, merged bumps, deformed bumps or other defects. A survey of the bumps height is also obtained. X-ray inspection has been routinely used to inspect assemblies after flip-chip assembly and provides a direct mean to correlate bump defects with malfunctioning pixels.

The bump defect rate at wafer level is the order 10^{-6}. However, additional defects are introduced during the flip-chip process. Typical defect rates after flip-chip assembly are of order 10^{-5}.

For a useful compendium of the bump-bonding procedures introduced in this appendix, see for instance [60].

Bibliography

[1] S. Eidelman *et al.*, *The Review of Particle Physics*, Physics Letters **B592**, 1 (2004).

[2] W.R. Leo, *Techniques for Nuclear and Particle Physics Experiments*, Springer-Verlag (1993).

[3] C.M. Davisson, *Interaction of gamma radiation with matter* in *Alpha-, Beta- and Gamma-Ray Spectroscopy*, edited by K. Siegbahn, North-Holland (1968).

[4] R.M. Sternheimer, S.M. Seltzer, M.J. Berger, Phys. Rev. **B26**, 6067 (1982); erratum in **B27**, 6971 (1983).

[5] R.M. Sternheimer, M.J. Berger, S.M. Seltzer, At. Data and Nucl. Data Tables **30**, 262 (1984).

[6] Review of Particle Properties in Phys. Rev. **D45**, Part II (1992).

[7] K. Rossman, *Point-spread function, line-spread function and modulation transfer function*, Radiology **93** (1969), 257-272.

[8] C.Froejdh and P.Nelvig, *Performance Criteria forX-Ray Imaging Sensors*, Physica Medica XIV (1998) 10-12 (Suppl. 2).

[9] J.C. Dainty and R. Shaw, *Image Science*, Chapters 6-7, Academic Press, New York (1974)

[10] U. Welander *et al.*, *Resolution as defined by line spread and modulation transfer functions for four digital intraoral radiographic systems*, Oral and Maxillofacial Radiology, Oral Surg Oral Med Oral Path **78** (1) (1994) 109-115.

[11] U. Welander *et al.*, *Absolute measures of image quality for the Sens-A-Ray direct digital intraoral radiography system*, Oral and Maxillofacial Radiology, Oral Surg Oral Med Oral Path **80** (3) (1995) 345-350.

[12] J.T. Dobbins, *Effects of undersampling on the proper interpretation of modulation transfer function, noise power spectra, and noise equivalent quanta of digital imaging systems*, Med. Phys. **22** (2) (1995) 171-181.

[13] J. Giersch, D. Niederlöhner, G. Anton, *The influence of energy weighting on X-ray imaging quality*, Proceedings of the 5^th International Workshop on Radiation Imaging Detectors (IWORID), Riga (Latvia) - September 7-11, 2003, p. 68.

[14] F. Pedersen *et al.*, *Energy discrimination with an X-ray pixel detector - a Monte-Carlo simulation*, Nucl. Instr. and Meth. **A 395** (1997) 443-447

[15] D.R. Dance and R. Davis, *Simulation of mammography by Monte Carlo calculation - The dependence of radiation dose, scatter and noise on photon energy*, in G. Drexler, H. Eriskat, and H. Schibilla, editors, *Patient exposure to radiation in medical X-ray diagnosis*, pages 227-242, EUR7438 (1981)

[16] M. Saebel and H. Aichinger, *Recent developments in breast imaging*, Phys. Med. Biol. **41** (1996) 315-368.

[17] D. San Segundo Bello, B. Nauta, J.L. Visschers, *Pixel-level analog-to-digital converters for hybrid pixel detectors with energy sensitivity*, Proc. of the IEEE Nuclear Science Symposium and Medical Imaging Conference, Lyon, France, October 15-20, 2000, ISBN 0-7803-6503-8, pp. 9 (98-102).

[18] E.H.M. Heijne, *Future semiconductor detectors using advanced microelectronics with post-processing, hybridization and packaging technology*, submitted to Nucl. Instr. and Meth. A for Proceedings of STD5 Hiroshims, 14-17 June 2004.

[19] M. Campbell *et al.*, *Readout for a 64 × 64 pixel matrix with 15-bit single photon counting*, IEEE Trans. Nucl. Sci. **45** (1998) 751.

[20] G. Bardelloni *et al.*, *A new read-out system for an imaging pixel detector*, Proc. of the IEEE Nuclear Science Symposium and Medical Imaging Conference, Lyon, France, October 15-20, 2000, **ISBN 0-7803-6503-8**, pp. 12 (57-60).

[21] E. Bertolucci, T. Boerkamp, M. Maiorino, G. Mettivier, M.C. Montesi, and P. Russo, *Portable System for Imaging of α, β and X-Ray Sources With Silicon Pixel Detectors and Medipix1 Readout*, IEEE Trans. on Nucl. Sci., Vol. **49** (4), august 2002.

[22] A. Fornaini, D. Calvet, J.L. Visschers, *Soft X-ray sensitivity of a photon-counting hybrid pixel detector with a silicon sensor matrix*, Nucl. Instr. and Meth. in Phys. Res.**A 466** (2001) 142-145

[23] Medipix collaboration internal meeting

[24] B. Mikulec, *Single photon detection with semiconductor pixel arrays for medical imaging applications*, PhD thesis, University of Vienna, Austria, June 2000, **CERN-THESIS-2000-021**.

[25] B. Mikulec, *Development of Segmented Semiconductor Arrays for Quantum Imaging*, Nuclear Instruments and Methods in Physics Research A **510** (2003) 1-23.

[26] M.G. Bisogni *et al.*, *Performance of a 4096 pixel photon counting chip*, Proc. SPIE Vol. 3445 (1998) 298-304 and CERN-EP/98-162.

[27] C. Schwarz *et al.*, *X-ray imaging using a hybrid photon counting GaAs pixel detector*, Nucl. Physics B (Proc.Suppl.) **78** (1999) 491-496 and FREIBURG-EHEP-98-11.

[28] B. Mikulec, M. Campbell, G. Dipasquale, C. Schwarz, J. Watt, *Characterisation of a single photon counting pixel system for imaging of low-contrast objects*, Nucl. Instr. and Meth. in Phys. Res. **A 458** (2001) 352-359 and CERN-EP/99-167.

[29] C. Ponchut *et al.*, *Evaluation of a photon-counting hybrid pixel detector array with a synchrotron X-ray source*, Nucl.Instr.and Meth.in Phys.Res.**A 484** (2002) 396-406.

[30] C. Ponchut, *Pixel detectors in counting mode: limitations induced by the pulsed time structure of the X-ray beam*, ESRF Internal note CP/16/99, 1999.

[31] J.E. Bateman, *The effect of beam time structure on counting detectors in SRS experiments*, J. Synchr. Radiat. **7** (2000) 307.

[32] L. Abate *et al.*, *Noise and interpixel dead space studies of GaAs pixellated detectors*, Nucl. Instr. and Meth. in Phys. Res. A **458** (2001) 164.

[33] C. Broennimann *et al.*, *Synchrotron beam test with a photon-counting X-ray detector*, J. Synchr. Radiat. **7** (2000) 301.

[34] V. Kogan, K. Bethke, R. de Vries, *Applying X-rays in material analysis*, Nucl. Instr. and Meth. in Phys. Res., **509** (2003) 290.

[35] MCNC, *Microelectronics Center of North Carolina*, North Carolina - USA

[36] X. Llopart *et al.*, *Medipix2, a 64k pixel readout chip with 55 μm square elements working in single photon counting mode*, IEEE Trans. Nucl. Sci., vol. **49**, 2279-2283, October 2002.

[37] F. Krummenacher, *Pixel detectors with local intelligence: an IC designer point of view*, Nucl. Instr. and Methods in Phys. Res. A **305**, 1991, 527-532.

[38] V. Fanti, R. Marzeddu, P. Randaccio, *Medipix2 parallel readout system*, Nucl. Instr. and Meth. in Phys. Res. A, **509**, Issue 1-3, 171-175.

[39] D. San Segundo Bello *et al. Design of an interface board for the control and DAQ of the Medpix2 chip*, Proceedings of the 4^th International Workshop on Radiation Imaging Detectors, Amsterdam, The Netherlands, Sept. 8-12, 2002.

[40] M. Conti, M. Maiorino, G. Mettivier, M. C. Montesi, and P. Russo, *Preliminary Test of Medisoft 4: Control Software for the Medipix2 Readout Chip*, IEEE Trans. on Nucl. Sci., Vol. **50**, no. 4, October 2003.

[41] L. Tlustos, M. Campbell, E. Heijne and X. Llopart, *Signal variations in high granularity Si pixel detectors*, IEEE Trans. Nucl. Sci., 51(6), 2004

[42] Medipix collaboration, internal note.

[43] P.R. Granfors *et al. Performance of a 41×41 cm^2 amorphous silicon flat panel X-ray detector designed for angiographic and R&F imaging applications*, Medical Physics, October 2003, Vol. 30, Issue 10, pp. 2715-2726.

[44] S. Parker, *Semiconductor track detectors: a brief history from 0D to 3D*, proceeding of the 6th IWORID, Glasgow, July 25-29 2004

[45] C. Da Viá, *3D Silicon and radiation hardness*, proceeding of the 6th IWORID, Glasgow, July 25-29 2004.

[46] IPC/JPCA-2315, *Design Guide for High DensityInterconnects.*

[47] ACB, *Advanced Circuit Boards*, Dendermonde - Belgium.

[48] G. Charpak *et al.*, Nucl. Instr. and Meth. Phys. Res. **62**, 235 (1968).

[49] A. Breskin *et al.*, Nucl. Instr. and Meth. Phys. Res. **124**, 189 (1975).

[50] R.J. Madaras, P.J. Oddone, Physics Today **37**, No. 8, 36 (Aug. 1984).

[51] J.A. MacDonald (ed.), *The Time Projection Chamber*, AIP Conf. Proc. **108** (American Inst. of Physics, New York 1984).

[52] Y. Giomataris *et al.*, Nucl. Instr. and Meth. Phys. Res. A **376** (1996) 29-35.

[53] F. Sauli *et al.*, *The gas electron multiplier (GEM)*, CERN-PPE-96-177, Geneva, CERN, 4 Nov. 1996.

[54] R.K. Carnegie *et al.*, *Resolution studies of cosmic-ray tracks in a TPC with GEM readout*, submitted for publication in Nucl. Instrum. Methods Phys. Res. A.

[55] D. Karlen, *et. al.*, *Investigation of GEM Space Point Resolution for a TPC Tracker*, proceedings, LCWS 2000 (Physics and Experiments with Future Linear e^+e^- Colliders), Fermilab, October 2000, AIP Conference Proceedings, Volume **578** (2001) 817.

[56] M. Campbell et al., *The detection of single electrons by means of a Micromegas-covered MediPix2 pixel CMOS readout circuit*, Accepted by Nucl. Instr. and Methods Phys. Res. A, http://www.arxiv.org/physics/0409048.

[57] F. Sauli, *Principles of operating of multiwire and proportional drift chambers*, CERN Yellow Report 77-09, 1977.

[58] VTT Electronics, Helsinki - Finland

[59] M. Pecht, *Integrated circuit hybrid, and multichip module package design guidelines*, John Wiley & Sons, Inc. - New York 1994.

[60] J. H. Lau, *Flip Chip Technologies*, McGraw Hill 1996.

Summary

The Medipix collaboration, has been created to transfer the technology of hybrid pixel detectors from high energy physics experiments to X-ray imaging. Pixel devices have an excellent dynamic range, high signal-to-noise ratio and good flexibility (as different semiconductor sensors may be chosen, depending on the specific application).

The Medipix1 CMOS ASIC (1997) was the first readout chip designed by the collaboration. It features a total of 4996 pixels, organized as a matrix of 64 $\times$ 64 cells. The cell size is 170 μm $\times$ 170 μm. The chip is flip-chip bonded to a semiconductor X-ray sensor with a corresponding pixel matrix. The sensor material most commonly used is silicon. A characterization of the detector, carried out with a synchrotron beam at the ESRF facility, is presented. Several important conclusions are drawn. The device can detect photons with an energy as low as 6 keV, which is important for many soft X-ray applications. The absolute energy calibration and linearity response to flux have been determined, and the ENC noise is measured to be approximately 170 e^-. Charge sharing between adjacent pixels is also studied: no signal loss at the pixel edges is found.

After the Medipix1 hybrid pixel approach in X-ray imaging was proven successful, the collaboration designed a new version of the chip, called Medipix2 (2002). The steady progress in CMOS technology allows an enhanced functionality of each pixel cell, with a significant reduction in size. The Medipix2 pixel cells are about 9 times smaller: 55 μm $\times$ 55 μm, in a matrix of 256 rows and 256 columns.

However, the hybrid pixel detector approach has a major drawback for X-ray imaging. Due to the manufacturing procedure, the yield of electronics chips is inversely proportional to the size of the chip. Therefore, at first instance, the sensitive area of the X-ray detector is limited to the size of the CMOS ASIC (about 2.5 $\times$ 2.5 cm^2). In order to arrive at a large area X-ray imager, a prototype chipboard capable of hosting an array of 2 $\times$ 4 Medipix2 detectors has been designed. Arrays of 2 $\times$ 2 detectors (8 cm^2 sensitive area) are currently in use by the collaboration.

Building on the success of the Medipix2, we present an interesting application of the chip in high energy physics. Coupled to a Micromegas gas gain grid instead of a semiconductor sensor, the chip is used as readout element in a gas multiplication tracking detector. A small prototype Time Projection Chamber has been developed, and single primary electrons from cosmic tracks have been

detected with an efficiency better than 90%.

These detectors will outperform conventional gas chambers. Traditional readout pads (typical size of about 5-10 mm^2) are replaced by 100 μm $\times$ 100 μm pixels. This offers a much higher granularity, resulting in a drastic reduction in hit occupancy. Spatial resolution is improved, which also results in better δ-ray recognition and multi-track separation. Moreover, single electron detection provides precise dE/dx measurements.

A further improvement is obtained when the gas gain grid is integrated on the CMOS chip by means of wafer-scale post-processing. In this way, the grid reticule will be intrinsically aligned to the pixels. Furthermore, the assembly and maintenance of the detector will be less complex, since all the readout components (pad, preamplifier, external circuitry etc.) and the gas multiplication structure are integrated in one single element.

Samenvatting

Het Medipix samenwerkingsverband is ontstaan uit de behoefte om hybride pixeltechnologie, ontwikkeld in de Hoge Energie Fysica, over te dragen naar andere toepassingsgebieden zoals Röntgenonderzoek. Detectieapparatuur gebaseerd op deze technologie heeft een uitstekend dynamisch bereik, een grote signaal/ruisverhouding en is uiterst flexibel (de elektronica kan eenvoudig verbonden worden met halfgeleider sensoren die geoptimaliseerd zijn voor de detectie van specifieke straling/deeltjes).

De Medipix1 CMOS ASIC (1997) was de eerste binnen het samenwerkingverband ontwikkelde uitlees-chip. Deze ASIC bevat in totaal 4996 pixels, geordend in een matrix van 64 $\times$ 64 cellen. Elke cel heeft een afmeting van 170 μm bij 170 μm. De ASIC wordt met behulp van flip-chip technologie verbonden met en halfgeleider (silicon) sensor.

De eigenschappen van de detector zijn in detail onderzocht met behulp van de ESRF synchrotronstraling-faciliteit en worden uitgebreid besproken in deze dissertatie. Enkele belangrijke conclusies kunnen getrokken worden. Bijvoorbeeld, de hybride detector slaagt erin om nauwkeurig laag energetische fotonen waar te nemen ($E_\gamma > 6$ keV). De absolute energieschaal en de respons als functie van de flux zijn bepaald. Tevens is de ruisbijdrage aan het signaal gemeten; slechts 170 e- ENC. De ladingsverdeling over aangrenzende pixelcellen is bovendien onderzocht: er treedt geen significant signaalverlies op aan de randen van de pixels.

Na de succesvolle toepassing van de Medipix1 chip, besloot de collaboratie tot de ontwikkeling van een nieuwe chip: de Medipix2 (2002). De continue verbetering van de CMOS technologie maakt dat iedere pixelcel met meer functionaliteit toegerust kan worden, terwijl tegelijkertijd de afmetingen drastisch kunnen afnemen. De Medipix2 cel is qua oppervlak een factor 9 kleiner dan de cel in het Medipix1-ontwerp, n.l. 55 μm bij 55 μm, terwijl de chip nu 256 rijen en 256 kolommen bevat.

Echter, de hybride pixel benadering heeft een grote beperking wanneer grote objecten moeten worden afgebeeld. Omdat het aantal goed functionerende elektronica chips dat van een wafer verkregen wordt omgekeerd evenredig is met het oppervlak van de individuele chip, mag een typische chip de afmetingen van 2.5 $\times$ 2.5 cm^2 niet overschrijden. Om toch een groot gevoelig oppervlak te verkrijgen, is een chip-drager ontwikkeld die maximaal 8 chips kan bevatten (2 $\times$ 4 chips, oppervlak 16 cm^2). De chips zijn zodanig uitgelijnd dat zij verbonden

kunnen worden met een enkele sensor met een oppervlakte van 16 cm^2. Momenteel worden in diverse onderzoeken 4-chip combinaties succesvol toegepast.

Geïnspireerd door het grote succes van de Medipix2 detector, is een start gemaakt met de ontwikkeling van een geladen deeltjes detector voor Hoge Energie Fysica experimenten. De ASIC wordt in plaats van met een halfgeleider sensor, met een folie gekoppeld. De folie (Micromegas) heeft een matrix van microscopische gaatjes. De combinatie wordt in een gasvolume geplaatst. Wanneer over de folie en ASIC een potentiaalverschil aangelegd wordt, ontstaat een gasversterkingstrap. Op deze manier is een prototype TPC (Time Projection Chamber) ontwikkeld waarmee aangetoond wordt dat, lawines van elektronen, ontstaan ten gevolge van de ionisatie door kosmisch geladen deeltjes, waargenomen kunnen worden. Primaire elektronen worden met een efficintie beter dan 90% gedetecteerd.

De prestaties van de pixel TPC zijn veel beter dan die van de huidige gasdetectoren. Het uitleeselement (pad) in de conventionele apparatuur (typische afmeting 5 - 10 mm^2) wordt vervangen door een pixel met afmetingen van de orde 100 μm $\times$ 100 μm. Dit impliceert een grotere fijnmazigheid en vervolgens een veel kleinere bezettingsgraad van de individuele pixel. Het ruimtelijk oplossende vermogen verbetert drastisch wat vervolgens bijdraagt aan de verbeterde herkenning van delta-elektronen en scheiding van overlappende sporen. Bovendien draagt de detectie van individuele elektronen bij aan de accurate bepaling van het energieverlies van het geladen deeltje in het gas (dE/dx).

Verdere verbeteringen kunnen verkregen worden door de folie (de Micromegas) te integreren op de ASIC met behulp van additionele bewerkingsstappen op wafer-niveau. Op deze wijze kan een perfecte uitlijning van Micromegas en pixels verkregen worden. Van even groot belang is echter dat het assembleren en onderhoud van de detector verder vereenvoudigd wordt; gasversterking en signaalverwerking zijn gentegreerd in een enkel onderdeel.